

# **Finite-element models related to wideband tympanometry in newborns**

**Hamid Motallebzadeh**

Department of BioMedical Engineering

McGill University, Montréal

June 2015

A thesis submitted to McGill University

in partial fulfillment of the requirements of the degree of

**Doctor of Philosophy**

©Hamid Motallebzadeh

# Finite-element models related to wideband tympanometry in newborns

## Abstract

Early detection of hearing loss accompanied by appropriate early intervention is important in order to avoid problems associated with delayed language development, with its impact on daily communication, educational achievement, psychosocial development and later employment opportunities. Current screening methods are associated with high false-positive rates, which can be attributed to transient conditions in the external ear and middle ear in the first 48 hours *post partum*. Tympanometry (input acoustic admittance measurement in the presence of a range of static pressures) is a promising tool for evaluating the status of the middle ear in newborns.

Tympanometry involves both non-linear responses and viscoelastic (time-dependent) effects, and the tympanic membrane contributes to the overall response more than other middle-ear components do. We have therefore developed a non-linear viscoelastic model based on experimental data reported in the literature for excised strips of tympanic membrane. The constitutive equation of this model is a convolution integral, composed of the Ogden hyperelastic model and the exponential time-dependent function of the Prony series. The model was validated by reproducing the measured hysteresis effect with a single set of parameters.

The newborn ear is anatomically very different from the adult one, resulting in a different input admittance than in adults. We have developed a finite-element model to investigate the admittance responses of the ear canal and middle ear in newborns for frequencies up to 2 kHz. The model was validated by comparison with two sets of clinical data and provides quantitative insight into the separate contributions of the outer and middle ear. The results suggest that admittance measurements could provide more information about the condition of the middle-ear if made at multiple frequencies

around its resonance (around 1.8 kHz).

Wideband stimuli are used to extend admittance measurements to higher frequencies. Taking into account the fluid-structure interaction (FSI) between the air inside the canal and middle-ear cavity and the structure of the ear, we have extended the frequency range of our newborn model up to 10 kHz. The first and second standing-wave modes in the canal were observed at 7.2 and 9.6 kHz, respectively, and the resonance of the middle-ear cavity was identified at 6.1 kHz. The model was validated by comparison with two sets of clinical data and provides interpretations for features that exist in the clinical data but whose significance was not clear.

Our numerical models of the non-linear viscoelastic tympanic membrane and of the admittance responses of the newborn ear provide quantitative insight into the mechanics of the ear and establish a groundwork for the clinical application and interpretation of admittance measurements in newborns.

# **Modèles à éléments finis associés aux tympanométries large bande chez les nouveau-nés**

## **Résumé**

Il est important de pouvoir dépister tôt une perte auditive chez les nouveau-nés et d'intervenir de façon appropriée rapidement afin d'éviter les problèmes liés au retard du développement langagier et ses conséquences sur la communication au quotidien, la réussite scolaire, le développement psychosocial et les possibilités d'emploi ultérieures. Les méthodes de dépistage actuelles produisent des taux élevés de résultats faux positifs que l'on peut attribuer au régime transitoire qui prévaut dans l'oreille externe et moyenne durant les 48 heures qui suivent la période postnatale. La tympanométrie (c.-à-d. la mesure de l'admittance acoustique d'entrée en présence des pressions statiques) est un outil prometteur pour évaluer l'état de l'oreille moyenne des nouveau-nés.

La tympanométrie comprend des réponses non linéaires et des effets viscoélastiques (dépendants du temps). La membrane tympanique contribuant davantage à la réponse globale que les autres composantes de l'oreille moyenne, nous avons donc développé un modèle viscoélastique non linéaire basé sur des données expérimentales publiées dans la littérature et produites à partir de bandes excisées de membrane tympanique. L'équation constitutive de ce modèle est une intégrale de convolution composée du modèle hyperélastique d'Ogden et de la fonction exponentielle dépendante du temps de la série de Prony. Nous avons validé le modèle en reproduisant l'effet d'hystérésis mesuré au moyen d'un ensemble unique de paramètres.

Sur le plan anatomique, l'oreille du nouveau-né est très différente de celle de l'adulte. Pour étudier les réponses d'admittance du conduit auditif et de l'oreille moyenne des nouveau-nés à des fréquences allant jusqu'à 2 kHz, nous avons développé un modèle à éléments finis. Celui-ci, que nous avons validé

en comparant deux ensembles de données cliniques, fournit une piste d'évaluation quantitative sur les contributions distinctes de l'oreille externe et de l'oreille moyenne. Les résultats obtenus semblent indiquer que les mesures d'admittance pourraient fournir des renseignements supplémentaires sur l'état de l'oreille moyenne si elles sont faites pour de multiples fréquences au voisinage de la résonance de l'oreille moyenne (1,8 kHz).

Des stimulus large bande sont utilisés pour étendre les mesures d'admittance à des fréquences plus élevées. En tenant compte de l'interaction fluide-structure entre l'air dans le conduit auditif et dans la cavité de l'oreille moyenne, et la structure de l'oreille, nous avons étendu la gamme de fréquences de notre modèle jusqu'à 10 kHz. Des observations du premier et du deuxième mode d'onde stationnaire ont été effectuées dans le conduit auditif à des fréquences de 7,2 et de 9,6 kHz respectivement, et la résonance de la cavité de l'oreille moyenne a été décelée à 6,1 kHz. Notre modèle, qui a été validé par la comparaison de deux ensembles de données cliniques, permet d'interpréter des éléments dans les données cliniques dont la signification auparavant n'était pas claire.

Nos modèles numériques de la membrane tympanique viscoélastique non linéaire et des réponses d'admittance de l'oreille du nouveau-né offrent une piste d'évaluation des mécanismes de l'oreille, tout en ouvrant la voie à l'utilisation et à l'interprétation en milieu clinique de mesures d'admittance chez les nouveau-nés.

# Acknowledgements

I would like to take this opportunity to thank those without whose help and support this study could not have been accomplished. First of all, I would like to thank my supervisor, Dr. W. Robert J. Funnell. He taught me how to perform scientific research. Without his professional insight, broad knowledge and logical approaches and his remarkable patience I would not have been able to perform this study.

I would like thank my co-supervisor, Dr. Sam J. Daniel, who provided valuable clinical insight to this work. I also deeply appreciate his supervision, comments and support. I would also like to thank my advisory committee members, Dr. Robert Kearney, Dr. Luc Mongeau and Dr. Linda Polka, for the time they spent reviewing my work and providing valuable comments.

I would like to thank my friends and colleagues in the Auditory Mechanics Laboratory and McGill Auditory Science Laboratory. I especially thank my dear friend Nima Maftoon for his great personality and all the valuable hours of discussion that we had about mechanics and modelling. I would also like to thank Brian Gariepy, Mathieu Charlebois, Zinan He, Richard Shapiro, Olubunmi Victoria Akinpelu, Yan Tom Lu and Jacob Pitaro for their help and valuable input to my work.

I would like to express my gratitude to Nancy Abate, Pina Sorrini and Daniel Caron. They were always there to help every student in this department and my studies, like those of many others, would not have gone so smoothly without their help and support.

I would like to express my deep gratitude to my family, my lovely wife Mahsa Beirami, and my friends for their love and support.

# Contributions of authors

## **Chapter 3: A non-linear viscoelastic model for the tympanic membrane**

Published in the *Journal of the Acoustical Society of America* 134(6): 4427-4434 (2013)

### **First author: Hamid Motallebzadeh**

Conceived the study, developed the finite-element model, designed and performed the simulations, validated the model, analyzed and interpreted the output and wrote the manuscript.

### **Second author: Mathieu Charlebois**

Provided data analysis and suggestions for interpretation, reviewed the manuscript.

### **Third author: W. Robert J. Funnell**

Helped conceive the study, supervised the research and writing.

## **Chapters 4 and 5:**

### **Finite-element modelling of the acoustic input admittance of the newborn ear canal and middle ear**

To be submitted to *Journal of the Association for Research in Otolaryngology*

### **Fluid-structure finite-element modelling of the wideband acoustic input admittance of the newborn ear canal and middle ear**

To be submitted to *Journal of the Association for Research in Otolaryngology*

### **First author: Hamid Motallebzadeh**

Developed the finite-element model, designed and performed the simulations, validated the model,

analyzed and interpreted the output, helped to analyze the clinical data and wrote the manuscript.

**Second author: Jacob Pitaro**

Performed wideband immittance measurements on newborns, analysed the immittance data, reviewed the manuscript.

**Third author: W. Robert J. Funnell**

Helped conceive the study, reconstructed the geometry of the model, supervised the research and writing.

**Fourth author: Sam J. Daniel**

Helped conceive the study, provided the experimental facilities and supervised the clinical measurements, provided comments and suggestions, reviewed the manuscripts.

# Table of Contents

<b>1 Introduction.....</b>	<b>1</b>
1.1 Motivation.....	1
1.2 Objectives.....	3
1.3 Thesis outline.....	3
<b>Chapter 2: Background and literature review.....</b>	<b>4</b>
2.1 Anatomy of outer and middle ear.....	4
2.1.1 Introduction.....	4
2.1.2 Anatomy of outer ear.....	4
2.1.3 Anatomy of middle ear.....	5
2.1.3.1 Tympanic membrane.....	6
2.1.3.2 Ossicles.....	7
2.1.3.3 Ligaments and muscles.....	7
2.1.3.4 Middle-ear cavity.....	8
2.2 Introduction of tympanometry.....	8
2.2.1 Principles of immittance audiometry.....	8
2.2.2 Clinical applications of tympanometry.....	9
2.2.3 Tympanometry in children.....	10
2.3 Finite-element method.....	11
2.3.1 Introduction of finite element method.....	11
2.3.2 Nonlinear and time-dependent material models.....	15
2.3.2.1 Finite deformation.....	15
2.3.2.2 Nonlinear elasticity.....	16
2.3.2.3 Nonlinear viscoelasticity.....	17
2.3.3 Fluid-structure interaction.....	17
2.3.4 Finite-element models of the ear.....	19
<b>Chapter 3: A non-linear viscoelastic model for the tympanic membrane.....</b>	<b>22</b>
Preface.....	22
Abstract.....	23
3.1 Introduction.....	23
3.2 Methods.....	25
3.2.1 Experimental data.....	25
3.2.2 Finite-element model.....	26
3.2.3 Constitutive equation.....	28
3.2.4 Determination of model parameters.....	30
3.2.4.1 Time-dependent part.....	30
3.2.4.2 Elastic part.....	31
3.3 Results.....	33
3.3.1 Parameter identification.....	33
3.3.2 Simulated uniaxial tests.....	34
3.3.3 Loading and unloading curves.....	35
3.2.4 Strain-rate effect.....	37
3.4 Discussion.....	38
3.4.1 Non-linear viscoelastic model in the frequency domain.....	38
3.4.2 Loading and unloading loops.....	41

3.4.3 Conclusions.....	41
3.5 Acknowledgements.....	42
<b>Chapter 4: Finite-element modelling of the acoustic input admittance of the newborn ear canal and middle ear.....</b>	<b>43</b>
Preface.....	43
Abstract.....	44
4.1 Introduction.....	44
4.2 Materials and methods.....	48
4.2.1 3-D geometry and finite-element mesh.....	48
4.2.2 Material properties.....	50
4.2.2.1 Introduction.....	50
4.2.2.1 Stiffness.....	51
4.2.2.1.1 Pars tensa.....	51
4.2.2.1.2 Pars flaccida.....	52
4.2.2.1.3 Ear canal.....	52
4.2.2.1.4 Ossicles.....	53
4.2.2.1.5 Ligaments.....	53
4.2.2.2 Poisson's ratio.....	54
4.2.2.3 Density.....	54
4.2.2.4 Damping.....	55
4.2.3 Cochlear load.....	56
4.2.4 Air in middle-ear cavity.....	57
4.2.5 Air in ear canal.....	58
4.2.6 Boundary conditions.....	59
4.2.6 Loading conditions.....	59
4.2.8 Computational methods.....	60
4.2.8.1 Finite-element solver.....	60
4.2.8.2 Admittance calculation.....	60
4.2.9 Sensitivity analysis.....	61
4.2.10 Clinical data.....	64
4.3 Results.....	65
4.3.1 Displacement patterns.....	65
4.3.2 Admittances of the individual models.....	67
4.3.3 Admittance of the combined model.....	70
4.3.4 Model validation and parameter adjustments.....	71
4.3.6 Sensitivity analysis.....	73
4.4 Discussion.....	76
4.4.1 Displacement patterns.....	76
4.4.2 Admittance.....	76
4.4.3 Sensitivity analysis.....	78
4.5 Acknowledgements.....	79
<b>Chapter 5: Fluid-structure finite-element modelling of the wideband acoustic input admittance of the newborn ear canal and middle ear.....</b>	<b>80</b>
Preface.....	80
Abstract.....	81
5.1 Introduction.....	81
5.2 Methods.....	84

2.1 3-D geometry.....	84
5.2.2 Material properties.....	85
5.2.3 Boundary and loading conditions.....	85
5.2.4 Finite-element mesh.....	86
5.2.5 Computational methods.....	86
5.2.5.1 Finite-element solver.....	86
5.2.5.2 Implementation of fluid-structure interaction.....	87
5.2.5.3 Admittance calculation.....	87
5.2.6 Sensitivity analyses.....	87
5.2.7 Clinical data.....	88
5.3 Results.....	89
5.3.1 Sound-pressure and admittance responses.....	89
5.3.2 Sensitivity analysis.....	93
5.3.2.1 Combinations of low-, baseline-, and high-impedance models.....	93
5.3.2.2 Effects of material parameters.....	94
5.3.2.3 Effect of measurement location.....	96
5.3.2.4 Effect of geometry variations.....	98
5.3.3 Comparison with clinical data.....	98
5.3.4 Comparison with non-FSI model.....	101
5.4 Discussion.....	103
5.4.1 Pressure distribution inside the canal and middle-ear cavity.....	103
5.4.2 Model validation.....	105
5.5 Acknowledgements.....	106
<b>Chapter 6: Conclusions and future work.....</b>	<b>107</b>
6.1 Summary.....	107
6.2 Original contributions.....	107
6.3 Clinical application of this work.....	109
6.4 Future Work.....	110
6.4.1 Experimental Work.....	110
6.4.2 Finite-Element Modelling.....	111
<b>References.....</b>	<b>113</b>

# 1 Introduction

## 1.1 Motivation

Hearing loss can be *conductive*, involving the outer and/or middle ear or *sensorineural*, involving the inner ear, auditory nerve and brain, or a combination of these two types. Hearing loss is one of the most common birth defects—about 3 in 1000 babies are born with some degree of hearing impairment (e.g., Lang-Roth, 2014; Akinpelu et al., 2014). Most permanent newborn hearing loss is sensorineural, but its detection and diagnosis are often affected by transient conductive losses (e.g., Akinpelu et al., 2014).

Early detection of hearing loss accompanied by appropriate early intervention is important in order to avoid problems associated with language development that affect daily communication, educational achievement, psychosocial development and later employment opportunities (e.g., Joint Committee on Infant Hearing 1994 Position Statement; American Academy of Pediatrics, 2007). Hearing screening aims to identify infants with hearing loss. Currently, otoacoustic emission (OAE) and/or auditory brainstem response (ABR) tests are employed as screening tools in newborn hearing screening programs. However, high false-positive rates of 2.5% to 8% (e.g., Clemens and Davis, 2001) constitute a major concern and are often attributed to the transient condition of the middle ear due to fluid and other residual material in the first 48 hours postpartum (e.g., Akinpelu et al., 2014), which conflicts with the desire for shorter hospital stays. It would thus be very valuable to be able to identify conductive losses quickly, right at the time of the initial screening just after birth.

In addition to the identification of hearing impairments by hearing screening, diagnosis of the source of the hearing loss, including differentiation between conductive and sensorineural hearing loss is the next step because the course of intervention is quite different. Hearing assessment techniques (especially the cross-checking of results from multiple approaches) can help us to identify hearing loss type and severity. However, since we cannot perform behavioural evaluations (such as speech and pure-

tone audiometry) on infants, we have to rely on non-behavioural responses and physiological measures (Stach, 2008, p. 221).

Admittance measurement is a promising tool for assessing middle-ear status in newborns. In this method, the acoustic input admittance of the outer and middle ear is measured in response to an acoustic excitation, which can be either single-frequency or wideband. Tympanometry provides additional information by introducing a range of quasi-static air pressures in the ear canal along with the acoustic excitation. However, the admittance response of the infant ear is not at all well understood. Differences in the interpretation of results in adults and newborns may be attributed to anatomical and physiological differences occurring during maturation (e.g., Saunders et al., 1983; Eby and Nadol, 1986; Keefe et al., 1993; Qi et al., 2006).

Understanding the mechanics and the anatomical maturation of the middle ear after birth is obviously essential to understanding conductive hearing loss and to designing better screening and diagnostic tests. In recent years, a great deal of experimental work has been done around the world to characterize and clarify middle-ear function (e.g., Keefe et al., 1993; Keefe and Levi, 1996; Merchant et al., 2010). Since there are many factors affecting experimental results, outputs are difficult to interpret (e.g., Sanford and Feeney, 2008). With developments in software and medical imaging, three-dimensional middle-ear finite-element models have become a valuable tool for studying the mechanical behaviour of the ear, particularly the middle ear. Those models can help to interpret clinical data and to predict the effects of abnormal conditions. Qi et al. (2006, 2008) developed static models of the newborn ear canal and middle-ear, without taking into account the dynamic behaviour of the ear components. A preliminary study of the dynamic responses of the newborn ear canal and middle-ear, limited to frequencies up to 2 kHz, was performed by Gariépy (2011).

## 1.2 Objectives

The overall objective of this study was to develop a better quantitative understanding of the mechanical behaviour of the newborn outer and middle ear, particularly their admittance response. More specifically, the objectives of this thesis are listed below:

1. Development of a non-linear viscoelastic model for the tympanic membrane (TM) and investigation of TM behaviour relevant to the conditions involved in tympanometry: large, sweeping ear-canal pressures applied over a period of a few seconds.
2. Development of numerical models of the newborn ear canal and middle ear, to investigate features in clinical wideband immittance measurements and to provide insight into tympanometry.

## 1.3 Thesis outline

This thesis is based on three manuscripts, presented in Chapters 3, 4 and 5. In addition to the background information and literature reviews provided in the introductory sections of these manuscripts, a general background is provided in Chapter 2 for ear anatomy and for numerical aspects of the modelling. Chapter 3 presents a numerical approach for a non-linear viscoelastic model for the tympanic membrane (Motallebzadeh et al., 2013), representing its non-linear and time-dependent behaviour, relevant to the conditions involved in pressurized admittance measurements. Chapter 4 presents finite-element models of the newborn ear canal and middle ear to study their acoustic input admittance response for frequencies of up to 2 kHz. In Chapter 5, taking into account fluid-structure interactions, the frequency range is extended to 10 kHz to identify higher-frequency features in the clinical admittance data.

## **Chapter 2: Background and literature review**

### **2.1 Anatomy of outer and middle ear**

#### **2.1.1 Introduction**

The auditory system collects the acoustic information, modulates, transforms, amplifies and channels them to the brain via neural path. In general, this system is divided into three main sections: outer, middle and inner ear (Fig. 2–1). The outer ear which consists of auricle (or pinna) and the external acoustic meatus (or ear canal) collects the peripheral acoustical waves and transfers them to the middle ear. The middle ear contains the tympanic membrane (or eardrum), ossicles (i.e., malleus, incus and stapes) suspensory attachments of ligaments, tendons and muscles and middle-ear cavity. The acoustical waves vibrate the TM and the motion is passed through the ossicular chain into the inner ear. Inner ear itself consists of two parts: the cochlea which transforms acoustical energy to neural signals and the vestibular system which serves as a sensor of motion position. More detailed description of the ear anatomy can be found in standard anatomy textbooks (e.g., Standring, 2008, chap. 36 & 37). In this section we focus of anatomical characteristics of the outer and middle ear in human and anatomical maturation during the growth.

#### **2.1.2 Anatomy of outer ear**

The outer ear is the lateral portion of the ear. It is composed of the auricle (or pinna) and the external acoustic meatus (or outer ear canal ). The pinna has a quite complex anatomy and its growth is parallel to that of the other components of the head and continues approximately by 9 years of age (e.g., Saunders et al., 1983, p. 4).

The ear canal is a tube that begins in the bottom of the concha and extends into the temporal bone and terminates at the tympanic membrane (TM). In adults, its length is approximately 25 mm on the posterior-superior wall and due to the obliquity of the TM, the length on the antero-inferior wall is

6 mm longer. (Anson and Donaldson, 1992, p. 146). The ear canal forms an S-shape curvature and one third lateral portion is surrounded by soft tissue and the remaining medial two third of it is surrounded by bone (Standring, 2008, p. 620).

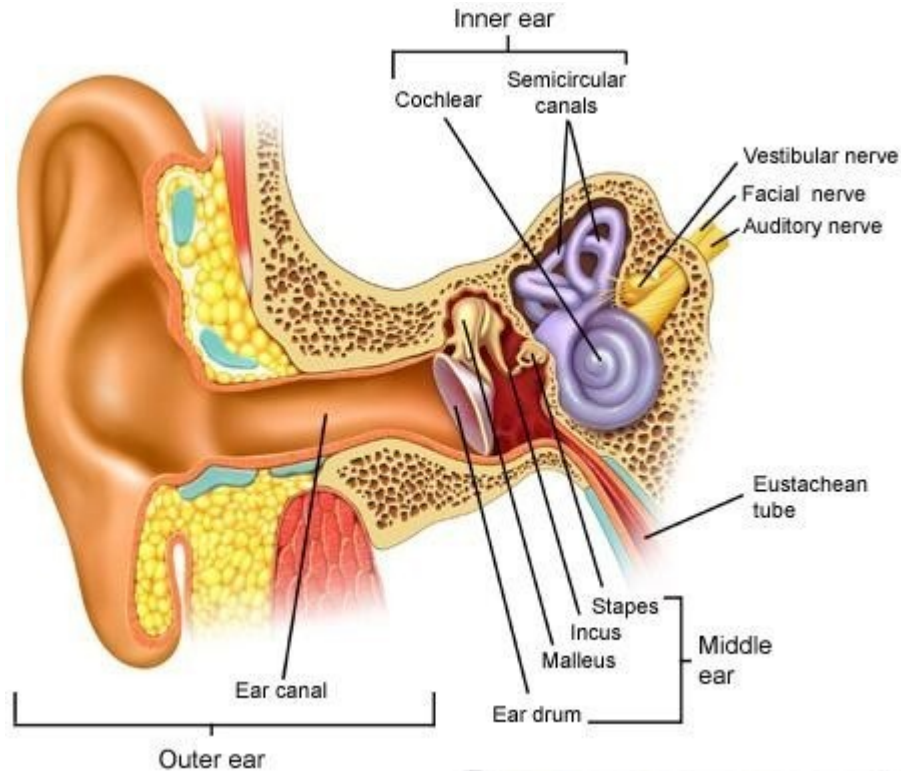


Fig. 2-1. Overview the human ear anatomy (Source: <http://www.ent-specialist.org/> as of 4 April 2015)

The postnatal development of the ear canal continues by age of 7 years (e.g., Saunders et al., 1983, p. 4). The cross-sectional at the birth is approximately oval and much narrower than that of adult. The canal curvature is more straight than that in adults and the surrounding bony wall is developed during the first 3 years of age (e.g., Eby and Nadol, 1986).

### 2.1.3 Anatomy of middle ear

The middle ear is located in the petrous part of the temporal bone, terminated laterally at the tympanic membrane and medially at the stapes footplate. The ossicular chain and its suspensory attachments are located within middle-ear cavity. This cavity is channelled to the throat by the Eustachian tube which is normally closed and equalizes the pressure on both sides of the tympanic membrane, when is opened.

### 2.1.3.1 Tympanic membrane

The tympanic membrane (TM), is a conical shape shell with an apex pointing inward the middle-ear cavity. Its longest and shortest diameters measure between 9 to 10 mm and 8 to 9 mm, respectively (e.g., Lim, 1970; Anson and Donaldson, 1992, p. 147). The TM reaches the adult size before birth. It is anchored to the tympanic sulcus thickened fibrocartilaginous ring or annulus.

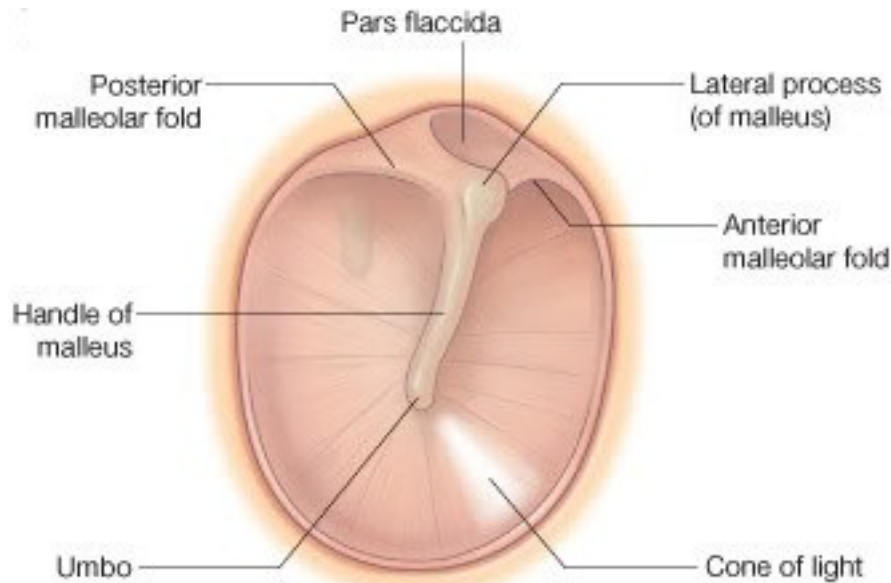


Fig. 2–2. Anatomy of the tympanic membrane

(Source: <http://www.case.edu/med/otolaryngology/ben.htm> as of 4 June 2015)

The TM consists of two parts, namely the pars tensa and pars flaccida (Fig. 2–2). The pars tensa, the larger portion of the TM, is composed of three layers: the lateral epidermal layer, the intermediate fibrous layer and the medial mucosal layer. Lim (1970) reported the thickness of the pars tensa being between 30 and 90  $\mu\text{m}$  in adults. More recently, Kuypers et al. (2006) reported a thickness range from 40 to 120  $\mu\text{m}$  for the pars tensa. The pars flaccida is approximately one-tenth of the TM and is considered to be the extension of the skin of the external ear canal and its thickness varies between 30 and 230  $\mu\text{m}$  in adults (Lim, 1970).

Ruah et al. (1991) reported morphological changes of the TM during post-natal development and investigated the similarity between age-related ultra-structural changes of the TM and changes

observed in human skin. They also reported that the thickness of the pars tensa and pars flaccida is significantly higher than that of adults. The tympanic ring is yet incomplete at birth (e.g., Standing, 2008, p. 624). More details about the morphology and thickness of the newborn TM are presented in Section 4.2.1.

### *2.1.3.2 Ossicles*

Middle ear contains three bones, called malleus, incus and stapes. The malleus, the most lateral bone, is the largest of the ossicles. It is composed of head, neck, manubrium and anterior and lateral processes and measures between 7.6–9.1 mm in length (e.g., Wever and Lawrence, 1954, p. 417). The malleus is attached to the TM along the length of the manubrium.

The middle bone in the ossicular chain is the incus, shaped like an anvil. The anterior portion of the incus articulates with the malleus in a saddle-shaped joint, called the incudomalleolar joint. The lengths of the short and long processes of the incus are approximately 5 and 7 mm, respectively (e.g., Wever and Lawrence, 1954, p. 417).

The most medial bone in the ossicular chain is the stapes. It has a head, neck, two crura and a footplate. It articulates with the incus via the incudostapedial joint. The footplate is attached to the oval window via the stapedial annular ligament. The surface area of the stapes footplate of 2.3 – 3.75 mm<sup>2</sup> has been reported in the literature (e.g., Wever and Lawrence, 1954; Gan et al., 2011).

The ossicles are not mature at birth. Although they ossify prenatally (e.g., Standing, 2008, p. 627), and their size and weight are still developing after birth (e.g., Saunders et al., 1983, p. 10).

### *2.1.3.3 Ligaments and muscles*

There is controversy about what ligaments there are in the human ear. Here we focus on those that are mostly reported in the literature. The malleus attaches to the TM by a ligament, along manubrium length. Three ligaments are attached to the malleus, called superior, lateral and anterior ligaments. The

incus is connected to the fossa incudis by the posterior ligament. An annular ligaments attaches the footplate of the stapes to the oval window. As a collagenous tissue, ligaments undergo significant alterations from newborn to adult (e.g., Williamson et al., 2001).

There are two muscles in the middle-ear cavity, tensor tympani and stapedius muscles. The tensor tympani attaches the handle of the malleus to the anterior wall of the tympanic cavity and the stapedius muscle connects the stapes head to the mastoid wall of the tympanic cavity. The tensor tympani and stapedius muscles are approximately 25 and 6.3 mm in length, respectively. The muscles and their connections are matured prenatally, however, the attachments are not matured until one week after birth (e.g., Saunders et al., 1983, p. 10).

#### *2.1.3.4 Middle-ear cavity*

The middle-ear cavity refers to the set of air-filled and inter-connected cavities within the temporal bone that comprise the tympanic cavity, aditus, antrum, and mastoid inside the temporal bone. The air volume in the cavity ranges from 2000 to 22000 mm<sup>3</sup> in adults (e.g., Molvaer et al., 1978). The size of the cavity undergo significant changes after birth, due to the enlargement of the antral and mastoid air sinuses (e.g., Saunders et al., 1983, p. 11).

## **2.2 Introduction of tympanometry**

### **2.2.1 Principles of immittance audiometry**

Immittance measurement is an audiological tool for assessing middle-ear status. It was introduced into clinical practice during the 1970s (e.g., Stach, 2008, p. 314). In this method the acoustical input immittance of the outer and middle ear is measured in response to probe tones. The measurement can be done in two conditions: (1) under ambient pressure or (2) with a pressurized ear canal. In the second form (called tympanometry), a probe tone is introduced to the ear canal while a pump generates quasi-

static pressures ranging from zero to  $\pm 200$ - $400$  daPa, going from negative to positive pressures or vice versa.

Immittance refers to either admittance  $Y$  or impedance  $Z$ . The admittance is a measure of the mobility of a system. In acoustics, the admittance of a system is defined by

$$Y = U/P, \quad (2-1)$$

where  $U$  and  $P$  are the volume velocity and the acoustical pressure, respectively, at the point where the measurement is performed. The impedance is the reciprocal of the admittance. The admittance and impedance are complex numbers, so they can be reported in terms of either magnitude and phase or real and imaginary parts.

### **2.2.2 Clinical applications of tympanometry**

Tympanometry is often done with a single probe tone of 226 Hz. However, more information can be obtained by using multiple frequencies (e.g., Alberti and Jerger, 1974; Colletti, 1975; Funasaka et al., 1984; Keefe and Levi, 1996; Shahnaz et al., 2008). In fact multi-frequency tympanometry has been shown to improve the test sensitivity in some cases of outer/middle ear pathologies (e.g., Shahnaz et al., 2008). This kind of measurement can be performed in two methods; multiple discrete frequencies (e.g., Colletti, 1975) and wideband-acoustic stimuli both in presence of sweeping quasi-static pressure (e.g., Funasaka et al., 1984). In the former method, a full course of quasi-static pressure variation in the ear canal is performed (in the range of for example  $\pm 4$  kPa (e.g., Colletti, 1975), while the probe tone is held at a constant frequency and the pressurization is repeated for each single probe tone. In the wideband immittance measurements, the acoustic stimulus – which can be a sweep-frequency tone (e.g., Funasaka et al., 1984), a chirp (e.g., Keefe et al., 1993) or a click (e.g., Keefe and Simmons, 2003) – is presented to the ear canal every 40 ms, for example, while the quasi-static pressure changes by only a few daPa (e.g., 3.2 daPa for a pressure course of  $-3$  to  $+2$  kPa at a rate of 0.75 kPa/s as in Liu

et al., 2008), and it is assumed that the pressure is constant at each frequency.

At low frequencies (e.g., below 2 kHz), the acoustic pressure distribution is approximately uniform in the ear canal and across the TM surfaces. At higher frequencies, however, the geometrical dimensions of the canal and TM are not small in comparison with the sound wavelength, so this assumption is not valid any longer and the output of tympanometry becomes sensitive to the position of the probe tip (e.g., Keefe et al., 1993; Voss and Allen, 1994). To overcome this problem, energy reflectance has been proposed for clinical measurements. It has been stated that, unlike the immittance response, the energy reflectance in adults represents the response of the TM, independent of the location of the probe tip, because (1) the energy loss of the sound wave in the enclosed air in the canal is negligible; (2) the ear canal acts like a smoothly varying transmission line (i.e., no significant energy is reflected from the canal wall); and (3) energy loss at the canal wall is negligible (e.g., Voss and Allen, 1994).

### **2.2.3 Tympanometry in children**

Low-frequency tympanometry at a single probe tone provides easy-to-interpret results for adult ears but the results in newborns are very different from those in adults. Tympanometry with traditional low-frequency probe tones (e.g., 226 Hz) is not recommended for infants less than 7 months of age (Paradise, 1982; e.g., Holte et al., 1990). The differences between infant and adult ears may be attributed to anatomical and physiological differences occurring during maturation (Eby and Nadol, 1986; Qi et al., 2006; Saunders et al., 1983). As shown in Fig. 2–3, some of the most important anatomical differences between infants and adults can be summarized as follows:

1. The sizes of the ear canal and middle-ear cavity have not matured yet.
2. The relative orientation of the ear canal and the TM undergoes postnatal changes.
3. The density and size of the ossicles are still developing after birth.

4. Unlike the case in adults, the newborn ear canal is surrounded mainly by soft tissue.
5. In infants, the TM is less stiff and yet thicker than in adults.

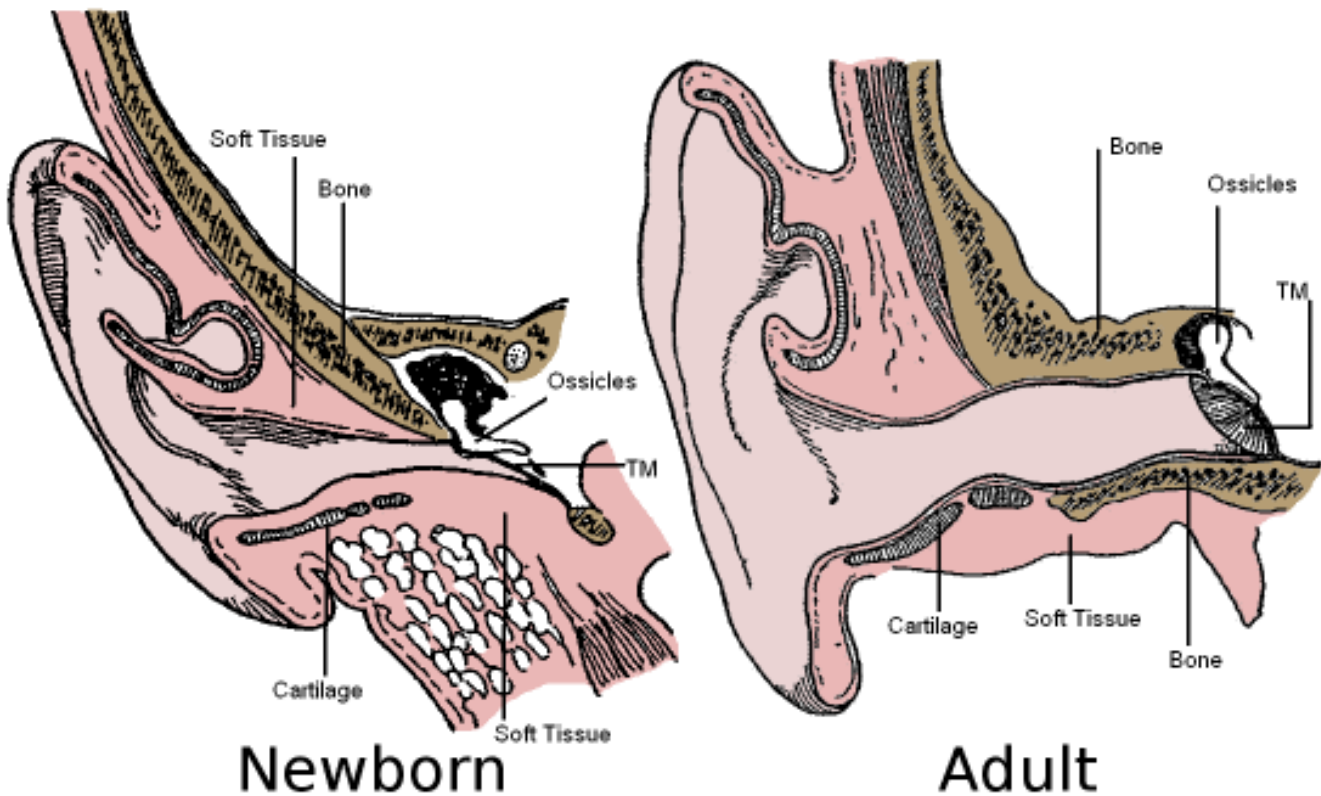


*Fig. 2–3. Comparison of the ear anatomy between newborns and adults (After Fowler EP Jr. (1947):  
Medicine of the ear, 2nd ed., T. Nelson, New York)*

In addition to the unsatisfactory results of tympanometry at low frequencies, the sensitivity of the tympanometry output to the position of the probe tip inside the canal at higher frequencies (as stated in 2.2.2) is yet another issue. Since the compliant ear canal absorbs some portion of the acoustical energy, unlike the case in adults, the energy reflectance in newborns is still sensitive to the position of the probe tip.

## 2.3 Finite-element method

### 2.3.1 Introduction of finite element method

The finite-element method (FEM) is a numerical approach to finding approximate solutions for partial differential equations that govern a physical system. In this method, the physical system under study is

divided into simple components, called elements, whose behaviour can be described by simple equations, readily solved. The combination of the responses of these elements can represent the complex behaviour of the overall system. The development of this method can be traced back to the early 1940s and the work of McHenry, Hrenikoof and Newmark in the field of solid mechanics (e.g., Zienkiewicz et al., 1977).

The finite-element analysis can be sub-categorized into three main steps:

1. Pre-processing: reconstructing the geometry; mesh generation (discretizing the system into finite elements); assigning the material properties; assigning the boundary, initial and loading conditions; and the mathematical formulation.
2. Processing: solving the governing equations.
3. Post-processing: analyzing the outputs, and validating the results.

More details about this method can be found in standard finite-element method textbooks (e.g., Zienkiewicz et al., 1977).

As a brief introduction to this method, let us consider a continuum solid domain. To model a continuum mechanical system, a geometry, more or less accurate, is required. In finite-element models of living tissues, the geometry is usually generated based on sets of images, such as computed tomography (CT). Segmentation of each image is performed and then the combination of them will generate the final geometry. The reconstructed geometry is then broken down to a mesh of small components such as hexahedral and tetrahedral elements. The system characteristics (e.g., material parameters), initial and boundary conditions, external forces and the interaction between system components are defined and the constitutive equations that can represent the system response to the applied conditions are selected. The time course (duration) of the modelling is divided into finite

segments. In the main step of finite-element modelling, the governing equations (e.g., the constitutive equations of the materials) are approximated by linear sets of equations for each element and the combination of them results in matrices of coefficients (related to material properties and geometry) and variables (spatial coordinates and time).

The basic equations for the finite-element method are derived as a variational formulation based on Hamiltonian mechanics. In this formulation, the classical Newtonian equations of mechanics (i.e., vector-based formulations) are reformulated using the principle of stationary action by minimizing the energy functional  $\delta W$ :

$$\delta W = \int_v \boldsymbol{\sigma} : \delta \mathbf{d} dv - \int_v \mathbf{f} \cdot \delta \mathbf{v} dv - \int_{\partial v} \mathbf{t} \cdot \delta \mathbf{v} da = 0 . \quad (2-2)$$

The first integral term is the potential energy of the system as a product of the stress tensor  $\boldsymbol{\sigma}$  and the virtual rate of deformation tensor  $\delta \mathbf{d}$  in the volume element of  $dv$ . The second term represents the virtual work done by the volume forces  $\mathbf{f}$  acting on the resultant velocity  $\delta \mathbf{v}$  of the volume element of  $dv$ . The third term is the virtual work of the surface forces  $\mathbf{t}$  and the resultant velocity, on a surface element  $da$ , the surface of the element  $\partial v$ . By taking advantage of the small dimensions of the elements and the small time steps, this formulation is linearized for each element. Solving the resulting system of linear equations provides the response of the system.

In the application of the finite-element method, a number of factors should be considered to provide an accurate representation of reality:

1. Mesh convergence: A coarse mesh generates a small system of equations, but the results may not be accurate enough. A very fine mesh, on the other hand, results in a high computational cost. A systematic mesh analysis should be performed to obtain an appropriate mesh.
2. Constitutive equations: Material behaviour is always non-linear. The nature of the deformations

of the model components during the simulations, determines whether their behaviour should be approximated by linear constitutive equations or more complicated equations should be adopted. There are different methods to linearize the mathematical equations that govern the system behaviour. In the finite-element method the choice of the method is based on trade-offs between the computational cost and the required accuracy. For example, approximating a curve with a second-order polynomial equation results in a more accurate representation than a linear one, but it increases the computational time.

3. Boundary, initial and loading conditions: In general, the interactions of the system within itself (i.e., between the components of the system) and with the environment (boundaries of the system and applied loads) are very complicated. A successful finite-element model should represent those conditions in a simplified form but still accurately enough.
4. Mechanical representation: Based on the nature of the system that is under study, appropriate simplifications may not only reduce the computational cost but also result in more accurate results. For example, modelling a quasi-linear and quasi-static condition with a non-linear dynamic representation not only increases the computation time, but may introduce numerical errors in the output.
5. Model verification and validation: Model verification refers to the verification of the computer code and the mathematical calculations. Model validation is the process of investigating how accurately the model represents the experimental measurements.

There are a number of software packages for finite-element modelling. Most of the commercial ones (e.g., ANSYS <http://www.ansys.com/> and ABAQUS <http://www.3ds.com/products-services/simulia/products/abaqus/>) integrate the three steps of modelling, namely pre-processing, processing and post-processing. In addition, free (libre) and open-source software is available. Most such software aims to

provide specific services. For example, there is software that is developed for the purpose of geometry and mesh generation (e.g., Fie, Tr3 and Fad at <http://www.audilab.bme.mcgill.ca/sw/>, PreView at <http://www.febio.org/preview/>, Gmsh at <http://www.geuz.org/gmsh/>), non-linear material representation (e.g., Mfront at <http://tfel.sourceforge.net/documentations.html>), solving the mathematical equations (e.g., FEBio at <http://www.febio.org/febio/> and Code\_Aster at <http://www.code-aster.org/>) and visualization of the output (e.g., PostView at <http://www.febio.org/postview/> and ParaView at <http://www.paraview.org/>).

### 2.3.2 Nonlinear and time-dependent material models

In continuum mechanics, nonlinearity arises from three conditions: (1) large deformations (e.g., large strains), (2) nonlinear material properties (e.g., nonlinear elasticity), and (3) change of the status (e.g., contact) (Holzapfel, 2000, chap. 6). In this brief introduction, we look at large deformations and nonlinear elastic and viscoelastic behaviours.

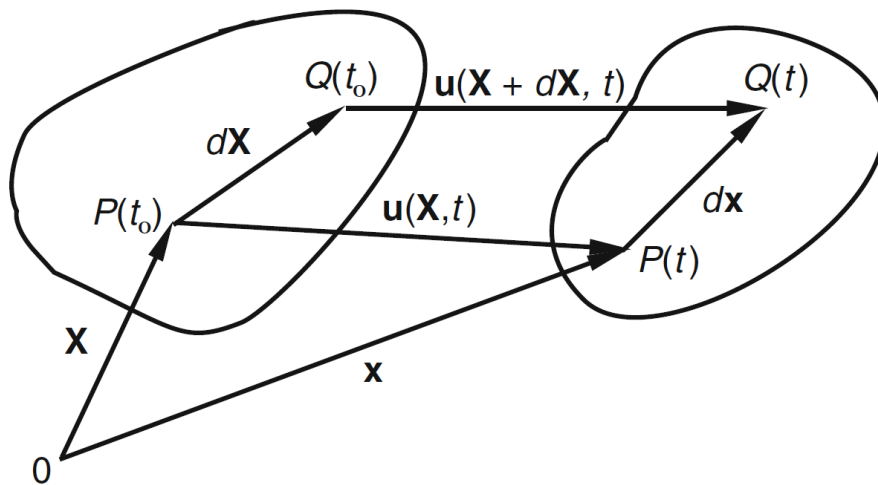


Fig. 2–4. Configuration and deformation of a continuum body (from Lai et al., 2009, p. 84)

#### 2.3.2.1 Finite deformation

Let us consider a configuration of a solid continuum domain in its reference (initial) and deformed configurations. A typical material point of  $P(t_0)$  and its neighbouring point  $Q(t_0)$  in the reference

configuration  $\Omega_0$  are transformed to new positions  $P(t)$  and  $Q(t)$  in the deformed configuration  $\Omega_t$  by the spatial vectors  $\mathbf{u}(\mathbf{X},t)$  and  $\mathbf{u}(\mathbf{X}+d\mathbf{X},t)$ , respectively. According to the configuration in Fig. 2–4, one can write the following vector-based relationships:

$$\begin{aligned}\mathbf{x}+d\mathbf{x}&=\mathbf{X}+d\mathbf{X}+\mathbf{u}(\mathbf{X}+d\mathbf{X},t) \\ d\mathbf{x}&=d\mathbf{X}+\mathbf{u}(\mathbf{X}+d\mathbf{X},t)-\mathbf{u}(\mathbf{X},t), \\ d\mathbf{x}&=d\mathbf{X}+(\nabla\mathbf{u})d\mathbf{X} \\ d\mathbf{x}&=\mathbf{F}d\mathbf{X}\end{aligned}\tag{2-3}$$

where  $\nabla\mathbf{u}$  is a second-order tensor known as the *displacement gradient* and  $\mathbf{F}$  is the deformation gradient. Two forms of strain tensor are defined based on the *right Cauchy-Green deformation tensor*  $\mathbf{C}$  ( $=\mathbf{F}^T\mathbf{F}$ ,  $\mathbf{F}^T$  being the transverse of matrix  $\mathbf{F}$ ): (1) the *Lagrangian finite strain tensor*  $\mathbf{E}$  and (2) the *Green-Lagrangian strain tensor*  $\mathbf{e}$ . The strain tensors are defined by

$$\mathbf{E}=\frac{1}{2}(\mathbf{C}-\mathbf{I})\quad\mathbf{e}=\frac{1}{2}(\mathbf{I}-\mathbf{C}),\tag{2-4}$$

where  $\mathbf{I}$  is the unity matrix. Let us expand the Lagrangian finite strain tensor  $\mathbf{E}$ , for instance:

$$\mathbf{E}=\frac{1}{2}[\nabla\mathbf{u}+(\nabla\mathbf{u})^T+\nabla\mathbf{u}(\nabla\mathbf{u})^T].\tag{2-5}$$

For infinitesimal deformations, the term  $\nabla\mathbf{u}(\nabla\mathbf{u})^T$  is neglected, but for large deformations this term is kept.

### 2.3.2.2 Nonlinear elasticity

Unlike the case for linear elastic materials, the strain-stress relationship is not linear for nonlinear elastic materials, commonly called hyperelastic materials. There are a number of constitutive equations, derived from a strain-energy function, such as the Mooney–Rivlin, Neo-Hookean, Yeoh, and Ogden models (e.g., Holzapfel, 2000). More details about the formulation and application of the Ogden

hyperelastic model are presented in Section 3.2.3.

### 2.3.2.3 Nonlinear viscoelasticity

Most materials, and particularly living tissues, display both non-linear and time-dependent (viscoelastic) behaviour. Different formulations have been introduced to derive their constitutive equations (e.g., Charlebois et al., 2013). More details about the formulation and application of non-linear viscoelastic models are presented in Section 3.2.3.

## 2.3.3 Fluid-structure interaction

Fluid-structure interaction (FSI) is a field in physics that deals with mechanical interactions between fluid and structural domains. Sound waves are small distortions in a medium, propagating in space and time. When two media, one solid and one fluid, share an interface, the acoustic-structural interaction is modelled by coupling the constitutive equations of both structural and fluid domains at their interface. Let us consider a simple example of a homogeneous linear elastic structure domain  $\Omega_s$  and an inviscid fluid domain  $\Omega_f$  sharing an interface  $\Sigma$  (Fig. 2–5).

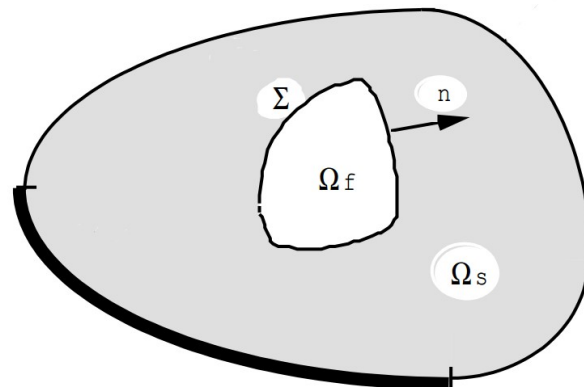


Fig. 2–5. A model of acoustic-structural interaction model (Modified from [http://www.code-aster.org/V2/doc/default/en/man\\_r/r4/r4.02.02.pdf](http://www.code-aster.org/V2/doc/default/en/man_r/r4/r4.02.02.pdf))

For the elastic structure, the conservation of the momentum is formulated by

$$\sigma_{ij,j} - \rho_s \frac{d^2 u_{si}}{dt^2} = 0, \quad (2-6)$$

where  $\sigma_{ij,j}$  is the derivative of the stress  $\sigma_{ij}$  in the  $j$  direction,  $\rho_s$  is the density and  $u_{si}$  is the displacement of the structure in the  $i$  direction. The linear elastic constitutive equation is

$$\sigma_{ij} = C_{ijkl} \varepsilon_{kl}, \quad (2-7)$$

where  $C_{ijkl}$  are the corresponding components of the stiffness matrix and  $\varepsilon_{kl}$  are the strain components, which themselves are defined in terms of the deformation matrix  $u$  by

$$\varepsilon_{kl} = \frac{1}{2} (u_{k,l} + u_{l,k}), \quad (2-8)$$

where  $u_{k,l}$  and  $u_{l,k}$  are derivatives of the deformations  $u$  in the  $k$  and  $l$  directions with respect to the  $l$  and  $k$  directions, respectively.

For the inviscid fluid domain, the conservation of momentum equation is formulated by

$$\tau_{ij,j} - \rho_f \frac{d^2 u_{fi}}{dt^2} = 0, \quad (2-9)$$

where  $\tau_{ij,j}$  is the derivative of the stress  $\tau_{ij}$  in the  $j$  direction,  $\rho_f$  is the density and  $u_{fi}$  is the displacement in the  $i$  direction. The inviscid assumption for the fluid indicates that it resists only pressure, so the stress components is

$$\tau_{ij,j} = -p \delta_{ij}, \quad (2-10)$$

where  $p$  is the pressure and  $\delta_{ij}$  is the Kronecker delta ( $= 0$  if  $i \neq j$ ,  $= 1$  if  $i = j$ ). In a fluid medium, pressure is a function of the fluid density  $\rho$  and the speed of the sound  $c$  in that fluid:

$$p = \rho c^2 . \quad (2-11)$$

The Helmholtz's equation for the propagation of the waves in a fluid medium is

$$\Delta p + k^2 p = 0 , \quad (2-12)$$

where  $\Delta$  is the second-order differential operator and  $k = \omega/c$  is the wave number ( $\omega = 2\pi f$  is the angular frequency).

At the interface  $\Sigma$  of the structure and fluid domains, there are two conditions that should be satisfied: (1) the continuity of the normal stresses and (2) the continuity of the normal velocities. The first condition is represented by

$$\sigma_{ij} \cdot n_i = \tau_{ij} \cdot n_i = -p \delta_{ij} \cdot n_i , \quad (2-13)$$

where  $n_i$  is the normal unity vector in the  $i$  direction and  $\cdot$  represents the scalar product. The continuity of the normal velocities is represented by

$$\frac{d u_{s_i}}{d t} \cdot n_i = \frac{d u_{f_i}}{d t} \cdot n_i . \quad (2-14)$$

Satisfying the continuity equations, the fluid and structure domains interact with each other and the forces and deformations transfer from one to the other.

### 2.3.4 Finite-element models of the ear

The first finite-element model of the middle ear was presented by Funnell and Laszlo (1978). They studied the low-frequency response of the cat TM. This model was extended to higher frequencies by Funnell (1983), an investigation of the undamped natural frequencies of the TM. The effect of damping was added to the TM model by Funnell et al. (1987). Lesser and Williams (1988) applied the finite-element method to a two-dimensional cross-sectional geometry of the human TM and malleus and investigated a variety of effects, such as the shape of displacement of the TM. Williams and Lesser

(1990) reported natural frequencies of an uncoupled 3-D TM. Wada et al. (1992) presented a three-dimensional finite-element model of the human middle ear. The mechanical characteristics of the model were adjusted to reproduce the experimental data, for example, the effect of the annular ligament of the TM was represented by linear and torsional springs. Ladak and Funnell (1996) looked at the effects of abnormalities in the ossicular chain of a cat middle-ear. Funnell and Decraemer (1996) used phase-shift moiré topography to study the shape and deformation of the TM, combined with finite-element modelling. Daniel et al. (2001) used imaging techniques to reconstruct more realistic geometries for finite-element models of the middle ear. Attempts have been made to improve the geometrical characteristics of the models. Series of histological images (Sun et al., 2002), micro-computed tomography (Decraemer et al., 2003) and magnetic resonance images (Kelly et al., 2003), and combinations of these methods (Elkhouri et al., 2006), have been utilized to reconstruct more accurate geometries of the models.

In finite-element models of the middle ear, a variety of constitutive models have been applied to different components based on their mechanical behaviours. The simplest constitutive model is linear isotropic elasticity. Funnell and Laszlo (1978) modelled the TM by a single layer of isotropic material. Multilayer and orthotropic elastic models have also been applied to the TM (e.g., Gan et al., 2006; Tuck-Lee et al., 2008). Viscous and nonlinear behaviour of the TM has also been taken into account in some finite-element models of the middle ear or its components (e.g., Ladak et al., 2006; Qi et al., 2008; Motallebzadeh et al., 2013a). There are a number of studies that explored the acoustical and structural coupling in the models, representing the acoustical pressure distribution in the canal or the effect of the air trapped in the middle-ear cavity (e.g., Day and Funnell, 1990; Gan et al., 2004; Ihrle et al., 2013; Vollandri et al., 2014).

The first attempts to model the newborn ear were performed in our group. Qi et al. (2006) presented

a non-linear finite-element model of the newborn canal and explored large deformations of the soft tissue surrounding the canal in response to high pressures up to  $\pm 3$  kPa. In another study Qi et al. (2008) presented a non-linear model of the response of the newborn middle ear to high pressures. They proposed a range of plausible Young's moduli for the TM and canal wall, based on the data reported for adults and taking into account the effects of maturation. In their non-linear models, the hyperelastic model was based on the linear elastic parameters. In both studies the ear components were subjected to static loading conditions. Gariepy (2011) presented a preliminary linear dynamic model of the response of the newborn ear to sound pressures for frequencies below 2 kHz and computed the input immittance. He adjusted the elastic parameters from Qi et al. (2006, 2008) for the dynamic behaviour of the tissues. In the models of both Qi et al. and Gariepy, the tympanic membrane was modelled with shell elements. (The geometries of the models in both studies were later found to have been scaled based on an incorrect interpretation of the slice thicknesses of the CT images, and Gariepy (2011) evaluated the magnitude of the effects of the error.)

Cheng et al. (2007) reported a series of mechanical measurements on strips of the human TM and reported non-linear elastic behaviour with deformations up to 20%. They also reported the time-dependent characteristics of the TM. These data are used in Chapter 3 to propose a more realistic constitutive model of the TM for large deformations at low frequencies. In Chapters 4 and 5 the ranges of newborn ear properties used by Qi et al. and by Gariepy are reconsidered based on experimental data reported recently in the literature, and a more accurate thickness map of the newborn TM is presented, based on a set of histological images. In Chapter 5, by taking into account fluid-structure interactions, the modelling of the immittance response of the ear is extended to higher frequencies.

## **Chapter 3: A non-linear viscoelastic model for the tympanic membrane**

Published in the *Journal of the Acoustical Society of America*, December 134(6): 4427-4434 (2013)

### **Preface**

In this paper, a non-linear viscoelastic model is presented for the human tympanic membrane (TM), based on experimental data reported in the literature for strip samples of the TM. Our approach allows us to model both the loading and unloading curves, and the associated hysteresis, with a single set of parameters. We also estimate the energy dissipation as a function of frequency, and explore the effects of strain rate on the relaxation behaviour. This model is suitable for representation of the TM behaviour at large deformations and low frequencies, the conditions corresponding to the pressurization involved in tympanometry.

## **Abstract**

The mechanical behaviour of the tympanic membrane displays both non-linearity and viscoelasticity. Previous finite-element models of the tympanic membrane, however, have been either non-linear or viscoelastic but not both. In this study, these two features are combined in a non-linear viscoelastic model. The constitutive equation of this model is a convolution integral composed of a non-linear elastic part, represented by an Ogden hyperelastic model, and an exponential time-dependent part, represented by a Prony series. The model output is compared with the relaxation curves and hysteresis loops observed in previous measurements performed on strips of tympanic membrane. In addition, a frequency-domain analysis is performed based on the obtained material parameters, and the effect of strain rate is explored. The model presented here is suitable for modelling large deformations of the tympanic membrane for frequencies less than approximately 3 rad/s or about 0.6 Hz. These conditions correspond to the pressurization involved in tympanometry.

## **3.1 Introduction**

The eardrum or tympanic membrane (TM), the gateway to the middle ear, has a curved conical shape with the apex pointing medially. It receives airborne sound waves collected by the outer ear, transforms them into mechanical vibrations and transmits the vibrations to the ossicular chain. Changes of the structure and properties of the TM directly affect the sound transmission and may lead to conductive hearing loss. In addition, the response of the TM greatly influences the results of hearing screening and diagnosis tests. For example, in tympanometry the TM contributes more to the overall response than other middle-ear components do (e.g., Feldman, 1974). Thus, understanding the mechanics of the TM is essential for understanding conductive hearing loss and for designing better screening and diagnostic tests. It is also important for TM repair procedures and for improvement of the coupling between ossicular prostheses and the TM.

The small dimensions and non-uniform thickness of the TM make measurements of its mechanical properties very challenging. Added to these difficulties are the non-linear stress-strain relationship and strain-rate-dependent behaviour of the TM.

In the literature, various measurements of the mechanical properties of the TM have been reported, in association with various models. Békésy (1949) measured the elastic modulus (or Young's modulus) of the human TM using a bending test on a rectangular flap. Kirikae (1960) calculated the elastic modulus based on a dynamic test on a strip of fresh human TM. Decraemer et al. (1980a, 1980b) reported data on the viscoelasticity of the TM and presented non-linear elastic and non-linear viscoelastic structural models. Fay et al. (2005) applied several approaches to estimate the elastic properties of the TM. Cheng et al. (2007) conducted uniaxial tensile tests on strips of fresh human TMs to measure the stress-stretch relationship, stress relaxation under constant deformation, and mechanical strength. They also applied a non-linear elastic model to the experimental data to analyze the non-linear stress-stretch behaviour.

More recently, Huang et al. (2008) and Daphalapurkar et al. (2009) used a nanoindentation method to measure both in-plane and through-thickness viscoelastic properties of the posterior and anterior portions of the human TM. The applied deformations and resultant strains were small and linear. Luo et al. (2009a, 2009b) used a split-Hopkinson pressure bar to measure the strain-rate-dependent behaviour of the normal and diseased human TM at strain rates of 300–2000 s<sup>-1</sup> in the radial and circumferential directions. At these strain rates the reported stress-strain curves are linear except in the vicinity of failure strains. Zhang & Gan (2010) stimulated human TM specimens by sound pressure and measured the vibrations with a laser Doppler vibrometer. The sound pressure was 80 dB SPL, which is within the range of linear TM vibrations (e.g., Khanna and Tonndorf, 1972). Most recently, Aernouts & Dirckx (2012) performed *in situ* sinusoidal indentations on gerbil TMs at frequencies from 0.2 Hz to 8.2 Hz. The strain magnitudes were small enough that the responses were linear. In all of these recent studies,

therefore, the behaviour of the TM was effectively linear and linear viscoelastic models are applicable.

For large deformations, however, the TM displays both non-linear and viscoelastic behaviour. Previous finite-element models of the TM, however, have included either non-linear behaviour (e.g., Ladak et al., 2006; Qi et al., 2008) or viscoelastic behaviour (e.g., Zhang and Gan, 2010) but not both. In an earlier study (Charlebois et al., 2013) we investigated two approaches to modelling nonlinear viscoelastic behaviour numerically. In this study, we use one of those approaches to combine non-linear elasticity (hyperelasticity) and viscoelasticity of the TM in a non-linear viscoelastic (NLV) finite-element model. We validate our model against the viscoelastic relaxation data and the non-linear stretch data reported by Cheng et al. (2007), Our approach allows us to model both the loading and unloading curves, and the associated hysteresis, with a single set of parameters. We also estimate the energy dissipation as a function of frequency, and explore the effects of strain rate on the relaxation behaviour.

## 3.2 Methods

### 3.2.1 Experimental data

Details of the mechanical test procedures can be found in the paper of Cheng et al. (2007). Rectangular strips were cut from the posterior regions of human TMs, almost parallel to the manubrium, using a knife with two parallel blades 2 mm apart. The rectangular strips were flattened and mounted in a material-testing system and uniaxial tests were done.

The measurements were performed under controlled-deformation conditions. However, there is a discrepancy between their use of the term “strain rate” and their specification of  $\text{mm s}^{-1}$  as the units. Strain rate is defined as  $\dot{\varepsilon}_{i,j} = d\varepsilon_{i,j}/dt$  (in units of  $\text{s}^{-1}$ ) while in a controlled-deformation experiment an elongation rate  $\dot{l} = dl/dt$  (in units of  $\text{mm s}^{-1}$ ) is the input for the test. We have confirmed with them that the values given in their paper as 0.1 and 1.8  $\text{mm s}^{-1}$  were actually elongation rates and not strain rates. Strain rate is calculated by dividing the elongation rate by the initial length (i.e.,  $\dot{\varepsilon}_{i,j} = d\dot{l}/l_0$ ).

The lengths, widths and thicknesses of the 11 TM specimens were 5.0–8.5 mm (mean 6.44), 1.5–2.4 mm (mean 1.97) and 0.06–0.1 mm (mean 0.08 mm), respectively. Excluding a failure test that is not considered here, two testing protocols were performed by Cheng et al. (2007). First, in the standard uniaxial tensile test (stress-stretch relationship measured with displacement-ramp loading and unloading), the elongation rate was set at  $0.1 \text{ mm s}^{-1}$  and the maximum elongation was 15 % of the original length. Second, in the stress relaxation test (stress measured as a function of time with rapid displacement-ramp loading followed by maintenance of the displacement), the elongation rate was set at  $1.8 \text{ mm s}^{-1}$  and the maximum elongation was again 15 % of the original length (i.e., stretch = 1.15). Loading time and final length are calculated here based on average dimensions because the individual dimensions were not given by Cheng et al. (2007).

### **3.2.2 Finite-element model**

The TM is a complex structure composed of multiple layers (e.g., Lim, 1995). The orientation of collagen fibres in radial and circumferential directions in separate layers, in addition to a nonuniform thickness (e.g., Kuypers et al., 2006), make it inhomogeneous and anisotropic. However, no details are available concerning the thickness and other variations in the TM strips of Cheng et al. (2007). In this study, therefore, as in many other studies, the TM strips are assumed to be homogeneous and isotropic with constant thickness.

In addition, the TM is approximately conical so the rectangular strips of experimental specimens are not flat. For a flexible and thin membrane (thickness/width  $< 0.05$  and thickness/length  $< 0.02$ , for the average dimensions of the TM strips) the bending moments are of minor importance (Schomburg, 2011). Therefore, as in Cheng et al. (2007), we can neglect the effects of flattening the TM strips.

A three-dimensional finite-element model of a rectangular TM specimen has been created in order to simulate the experimental data. The length, width and thickness of the TM strip have been taken to

have the mean values mentioned above (6.44, 1.97 and 0.08 mm, respectively). Taking advantage of symmetry to reduce computational cost, just one eighth of the actual TM strip has been modelled. The model consists of 800 ( $20 \times 10 \times 4$ ) isoparametric eight-node hexahedral (brick) elements with linear shape functions (Fig. 3–1). Since the elements have a poor aspect ratio, a much finer mesh, with elements of the same type but having a 1:1:1 (cubic) aspect ratio ( $644 \times 196 \times 8$  elements), was used to evaluate the adequacy of the coarse mesh. The simulation results with the coarse mesh and with the finer mesh were found to differ by less than 2.4 %. The experiments are simulated by clamping one end of the model and displacing the other end by specified amounts.

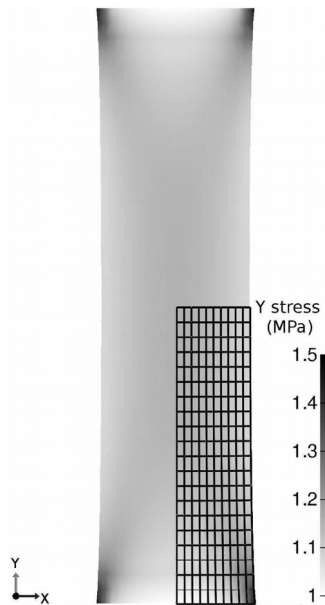


*Fig. 3–1. Meshed one-eighth model of a TM strip. Taking advantage of the symmetry of the strip, the overall stress distribution is determined based on that of the one-eighth model.*

The finite-element simulations are performed using the open-source software FEBio (Maas et al., 2012) (version 1.5.1) and its pre-processor Preview (version 1.4) and post-processor Postview (version 1.3.5). FEBio is a nonlinear finite-element solver specifically designed for biomechanical applications. It uses an implicit time-integration scheme with an incremental-iterative strategy based on Newton's method for nonlinear energy functions.

### 3.2.3 Constitutive equation

Different approaches have been used in the literature to derive the constitutive equations for non-linear viscoelastic materials. In this study we assume linear viscosity and non-linear elasticity (hyperelasticity). The material response is expressed as a convolution of a time-dependent component and an elastic component, similar to what is done for linear viscoelasticity. We refer here to this model as a non-linear viscoelastic (NLV) model. FEBio calculates the total second Piola-Kirchhoff stress tensor  $\mathbf{S}(t)$  by convolving a normalized relaxation function  $G(t)$  with the derivative of an elastic response function  $\mathbf{S}^e$ :

$$\mathbf{S}(t) = \int_0^t G(t-u) \left( \frac{d\mathbf{S}^e}{du} \right) du \quad (3-1)$$

where  $t$  is time and  $u$  is a dummy variable. The Prony series is a commonly used form for  $G(t)$ . This formulation not only facilitates interconversion of viscoelastic functions between the time and frequency domains but also increases the efficiency of discretization procedures in numerical methods (e.g., Taylor et al., 1970; Park and Schapery, 1999). Depending on whether  $\mathbf{S}^e$  represents the instantaneous or long-term elastic response,  $G(t)$  is given by either

$$G(t) = 1 - \sum_{i=1}^N g_i (1 - \exp(-t/\tau_i)) \quad (3-2)$$

or

$$G(t) = 1 + \sum_{i=1}^N g_i \exp(-t/\tau_i), \quad (3-3)$$

respectively. In both equations,  $g_i$  (relaxation coefficients) and  $\tau_i$  (time constants) are material parameters and  $N$  is the number of exponential terms.

Among the many constitutive models that have been proposed for hyperelastic materials, the Ogden

model is popular for biological tissues (e.g., Martins et al., 2006). According to this model, a strain energy  $W$  composed of deviatoric and volumetric energies (i.e., energies due to distortion and to change of volume, respectively) is defined by

$$W = \sum_{j=1}^M \frac{2\mu_j}{\alpha_j} [\bar{\lambda}_1^{\alpha_j} + \bar{\lambda}_2^{\alpha_j} + \bar{\lambda}_3^{\alpha_j} - 3] + W_{\text{vol}}(J), \quad (3-4)$$

where  $J = \lambda_1\lambda_2\lambda_3$  is the determinant of the elastic deformation gradient;  $M$  is the number of Ogden terms used;  $\bar{\lambda}_i = \lambda_i/J^{1/3}$  are modified stretches, where  $\lambda_i$  are the stretches;  $\alpha_j$  and  $\mu_j$  are material coefficients (with  $\mu_i > 0$  for thermodynamic consistency); and  $W_{\text{vol}}(J)$  is the volumetric part of the energy function. (This formulation is slightly different from that of Ogden (1972), where  $\alpha_j$  was used instead of  $\alpha_j^2$ . The difference between these two formulations was discussed by Charlebois et al. (2013).) In this study we use only a single Ogden term (i.e.,  $M = 1$ ).

Material parameters for a hyperelastic material can be determined by performing an unconfined tensile or compression test (to determine the deviatoric properties) and a confined compression test (to determine the volumetric part of the energy function). In the study from which we are taking our experimental data (Cheng et al., 2007), the mechanical tests were performed uniaxially on strips cut from TMs. Therefore, determining a volumetric response is not possible. Since soft tissue is generally assumed to be nearly incompressible (e.g., Humphrey, 2003), we model the TM as an incompressible material by setting the bulk modulus high enough to make  $W_{\text{vol}}$  negligible. For a uniaxial tensile test, the resultant stress is related to the stretch by

$$S_1^e = \frac{1}{\lambda_1} \frac{\partial W}{\partial \lambda_1}, \quad (3-5)$$

where the variables are the same as in Equations 3-1 and 3-4, and the subscript ‘1’ indicates the loading direction. Note that, although in Equation 3-1 the second Piola-Kirchhof stress is used for the

elastic response function (i.e.,  $\mathcal{S}^e$ ), the simulation output is given by FEBio as Cauchy (or ‘true’) stresses. Furthermore, the experimental data of Cheng et al. (2007) were reported as nominal stresses. Thus we convert all stress measures to Cauchy stresses,  $\sigma_1$ , for the purposes of our analysis. The second Piola-Kirchhof stress and the nominal stress can be converted to Cauchy stress for the case of uniaxial loading by

$$\sigma_1 = \lambda_1^2 S_1 \quad \text{and} \quad \sigma_1 = \lambda_1 P_1, \quad (3-6)$$

respectively, where  $P_1$  is the nominal stress.

### 3.2.4 Determination of model parameters

#### 3.2.4.1 Time-dependent part

A common practice is to take one time constant per decade of data along the logarithmic time axis (e.g., Knauss and Zhao, 2007). This corresponds to one time constant per decade in the frequency domain as well (e.g., Puso and Weiss, 1998; Charlebois et al., 2013). To estimate the parameters, we first digitized the mean normalized relaxation curve reported for nine TM specimens (Cheng et al., 2007, Fig. 8) at the fifteen points where mean values and standard deviation bars were reported. Based on the intervals between those data points (1 to 10 s) and on the relaxation duration (the stress relaxation reaches a relatively stable state in 120 s), a Prony series with three time constants (i.e.,  $1 \leq \tau_1 < 10$ ,  $10 \leq \tau_2 < 100$  and  $100 \leq \tau_3$ ) seems to be appropriate.

The Trust-Region non-linear least-squares method was used in the *cftool* curve-fitting function in Matlab version 7.8 (The MathWorks, Natick, MA) to identify material parameters. Each term in a Prony series involves the two parameters  $g_i$  and  $\tau_i$ , resulting in two degrees of freedom (DOFs). For the three-term series, two approaches have been taken, one with six DOFs (three time constants and three relaxation coefficients) and one with three DOFs (the three relaxation coefficients) and three time constants  $\tau_i$  that are predefined as 1, 10 and 100 s. The use of predefined time constants reduces the

computational cost and also reduces the need for defining constraints on the values of the parameters. To investigate whether three time constants are really required for the Prony series, series with one and two time constants (two and four DOFs respectively) were also fitted to the experimental data. We thus compared results for four Prony series.

#### *3.2.4.2 Elastic part*

As explained in 3.2.3, there are two possibilities for characterizing the elastic part in Equation 3–1: the instantaneous response or the long-term response (Equations 3–2 and 3–3, respectively). In these two limiting conditions, the viscous nature of the material does not contribute to the material response. However, because of practical limitations neither the instantaneous response nor the long-term response of a material is directly measurable (e.g., Wu et al., 2003).

According to the test protocol of Cheng et al. (2007), the loading time was approximately 10 s for the stress-stretch tests. Compared with the relaxation data, in which about 10 % of the stress is relaxed within 1 s, the 10-s loading time is not fast enough to be considered as an instantaneous response. It is also not slow enough to be considered as a long-term response because more than 100 s is needed to reach a plateau on the relaxation curve. Therefore, in the reported standard loading results the viscous behaviour of the material contributed to the shapes of the stress-stretch curves. If we obtain the elastic parameters by fitting the Ogden model to the loading data and then use these parameters as the instantaneous response for the elastic part of the non-linear viscoelastic model, the resultant stress-stretch curve will be lower than the experimental data. On the other hand, if the elastic parameters are used as the long-term response then the resultant stress-stretch curve will be higher than the experimental data. In either case, therefore, we must adjust the Ogden parameters to reproduce the experimental curves. We have chosen to take the elastic part of the model to be the instantaneous elastic response and the Prony series of Equation 3–2 is therefore used as the time-dependent part.

As usual in such cases, an iterative technique is used here to determine the elastic parameters of the formulation. We use a locally developed programme that minimizes an externally computed function using the algorithm of Hooke & Jeeves (1961). In this procedure, the initial values of the parameters  $\alpha$  and  $\mu$  are those obtained by curve-fitting without taking viscoelasticity into account, as described above. The function to be minimized is implemented as a Matlab script that invokes FEBio to run an NLV simulation for a given  $\alpha$  and  $\mu$  and then computes the root-mean-square error (RMSE) between the experimental data and the simulation results:

$$RMSE = \sqrt{\left( \frac{\sum_{i=1}^N (e_i - m_i)^2}{N} \right)} \quad (3-7)$$

where  $e_i$  and  $m_i$  are the experimental and modelling results, respectively, at points where mean values and standard deviations were reported, and  $N$  is the number of points. Starting values for the step size  $\Delta$  and minimum step size  $\delta$  must be defined. The subroutine is then called repeatedly until  $\Delta < \delta$ . Since the accuracy of the initial parameters was on the order of 0.01,  $\Delta$  and  $\delta$  were set to 0.01 and 0.001 respectively. For each function evaluation within the iterative minimization algorithm, the programme invokes the Matlab script and reads the resulting RMSE value. The iteration continues until the stopping criterion is met. The parameters obtained will be referred to below as adjusted Ogden parameters.

To determine what bulk modulus is required to enforce the assumption of incompressibility, we performed a sensitivity analysis to test how our model is affected by variations in the bulk modulus. We observed that for values of the bulk modulus greater than about  $10^3$  MPa (i.e.,  $K/\mu \approx 2500$ ) the output stress is constant to within less than 0.4 %, meaning that the TM is approximately incompressible.

### 3.3 Results

#### 3.3.1 Parameter identification

As described in 3.2.4, Prony series for the time-dependent part of the model were computed for one, two and three terms, with the three-term series having either six or three DOFs. These four sets of parameters are listed in Table 3–1. For each term of a Prony series, one time constant ( $\tau_i$ ) and one relaxation coefficient ( $g_i$ ) are required. For the six-DOF three-term series the  $\tau_i$  are fairly close to the values of 1, 10 and 100 s assigned for the three-DOF three-term series, and the corresponding values of  $g_i$  are very similar in the two cases. This supports the rationale for predefining the time constants. The root-mean-square errors (RMSE) are included as an indication of how much the fitted curves deviate from the experimental data points.

*Table 3–1 Calculated Prony-series parameters  $g_i$  and  $\tau_i$  for relaxation data. RMSE is the root-mean-square error between the fitted curves and the experimental data. Note that \* denotes a predefined value.*

Parameters	1 term	2 terms	3 terms	3 terms with predefined time constants
$g_1$	0.35	0.22	0.18	0.19
$\tau_1$ (s)	6.39	1.23	0.98	1*
$g_2$	–	0.13	0.08	0.07
$\tau_2$ (s)	–	42.4	6.6	10*
$g_3$	–	–	0.12	0.11
$\tau_3$ (s)	–	–	91.7	100*
RMSE	$37.\times 10^{-3}$	$4.0\times 10^{-3}$	$0.9\times 10^{-3}$	$1.7\times 10^{-3}$

Table 3–2. Calculated parameters  $l$  and  $a$  for the Ogden models for three individual TMs (TM#1–3) and the mean value of the stress-stretch relationship for eleven TM specimens from experimentally reported stress-stretch curves [Cheng et al., 2007, Figs. 4(a)–4(c) and 6(b)].

	Initial parameters			Adjusted parameters		
	$\mu$ (MPa)	$\alpha$	RMSE (MPa)	$\mu$ (MPa)	$\alpha$	RMSE (MPa)
TM#1 (Fig. 4a)	0.69	22.6	0.015	0.75	22.5	0.016
TM#2 (Fig. 4b)	0.30	29.6	0.012	0.33	29.3	0.011
TM#3 (Fig. 4c)	0.36	24.0	0.010	0.39	23.8	0.010
Mean (Fig. 6b)	0.38	28.6	0.029	0.40	28.8	0.025

The initial and adjusted Ogden parameters obtained for the loading curves of each of three individual specimens and for one mean curve for eleven specimens (Cheng et al., 2007, Figs. 4a,b,c and 6b) are listed in Table 3–2. In this table, the initial parameters are those obtained directly from a curve-fitting procedure without taking viscoelasticity into account, and the adjusted parameters are those obtained by the procedure explained in Section 3.2.4.2. The RMSE values indicate that we are able to account for the viscous effects without reducing the quality of the fit.

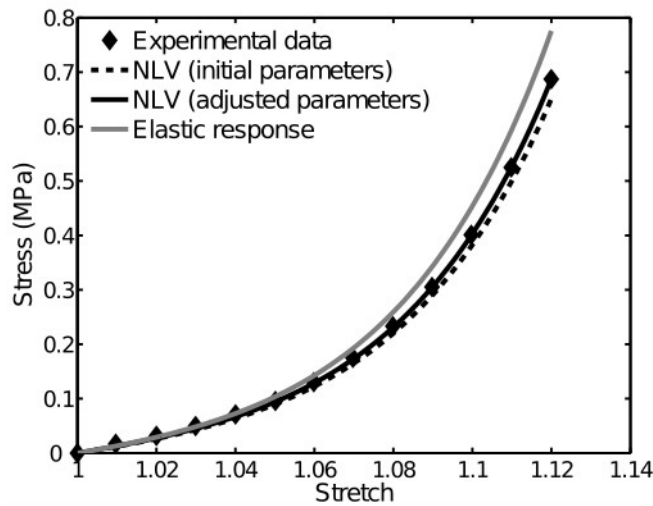


Fig. 3–2. Stress-stretch relationship for the mean experimental data of Cheng et al. (2007, Fig. 6) and for the NLV model with initial parameter values, with adjusted parameters, and with adjusted parameters but no relaxation (i.e., elastic response).

### 3.3.2 Simulated uniaxial tests

In Fig. 3–2, the mean values for the experimentally measured stress-stretch data of Cheng et al. (2007,

Fig. 6b) are shown together with the simulation results for the NLV model with both initial elastic parameters and adjusted elastic parameters. The stress values for the NLV model but with the initial elastic parameters are lower than the experimental data, while the NLV model with the adjusted elastic parameters matches the data well. An elastic response (with the adjusted elastic parameters but no relaxation) is also shown in Fig. 3–2; this response is, as expected, higher than the experimental data.

Fig. 3–3 shows the experimentally reported relaxation data of Cheng et al. (2007, Fig. 8) together with the simulated relaxation results of the NLV model with adjusted parameters, for one-term, two-term and three-term Prony series (after normalizing by the maximum stress). (Since, for the three-term series, the three-DOF version (with predefined time constants) and the six-DOF version produce very similar responses, for the sake of clarity only the three-DOF version is included in this figure.) It can be seen that the normalized stress for the one-term Prony series does not provide a good representation of the experimental data (with an RMSE of 3.7% of the normalized maximum stress) while the two-term and three-term Prony series match the experimental data quite well (with RMSE's of 0.4 and 0.17% of normalized maximum stress respectively).

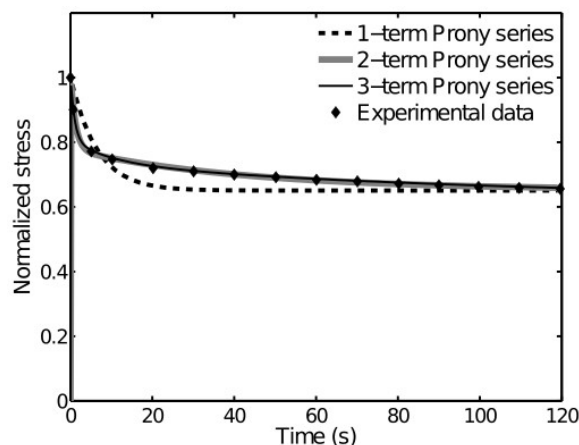


Fig. 3–3. Experimental data (Cheng et al., 2007, Fig. 8) and comparison with simulated relaxation tests with one-term, two-term, and three-term Prony series.

### 3.3.3 Loading and unloading curves

One of the important criteria in evaluating a viscoelastic model is its ability to predict both the loading

behaviour and the unloading behaviour with the same material parameters. Cheng et al. (2007, Fig. 4) reported loading and unloading curves for three individual TM specimens. Three sets of Ogden parameters were obtained based only on the loading curves of three individual TM specimens as explained in Section 3.2.4.2, for the elastic part of the model. Since no relaxation data were reported for individual specimens, the parameters of the 3-term Prony series, with predefined time constants, were obtained for average relaxation data for the viscous part of the model. The NLV model was then used to simulate the unloading behaviour. In Fig. 3–4 the three sets of experimental loading and unloading curves are shown together with the simulation results for the three corresponding NLV models. The simulation results match the experimental data quite well, the RMSE's of the combined loading and unloading curves being 1.5, 2.9 and 2.4% of the maximum stress magnitudes for TM's 1, 2 and 3 respectively. The most noticeable discrepancy is that the simulated unloading curves pass below the zero stress level; this is discussed in Section 3.4.

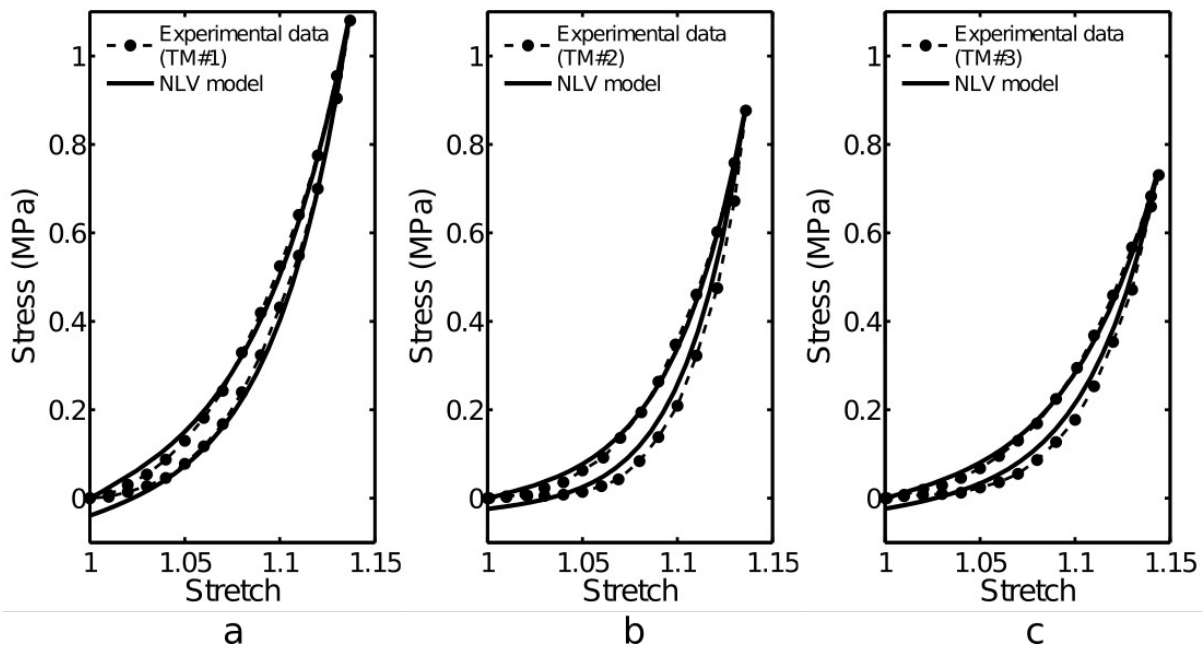


Fig. 3–4. Experimental data for three individual TM specimens reported by Cheng et al. [2007, Figs. 4(a)–4(c)] compared with simulated results from NLV model.

Note that, although the elastic parameters of the three TMs were obtained from the individual loading curves of the three reported samples, the viscous parameters were obtained from the mean relaxation curves for nine TMs, because individual relaxation curves were not available. In addition, the simulated loading and unloading times were calculated based on the average dimensions of the eleven specimens of Cheng et al. (2007) because the dimensions were not reported for individual specimens. This use of mean data to determine the parameters of individual models may account for some of the discrepancies seen in Fig. 3–4.

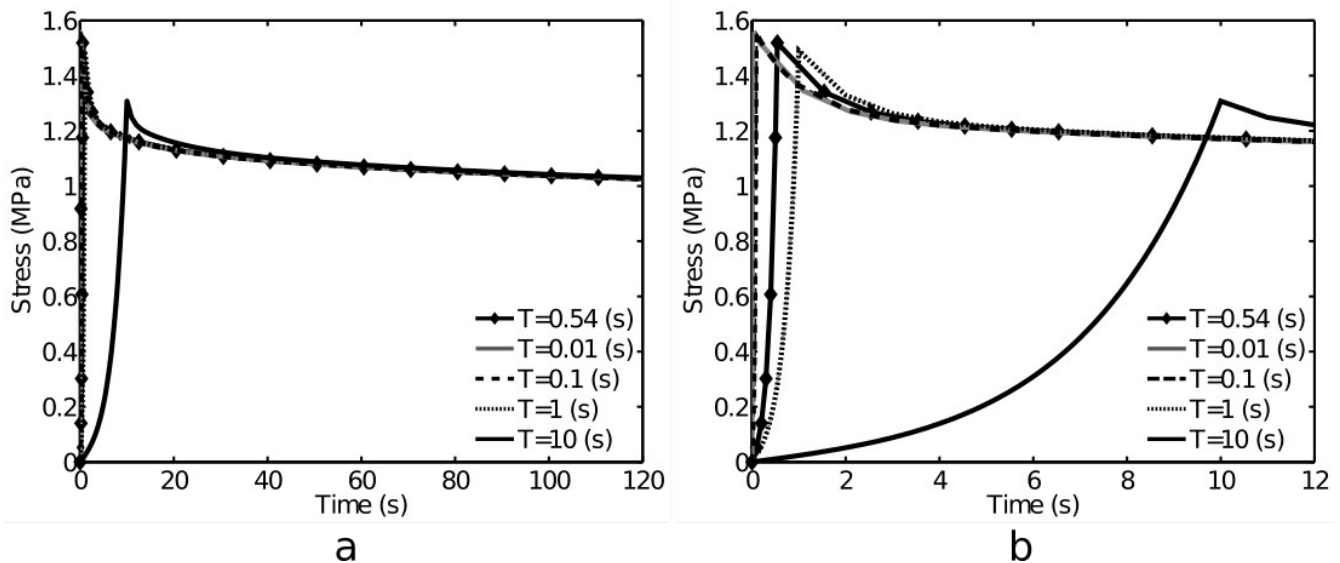


Fig. 3–5. Effect of loading time on simulated relaxation response of TM strips. (a) Full duration of measurements (120 s), showing lack of long-term differences. (b) Expanded view of first 12 s of response, emphasizing the short-term differences.

### 3.2.4 Strain-rate effect

In the experimental relaxation curve (Fig. 3–3), the normalized stress decreases by almost 10 % in less than 1 s after the peak. Since according to the experimental protocol described by Cheng et al. (2007) the loading time was  $\sim 0.54$  s, the results might have been significantly affected by the relaxation that occurred during the loading time. We have investigated the sensitivity of the NLV model to strain rate by varying the loading time (the time required to apply the specified deformation in the relaxation test) in simulations. As shown in Fig. 3–5a, the long-term response of the model is not affected by changing

the loading time. The short-term response, however, is affected as shown in Fig. 3–5a and more clearly in Fig. 3–5b, which focuses on the first 12 s, where the peak stress changes by less than 2.5% for loading times between 0.01 and 0.54 s.

### 3.4 Discussion

#### 3.4.1 Non-linear viscoelastic model in the frequency domain

It is often instructive to explore the implications of a viscoelastic model in the frequency domain. For example, Fung (1993) showed, for a linear viscoelastic model with one-time constant, that at low frequencies the Young’s modulus remains constant at its static value, but at a certain critical frequency the modulus rises sharply before settling at a new high-frequency value. For a non-linear viscoelastic model, Charlebois et al. (2013) reported that the stored energy shows a similar stiffening pattern over the frequency domain.

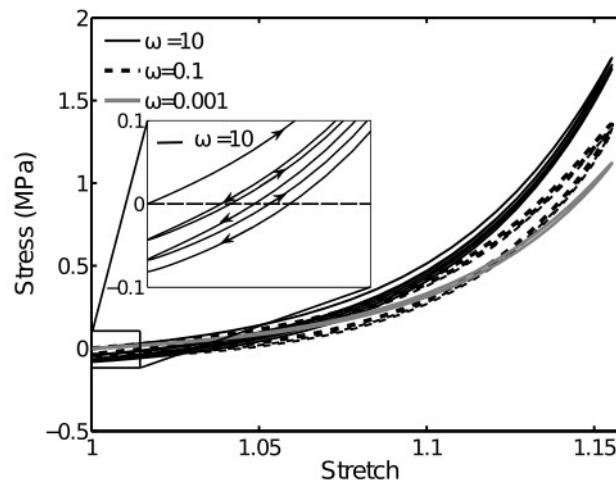


*Fig. 3–6. Frequency effects on stress-stretch relationship. The first three cycles of hysteresis loop are shown for each of three circular frequencies. The inset shows a magnified view of the area around the origin of the stretch and stress axes for  $\omega = 10$  rad/s, to demonstrate the changes in the loading and unloading paths from one cycle to the next.*

To demonstrate how stress-stretch relationships and hysteresis loops are affected by the loading frequency, a harmonic displacement-controlled loading condition was modelled at three circular

frequencies, 0.001, 0.1 and 10 rad/s, for a three-term Prony series. The results are shown in Fig. 3–6. Note that the maximum stress magnitude for the frequency of  $\omega = 10$  rad/s is higher than that for the frequencies of  $\omega = 0.1$  and .001 rad/s, which demonstrates that this viscoelastic model behaves more stiffly at high frequencies than at low frequencies. It can be shown that the maximum stress magnitude approaches plateaus at the lower and upper frequencies (i.e.,  $\sim 0.001$  and 10 rad/s respectively), as described in the previous paragraph. In addition, it can be seen that the area inside the hysteresis loop (i.e., the area between the loading and unloading curves, representing lost energy) is larger at the middle frequency (i.e.,  $\omega = 0.1$  rad/s) than at the upper and lower frequencies (i.e.,  $\omega = 10$  and 0.001 rad/s, respectively). (The lost energy spectra in the frequency domain will be discussed below in more detail.)

At each frequency, a steady state is obtained after a few cycles of loading and unloading. The number of cycles required to reach steady state is smaller at low frequencies than at high frequencies (cf. Schatzmann et al., 1998; Charlebois et al., 2013). Fig. 3–6 shows that the steady-state closed loops are reached within the first cycle for the lowest frequency and are almost reached by the third cycle for the middle frequency, but are not yet reached after three cycles for the highest frequency.

As mentioned in the Methods, it is very common to choose one relaxation time per decade of data. If we plot each  $g_i$  as a function of its inverse associated time constant  $\tau_i$  on a frequency axis, we will have a spectrum of relaxation function  $g_i(1/\tau_i)$ . As we increase the number of time constants this spectrum  $g_i(1/\tau_i)$  becomes more uniform (e.g., Fung, 1993), which is desirable for describing the usual time-dependent behaviour of biological tissues. Thus, although two time constants seem to fit the relaxation data as well as three (Fig. 3–3), a three-time-constant series is probably a better choice to model the TM. To illustrate this, Fig. 3–7a shows lost-energy spectra calculated from hysteresis loops using the method described by Charlebois et al. (2013). The lost-energy spectra were computed for the viscous

parameters shown in Table 3–1 (i.e., for one-term, two-term and three-term Prony series, with pre-defined time constants for the latter) and the elastic parameters shown in Table 3–2 (i.e., the adjusted parameters for the mean elastic response of Cheng et al., 2007 Fig. 6b). As seen in this figure, increasing the number of Prony-series terms results in a more uniform lost-energy spectrum over the frequency range of approximately 0.006 to 4 rad/s.

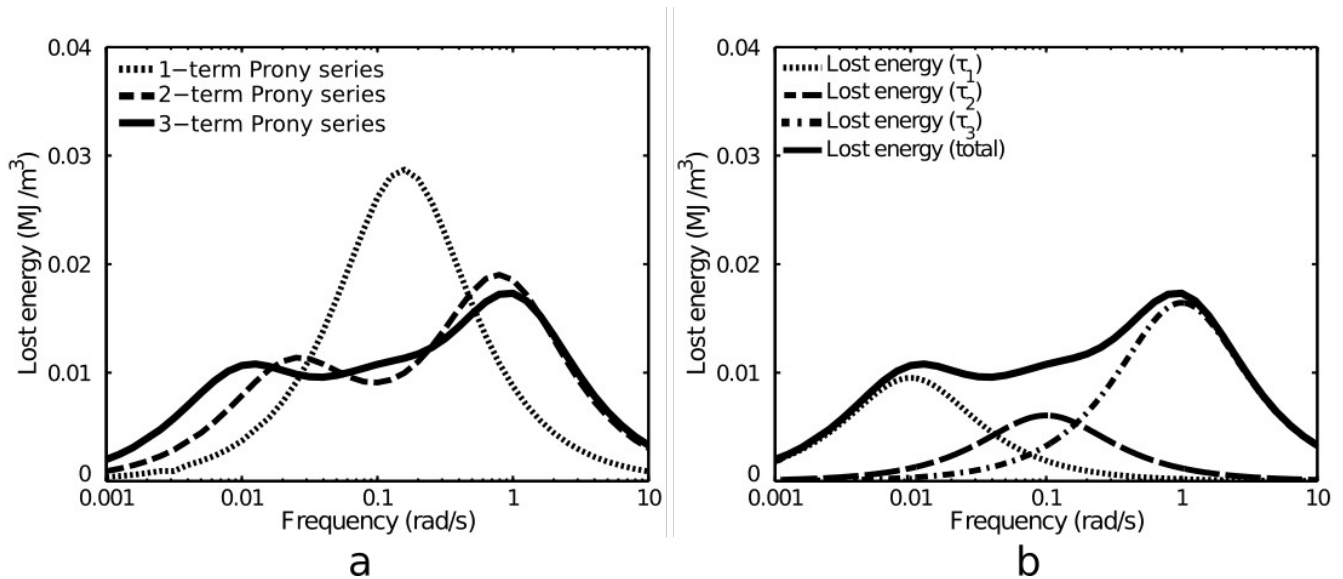


Fig. 3–7. Lost-energy spectrum in frequency domain for one-term, two-term and three-term Prony series. (b) Lost energy due to each term in the three-term Prony series (i.e., due to  $\tau_1$ ,  $\tau_2$ , and  $\tau_3$ ) and total lost energy.

In addition, Fig. 3–7 demonstrates that at low frequencies (i.e.,  $\omega < 0.001$  rad/s) and high frequencies (i.e.,  $\omega > 10$  rad/s) the lost energy becomes small. This means that the model behaves like an elastic material at frequencies far beyond these values, so it will no longer be sensitive to strain rate. This explains why the relaxation behaviour of this model is not sensitive to loading rates higher than  $10 \text{ s}^{-1}$  (i.e., loading times less than 0.1 s, as shown in Fig. 3–5).

For a linear viscoelastic model, a complex dynamic modulus is defined which is composed of storage and loss components (Mase and Mase, 1999). It can be shown that, for a linear viscoelastic model with a Prony series representing the viscous part, the peaks of the loss modulus and of the lost-

energy spectrum occur at the same frequencies (e.g., Park and Schapery, 1999). Such a modulus is not defined for a non-linear viscoelastic model, but the lost-energy spectrum peaks for the non-linear viscoelastic model occur at the same frequencies as are predicted by a linear viscoelastic model with the same viscous parameters. To demonstrate the contribution of each term of the Prony series to the total lost-energy spectrum, the model with a three-term Prony series is analyzed separately in Fig. 3–7b. As this figure shows, each term has a peak occurring at an angular frequency corresponding to the inverse of its time constant (i.e.  $\omega_1 = 1/\tau_1 = 1$ ,  $\omega_2 = 1/\tau_2 = 10$  and  $\omega_3 = 1/\tau_3 = 100$ ). Note the height of each peak depends on the value of the associated  $g_i$ .

### **3.4.2 Loading and unloading loops**

As a result of viscoelastic processes, at the end of each unloading process the length of the TM strip would tend to be longer than its initial length. This means that to force the specimen back to its initial length we would need to apply a compressive stress. In the experimental tests, the TM strips do not resist the compression and some local buckling happens, so the loading and unloading curves form a closed loop. However, with the numerical model no buckling occurs and, as Fig. 3–4 shows, for a single cycle the loading and unloading curves do not form a closed loop. Loading and unloading loops approach a closed configuration over a number cycles, as discussed above in connection with Fig. 3–6.

### **3.4.3 Conclusions**

The material parameters (Tables 3–1 and 3–2) for a nonlinear viscoelastic model of human TM were derived from experimental data reported by Cheng et al. (2007) and the model is able to reproduce the results of their mechanical tests. Most significantly, this allows us for the first time to model both a loading curve and the corresponding unloading curve with a single set of parameters.

This model is suitable for large deformations of the TM and for frequencies in the range of about 0.003 to 3 rad/s (approximately 0.001 to 0.64 Hz). These conditions correspond to those involved in

tympanometry, in which a large sweeping ear-canal pressure (e.g.,  $-300$  to  $+200$  daPa) is applied in less than 10 s.

### **3.5 Acknowledgements**

This work was supported by the Canadian Institutes of Health Research and the Natural Sciences and Engineering Research Council of Canada.

# **Chapter 4: Finite-element modelling of the acoustic input admittance of the newborn ear canal and middle ear**

To be submitted to the *Journal of the Association for Research in Otolaryngology*.

## **Preface**

The study presented in the previous chapter was relevant to the response of the tympanic membrane to the static pressures used in tympanometry. The studies presented in this chapter and the following chapter, on the other hand, are relevant to the response of the ear to the probe tones used in tympanometry.

The wideband immittance data in newborns are affected by many factors, thus outputs are difficult to interpret. In this paper a finite-element model of the newborn outer- and middle-ear models is presented. At low frequencies, due to the long wavelength of the sound pressures, the ear structure can be treated as lumped elements. In this study, we modelled the newborn outer- and middle-ear models and investigated the contribution of each component to the overall admittance response quantitatively in a range of frequencies up to 2 kHz. The model shows that at frequencies below 1000 Hz admittance measurements are highly affected by the canal response and they cannot satisfy their main goal of reporting the middle-ear response. The response of the ear canal becomes negligible at frequencies in the vicinity of the middle-ear resonance (i.e., between 1000 and 2000 Hz). However the resonance frequency may vary considerably due to intersubject variability. This suggests that admittance measurements can provide more information about the condition of the middle-ear when they are made at multiple frequencies above 1000 Hz.

## **Abstract**

Admittance measurement is a promising tool for evaluating the status of the middle ear in newborns. However, the newborn ear is anatomically very different from the adult one and the acoustic input admittance is different than in adults. To aid in understanding the differences, a finite-element model of the newborn ear canal and middle ear was developed and its behaviour was studied for frequencies up to 2000 Hz. Material properties were taken from previous measurements and estimates, and the sensitivities of the models to these different parameters were examined. The simulation results were compared with measurements made in newborns. The model produces results that are within the range of the measured data and permits investigation of the separate contributions of the outer and middle ear. The results suggest that admittance measurements can provide more information about the condition of the middle-ear when made at multiple frequencies around its resonance.

## **4.1 Introduction**

Hearing loss is considered to be one of the most common birth defects in newborns – about 3 in 1000 babies are born with some degree of hearing impairment (e.g., Akinpelu et al., 2014). Early detection of hearing loss accompanied by appropriate early intervention is important in order to avoid problems associated with language development that affect daily communication, educational achievement, psychosocial development and later employment opportunities (e.g., Joint Committee on Infant Hearing 1994 Position Statement; American Academy of Pediatrics, 2007). Hearing loss is either conductive, involving the outer and/or middle ear, or sensorineural, involving the inner ear, auditory nerve and/or brain. Most permanent newborn hearing loss is sensorineural but its detection and diagnosis are often affected by transient conductive losses (e.g., Akinpelu et al., 2014).

Currently, otoacoustic emission (OAE) and/or auditory brainstem response (ABR) tests are employed as screening tools in newborn hearing screening programs. High false-positive rates of

screening tests are an important concern with universal newborn hearing screening. Many false positives can be attributed to transient conditions in the external ear (e.g., collapse of the ear canal and the presence of debris) and middle ear (e.g., presence of amniotic fluid and mesenchyme) in the first 48 hours postpartum (e.g., Akinpelu et al., 2014), which conflicts with the desire for shorter hospital stays. It would thus be very valuable to be able to quickly identify conductive losses right at the time of initial screening, just after birth.

Tympanometry is a promising tool for assessing middle-ear status. In this method the acoustical input immittance of the outer and middle ear is measured in response to a probe tone, in the presence of a range of quasi-static air pressures in the ear canal. Immittance refers to either admittance  $Y$ , which is volume velocity divided by sound pressure, or impedance  $Z$ , the reciprocal of admittance. Both admittance and impedance are complex numbers, the former being composed of a real part  $G$ , conductance, and an imaginary part  $B$ , susceptance, and the latter being composed of a real part  $R$ , resistance, and an imaginary part  $X$ , reactance. Measurements of the separate real and imaginary parts (or, equivalently, of the magnitude and phase) contain more information about the middle ear than just the magnitude alone, but much remains to be understood about what they mean and how to interpret them.

Tympanometry is most often done with a 226-Hz probe tone. This frequency provides easy-to-interpret results for adult ears but the results in newborns are very different from those in adults. The differences may be attributed to anatomical and physiological differences occurring during maturation (Saunders et al., 1983; Eby and Nadol, 1986; Qi et al., 2006, 2008). For example, the newborn ear-canal wall is not ossified and is surrounded along most of its length by soft tissue (e.g., Standing, 2008, chap. 36). This causes the newborn canal to be very compliant. In adults, only the most lateral third of the canal wall is composed of soft tissue, while the medial two-thirds of the canal is encompassed by temporal bone (e.g., Anson and Donaldson, 1992, p. 146). In addition, the orientation,

shape and ultrastructure of the tympanic membrane (Ruah et al., 1991) and ear canal (e.g., Saunders et al., 1983, p. 4) undergo dramatic changes during growth, especially in the first months after birth. It has been known for some time that a 1-kHz tone provides better differentiation between normal and liquid-filled newborn middle ears, but the differentiation is still far from perfect (e.g., Shahnaz et al., 2008). Furthermore, the fact that the main middle-ear resonance is in the vicinity of 1.8 kHz (Keefe et al., 1993) suggests that the measurements may be quite sensitive to what frequency is used and where the resonance is in a given ear. More information can be obtained by using multiple frequencies (e.g., Alberti and Jerger, 1974; Colletti, 1975; Funasaka et al., 1984; Keefe and Levi, 1996; Shahnaz et al., 2008). A number of groups have evaluated wideband measurements of immittance in newborns, whether unpressurized (e.g., Keefe et al., 1993) or pressurized (e.g., Holte et al., 1991; Sanford and Feeney, 2008).

In addition to immittance, it is also possible to characterize the ear in terms of energy reflectance (ER), the ratio of the reflected energy to the incoming energy, or absorbance (EA), equal to  $1-ER$ . It has been assumed, at least for adults, that the ER measured in the ear canal represents the condition at the TM, independent of the location of the probe tip, based on the following approximations: (1) the energy loss of the sound wave in the enclosed air in the canal is negligible; (2) the ear canal acts like a smoothly varying transmission line (i.e., no significant energy is reflected from abrupt changes in the canal cross-section); and (3) the energy loss at the canal wall is negligible (e.g., Voss and Allen, 1994). The first two assumptions are reasonable for both adults and newborns (e.g., Eby and Nadol, 1986). The third assumption, however, is probably not valid for newborns because, as stated above, the canal wall is composed of soft tissue, so sound energy is absorbed within it (e.g., Keefe and Levi, 1996). Merchant et al. (2010) conducted a series of wideband energy measurements to define the normative energy response of the ear of newborns and infants.

The middle ear is a complex 3-D mechano-acoustical system containing many interconnected,

highly irregular, asymmetrical and non-uniform components. There are many parameters that affect clinical measurements, and the contribution of each parameter to the output is difficult to identify (e.g., Sanford and Feeney, 2008). The finite-element method can be utilized to provide a quantitative understanding of such a system. In this method, a complicated system is divided into a large number of relatively simple elements. A finite-element model is defined in terms of anatomical and biomechanical parameters that have very direct relationships to the structure and properties of the system (e.g., Funnell et al., 2013).

Funnell and Laszlo (1978) introduced the finite-element method to middle-ear modelling. Since then this method has been widely used to investigate different aspects of both human and animal ears (e.g., Wada et al., 1992; Ladak and Funnell, 1996; Koike et al., 2002; Gan et al., 2004; Motallebzadeh et al., 2013. Qi et al. (2006; 2008) developed nonlinear finite-element models of the newborn ear canal and middle ear. They reported the displacements of these models under static pressures in the range of those induced during tympanometry and calculated the ear-canal and middle-ear compliances.

In this study, we have developed linear finite-element models of the newborn ear canal and middle ear and analyzed their responses to sound frequencies up to 2000 Hz. (Preliminary versions of this model were described by Gariepy (2010) and Motallebzadeh et al. (2013b). We set the upper limit of the frequency range to 2000 Hz because at higher frequencies the input immittance is influenced by the spatial variation of sound pressure along the canal and the associated standing waves (e.g., Shanks and Lilly, 1981; Stinson et al., 1982), so it becomes more sensitive to the position of the probe tip inside the ear canal (e.g., Keefe et al., 1993; Voss and Allen, 1994). The input admittances of the ear canal and middle ear were calculated separately and then combined to give the overall admittance of the ear. This approach, as discussed in Section 4.2.6, makes it possible to investigate the individual contributions of the outer ear and middle ear to the overall response. The results are validated in comparison with previously reported clinical data. In addition, the effects of material-property parameters are explored.

## 4.2 Materials and methods

### 4.2.1 3-D geometry and finite-element mesh

The ear-canal and middle-ear models are revised and refined versions of those of Qi et al. (2006; 2008). The geometries are based on a clinical X-ray CT scan (GE LightSpeed16, Montréal Children's Hospital) of a 22-day-old newborn's right ear. The scan had a pixel size of 0.187 mm and a slice thickness of 0.625 mm with a 0.125-mm overlap, resulting in a slice spacing of 0.5 mm. Three locally developed programs, Fie, Tr3 and Fad (<http://www.audilab.bme.mcgill.ca/sw/>), were used to generate a surface model. Gmsh (<http://www.geuz.org/gmsh/>) was then used to generate 3-D solid models with tetrahedral elements for each individual component of the ear-canal and middle-ear models. The solid models were then assembled in Fad (Fig. 4-1).

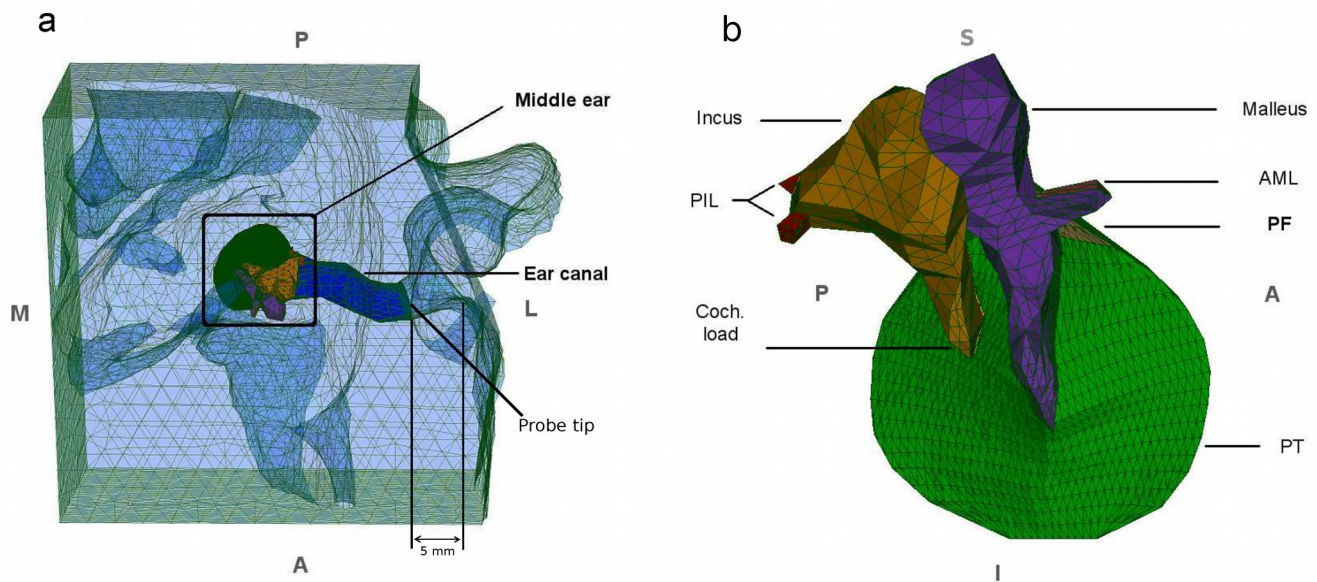


*Fig. 4-1. Meshed geometry of the finite-element model. (a) Superior view of the overall model including the ear canal, surrounding soft tissue and middle ear. (b) Expanded medial view of the middle-ear model, with the TM annulus almost parallel to the page. (PIL = posterior incudal ligament; AML = anterior malleolar ligament; PT = pars tensa; PF = pars flaccida; S = superior; I = inferior; M = medial; L = lateral; A = anterior; P = posterior)*

The canal model consists of the soft tissue surrounding the lumen of the ear canal. The interiors of bony structures in the region have not been included in the ear-canal model, but their surfaces are

included and are considered as rigid boundary conditions for the model. A probe tip is represented in the model by a small block located 5 mm inside the ear-canal entrance (Fig. 4–1 and also Qi et al., 2006, Fig. 4–2), based on the estimate of the clinical situation by Keefe et al. (1993, Table I), and tightly connected with the surrounding tissue in order to simulate a hermetic seal.

The middle-ear model consists of the tympanic membrane (TM), the malleus and incus, the anterior malleolar ligament (AML) and the two bundles of the posterior incudal ligament (PIL). The incudomalleolar joint is assumed to be fused so there is no relative motion between the malleus and incus. This simplification was also used in the newborn middle-ear model of Qi et al. (2008) and in the adult human model of Eiber (1999).

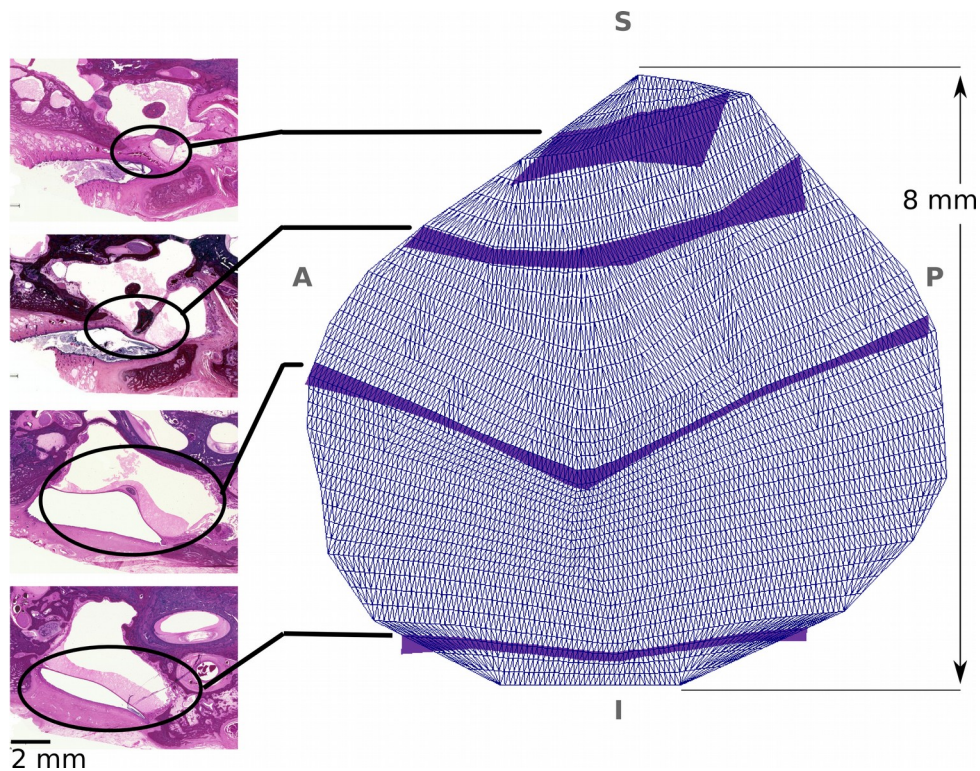


*Fig. 4–2. Thickness map of the TM. Four 20-µm-thick serial histological sections from a three-week-old infant (left) from which the thicknesses of the TM were derived for the finite-element model (right).*

The thickness of the TM was measured from a set of 26 20-µm-thick serial histological sections from a three-week-old newborn. In our CT scan there were 11 slices containing the TM, and 11 approximately corresponding slides were selected from the histology images. The thicknesses were

measured at several points using the Measure tool in GIMP, a free (libre) and open-source image-manipulation programme (<http://www.gimp.org>), then a piecewise cubic Hermite interpolation algorithm (MATLAB, Release 2012b, The MathWorks, Inc., Natick, Massachusetts, United States) was used to determine a thickness distribution over the cross-section of the TM surface at each slice. The thicknesses were applied manually in the segmentation software (Fie) to generate the 3D geometry of the TM. Four of the 11 histological images and corresponding cross-sectional thicknesses on the TM model are presented in Fig. 4–2. The measured thickness of the posterior-superior quadrant varies between 0.15 and 0.6 mm and that of the other three quadrants varies between 0.07 and 0.4 mm (the higher value in each quadrant corresponding to the TM annulus). The pars flaccida thickness (0.5–2 mm) is significantly greater than that of the pars tensa. These thicknesses for the TM are consistent with the findings of Ruah et al. (1991).

## **4.2.2 Material properties**

### *4.2.2.1 Introduction*

The probe tone in tympanometry typically has an amplitude of around 95 dB SPL (~1.1 Pa) or less (e.g., Alberti and Jerger, 1974) and does not cause deformations that are large enough to push the system into its nonlinear range. In fact, according to the model of Qi et al. (2008), the onset of nonlinearity seems to occur at approximately 1000 Pa in both the ear canal and the middle ear. Thus, in this study all materials are assumed to be linear elastic.

Since precise values for the material properties of newborn ear-canal and middle-ear components are not available, ranges of plausible values are used. For each material property, upper and lower limits were defined based on structural similarities between different tissues (e.g., skin and the pars flaccida) and/or on reported values for the adult ear. Each baseline material property is approximately the arithmetic mean of the upper and lower limits for that property. Thus, three models each are generated

for the ear canal and the middle ear: (a) a low-impedance model (i.e., a model with the lowest stiffness, density and damping values for all components); (b) a baseline model (i.e., a model with baseline parameter values); and (c) a high-impedance model (i.e., a model with the highest stiffness, density and damping values for all components). Taking all possible combinations of the ear-canal and middle-ear models, nine scenarios were considered for the whole-ear response in this study.

#### *4.2.2.1 Stiffness*

##### **4.2.2.1.1 Pars tensa**

Volandri et al. (2011) and Maftoon et al. (2015) recently reviewed the Young's moduli that have been reported for the pars tensa in the literature. A Young's modulus of 20 MPa has frequently been used for the pars tensa in numerical models (e.g., Funnell and Laszlo, 1978; Gan and Sun, 2002); Young's moduli half as large and twice as large (i.e., 10 and 40 MPa) are still within the range of experimental measurements (e.g., Békésy, 1949; Kirikae, 1960; Decraemer et al., 1980b; Cheng et al., 2007; Huang et al., 2008; Luo et al., 2009a; Aernouts et al., 2012; Zhang and Gan, 2013).

Ruah et al. (1991) reported morphological changes of the TM during post-natal development and investigated the similarity between age-related ultra-structural changes of the TM and changes observed in human skin. The age-related changes of human skin have been reported in several studies and have been attributed to the water content of the skin and to the orientation and density of the collagen fibres (e.g., Yamada and Evans, 1970; Rollhäuser, 1950). Rollhäuser (1950) reported that the Young's modulus for the skin of babies of less than 3 years old is 3–5 times smaller than that of adults. Based on these studies, we used Young's moduli of 2, 6 and 10 MPa in our models. These values are approximately 3–5 times smaller than the lower, middle and upper values of the reported pars-tensa Young's moduli mentioned above.

Qi et al. (2008) used Young's moduli of 0.6, 1.2 and 2.4 MPa in their static model. Considering the

report of Luo et al. (2009a, 2009b), which states that the Young's modulus of the normal TM in dynamic conditions is more than twice that in static ones, our values are consistent with those of Qi et al.

#### 4.2.2.1.2 Pars flaccida

The pars flaccida is considered to be the extension of the skin of the external ear canal (Lim, 1970). Based on this observation, Maftoon et al. (2015) used a Young's modulus of 2 MPa for the gerbil pars flaccida, in the range of the reported Young's moduli of the human epidermis and stratum corneum (Geerligts et al., 2011). They also used a simplistic model of a circular plate to validate their value by comparing the results with their own experimental data from laser Doppler vibrometry. In this study, we used Young's moduli of 0.4, 1.2 and 2 MPa for the pars flaccida. The 0.4 MPa value is approximately the Young's modulus of the skin as reported by Agache et al. (1980), and it is approximately 1/5 of the value used by Maftoon et al. (2015), consistent with the change of elastic modulus of the skin during maturation. The upper value was used in the model of Maftoon et al. (2015). The middle value is approximately 1/3 of our baseline value of the pars tensa Young's modulus, a pars-flaccida/pars-tensa stiffness ratio that has been used in other modelling studies (e.g., Lesser and Williams, 1988; Koike et al., 2002).

#### 4.2.2.1.3 Ear canal

The newborn ear canal is surrounded by elastic cartilage, skin, glandular tissue and fat (e.g., Gulya, 1995). In adults the ear canal is mainly surrounded by bone, whereas in newborns the canal is surrounded almost entirely by soft tissue (e.g., McLellan and Webb, 1950). To the best of our knowledge, the stiffness of human newborn elastic cartilage has never been reported in the literature. Elastic cartilage is the least stiff type of cartilage in the human body (Fung, 1993, p. 519). Young's moduli of 0.33–5.8 MPa have been reported for different adult human articular cartilages (e.g., Hayes

and Mockros, 1971). As a collagenous tissue, cartilage undergoes significant alterations from newborn to adult (e.g., Williamson et al., 2001), similar to the skin and pars tensa. Thus, the stiffness of the articular cartilage in newborns can be expected to be less than the values mentioned above by a factor of perhaps 3–5, giving a range of about 0.11–1.9 MPa, and the stiffness of the elastic cartilage would be expected to be less than these values.

Qi et al. (2006) used Young's moduli of 30, 60 and 90 kPa for the soft tissue in their static model. In this study, we used Young's moduli of 20, 210 and 400 kPa for the soft tissue. The lowest value is approximately the mean of the Young's moduli of fat and glandular tissue (Wellman et al., 1999) and the upper value corresponds to the Young's modulus of skin in young adults (less than 30 years old) as reported by Agache et al. (1980).

#### 4.2.2.1.4 Ossicles

Various values for the Young's modulus of compact bone have been reported in the literature. Fung (1993, p. 511) reported a range of 17.6–18.9 GPa and stated that the mechanical properties of bone vary with age, sex, location in the body, orientation of the load, and strain rate. Most recently, Soons et al. (2010) measured Young's moduli of  $16 \pm 3$  GPa for the rabbit incus and malleus. Qi et al. (2008) used Young's moduli of 1, 3 and 5 GPa in their model. In this study, Young's moduli of 4, 10 and 16 GPa were applied to the ossicles, where the lower value corresponds to the lowest Young's moduli in the literature review of Funnell et al. (1992); the upper value corresponds to the average value in the measurements of Soons et al. (2010); and 10 GPa is the mean of these two values. It turns out that this parameter has very little effect on the behaviour of the model.

#### 4.2.2.1.5 Ligaments

In previous adult models, Young's moduli of 0.65 to 21 MPa have been used for middle-ear ligaments (e.g., Koike et al., 2002; Gan et al., 2004). Maftoon et al. (2015) used the same Young's moduli for the

ligaments as for the pars tensa, based on their structural similarities. Qi et al. (2008) used 1, 3 and 5 MPa in their newborn model. For the ligaments in this study we applied the Young's moduli of the pars tensa, namely, 2, 5 and 8 MPa.

The stapedial annular ligament was represented in our model by a translational spring element, at the same place where the dashpot is located. Gan et al. (2011, Fig. 6a) reported load-displacement curves for two adult human stapedial annular ligaments. In the linear region of their loading and unloading curves (i.e., for displacements  $< 0.1$  mm), we estimated that the stiffness was between 100 and 300 N/m. Cancura (1979) reported a stiffness of 182 N/m, and more recently Lauxmann et al. (2014) reported this stiffness to be 1050 N/m based on load and displacement measurements. They also compared their result to the value of 182 N/m and 940 N/m reported by Cancura (1979) and Waller (2002), respectively. Based on these values, we used stiffness parameters of 200, 600 and 1000 N/m in this study.

#### *4.2.2.2 Poisson's ratio*

Soft tissues are nearly incompressible, so values close to 0.5 are appropriate for their Poisson's ratio (e.g., Decraemer and Funnell, 2008). In this study the value of 0.49 was used for the soft tissues to avoid numerical problems arising from full incompressibility. For bones, a Poisson's ratio of 0.3 was used in this study, which is widely accepted (Cowin, 2001, chap. 23.18) and has often been used in numerical models of the middle ear (e.g., Koike et al., 2002).

#### *4.2.2.3 Density*

The density of soft tissue is usually considered to be somewhere between that of water ( $1000 \text{ kg/m}^3$ ) and that of dry collagen fibres ( $1200 \text{ kg/m}^3$ ). In this model, densities of 1000, 1100 and  $1200 \text{ kg/m}^3$  were used for the soft-tissue components. Fung (1993, p. 512) reported bone density as being between 1600 and  $1950 \text{ kg/m}^3$ . Based on this, densities of 1600, 1800 and  $2000 \text{ kg/m}^3$  were used for the malleus

and incus in this model. This is close to the range that Maftoon et al. (2015) used for the malleus, incus and stapes.

Wever and Lawrence (1954, p. 417) reported the mass of the stapes to be in the range of 2.0 to 4.3 mg (mean 2.86). Since our 3-D geometry did not include the stapes, its mass was represented by a discrete mass element of 2, 3 or 4 mg at the same location where the spring and dashpot were attached to the incus.

#### 4.2.2.4 Damping

The damping of a mechanical system is more difficult to understand than its mass or stiffness since it deals with internal friction and energy dissipation, processes that are difficult to isolate and measure. Several empirical models have been proposed for describing damping. One of the most common models is Rayleigh damping (e.g., Funnell et al., 1987). In this model, the damping matrix  $\mathbf{C}$  is generated by

$$\mathbf{C} = \alpha \mathbf{M} + \beta \mathbf{K}, \quad (4-1)$$

where  $\mathbf{M}$  and  $\mathbf{K}$  are the mass and stiffness matrices, respectively, and  $\alpha$  and  $\beta$  are the damping coefficients with units of  $s^{-1}$  and  $s$ , respectively. The damping ratio  $\zeta$  at each angular frequency  $\omega = 2\pi f$  is related to the Rayleigh damping coefficients by

$$\zeta = \frac{1}{2} \left( \frac{\alpha}{\omega} + \beta \omega \right). \quad (4-2)$$

This implies that  $\alpha$  corresponds to damping ratios that decrease with frequency while  $\beta$  corresponds to damping ratios that increase with frequency.

Previously used pairs of tympanic-membrane Rayleigh coefficients  $(\alpha, \beta)$  include  $(0, 1.0 \times 10^{-4})$ ,

(260,  $3.7 \times 10^{-5}$ ) and (0,  $0.75 \times 10^{-4}$ ) (Vollandri et al., 2011). For the frequency range of 50–2000 Hz that we use in our simulations, Equation 4–2 gives values of  $\zeta$  between 0.012 and 0.63 for these values of  $\alpha$  and  $\beta$ . Wada et al. (1992) estimated a damping ratio of 0.126 for frequencies less than 3 kHz. Maftoon et al. (2015) assigned stiffness-proportional damping (i.e.,  $\alpha = 0$ ) with  $\beta = 2 \times 10^{-6}$  s,  $3 \times 10^{-5}$  s and  $2 \times 10^{-7}$  s for the soft tissues with highly organized collagen fibres, the soft tissues with abundant elastic fibres, and bones, respectively. These values result in damping ratios up to 0.001, 0.012 and 0.188, respectively, for frequencies up to 2 kHz. Keefe et al. (1993) used a quality factor ( $Q = \frac{1}{2\zeta}$ ) of 2 as ‘typical of quality factors measured in mechanical impedance measurements on the human body’, corresponding to a damping ratio of 0.25. Assuming a damping ratio that is constant over the frequency range of interest, and excluding the outliers of the damping ranges mentioned above, in this study we used damping ratios of 0.1, 0.25 and 0.4. We used Rayleigh damping and calculate  $\alpha$  and  $\beta$  at each frequency in order to obtain the desired damping ratio.

### 4.2.3 Cochlear load

It has been reported that the cochlea influences the response of the ear mainly by damping, at least for the frequency range of interest here (e.g., Overstreet and Ruggero, 2002; Decraemer et al., 2007). Since our model does not contain the stapes, we applied a discrete dashpot (i.e., viscous damper) element to represent the damping effect, in the direction of stapedial piston-like motion, at the end of the long crus of the incus (i.e., where the incudostapedial joint would be). The viscous damping coefficient can be calculated by dividing the cochlear input impedance by the square of the footplate area of the stapes. Koike et al. (2002) calculated a coefficient of 0.89 Ns/m for their adult human model, for an impedance of 50 G $\Omega$ . For this impedance value, and a stapes footplate surface area of 2.3 – 3.75 mm<sup>2</sup> as reported by Wever and Lawrence (1954, p. 417) and Gan et al. (2011), we calculated a dashpot parameter of 0.2

– 0.7 Ns/m. We have not attempted to correct this for any possible differences between newborns and adults.

*Table 4–1 Material properties*

	Minimum	Baseline	Maximum
Young’s modulus (MPa)			
Pars tensa	2	6	10
Pars flaccida	0.4	1.2	2
Soft tissue around canal	0.02	0.21	0.4
Ossicles	4000	10000	16000
Ligaments	2	5	8
Poisson’s ratio			
Soft tissues (around canal and in middle ear)	0.485	0.49	0.495
Ossicles	0.3		
Density (kg/m <sup>3</sup> )			
Soft tissues	1000	1100	1200
Ossicles	1600	1800	2000
Damping ratio	0.1	0.25	0.4
Cochlear load			
Spring (N/m)	200	600	1000
Dashpot (N.s/m)	0.2	0.45	0.7
Stapes mass (kg)	$2 \times 10^{-6}$	$3 \times 10^{-6}$	$4 \times 10^{-6}$
Cavity volume (m <sup>3</sup> )	$700 \times 10^{-9}$	$850 \times 10^{-9}$	$1000 \times 10^{-9}$

#### **4.2.4 Air in middle-ear cavity**

The Eustachian tube connects the middle-ear cavity to the nasopharynx and can be in either an open or a closed state. When the tube is closed (its normal state) a volume of air is trapped in the middle-ear cavity and it has been shown to have a large impact on the input admittance of the middle ear (e.g., Funnell and Laszlo, 1982; Stepp and Voss, 2005). A few finite-element models take this effect into

account (e.g., Gan et al., 2004).

The compliance of the middle-ear cavity is calculated by

$$C_{\text{cav}} = \frac{V}{\rho c^2}, \quad (4-3)$$

where  $V$ ,  $\rho$  and  $c$  are the volume of the cavity and the density and sound speed of air, respectively. Qi et al. (2008) estimated this volume as being between 700 and 1000 mm<sup>3</sup> based on the same CT scan that we used in this study. Neglecting the mass of the air, the cavity effect was considered to be an ideal stiffness element. Thus, its admittance is purely susceptance and is calculated at each angular frequency  $\omega$  by

$$B_{\text{cav}} = \omega C_{\text{cav}}. \quad (4-4)$$

The middle-ear input admittance  $Y_{\text{me}}$  is calculated based on a series combination of the cavity and the TM admittance (e.g., Stepp and Voss, 2005):

$$\frac{1}{Y_{\text{me}}} = \frac{1}{Y_{\text{tm}}} + \frac{1}{Y_{\text{cav}}}. \quad (4-5)$$

#### 4.2.5 Air in ear canal

According to the geometry reconstructed from our CT images, the air enclosed inside the ear canal, between the probe tip and the TM, has a volume of 128 mm<sup>3</sup>. The corresponding compliance  $C_{\text{can}}$  and admittance  $Y_{\text{can}}$  were calculated in the same way as for the air in the middle-ear cavity, with the effects of mass again being neglected. The air in the canal is assumed to act as a lumped element in parallel with the ear-canal wall and the middle ear (e.g., Keefe et al., 1993, Fig. 12). The three admittances,  $Y_{\text{ec}}$  for the ear canal,  $Y_{\text{can}}$  for the canal air and  $Y_{\text{me}}$  for the middle ear, are in parallel, so the total admittance of the ear is

$$Y_{\text{ear}} = Y_{\text{ec}} + Y_{\text{can}} + Y_{\text{me}} . \quad (4-6)$$

#### 4.2.6 Boundary conditions

The canal and middle-ear were modelled separately and their individual contributions to the total immittance response of the ear were investigated. This was made possible by clamping the border of the TM, that being the only place where the two parts of the overall model interact. This assumption has been used in previous human middle-ear models (e.g., Rabbitt, 1988; Gea et al., 2010; Aernouts et al., 2012). In our middle-ear model, the ends of the AML and PIL were also clamped. In the ear-canal model, the surface of the probe tip was taken to be fixed, since it is assumed to be securely held in the canal, and so were the surfaces of the temporal bone and the TM.

#### 4.2.6 Loading conditions

In this study the sound pressures were applied as harmonic stimuli with an amplitude of 0.2 Pa root mean square (corresponding to 80 dB SPL) on the surfaces of the canal wall and the TM. For presentation, all displacements are normalized by the pressure. The frequency of the input pressure was varied between 25 and 2000 Hz in 25-Hz steps and the input admittance of the model was calculated for each frequency. The upper limit of 2000 Hz is set in order to maintain the validity of the assumption that the ear canal can be modelled as a lumped acoustical element (e.g., Shanks and Lilly, 1981; Margolis et al., 2003; Sanford and Feeney, 2008). For an average ear-canal length of 14 mm and a probe-tip insertion of 5 mm (Keefe et al., 1993), the effective length is 9 mm. This length is 19 times as long as the 171-mm wavelength of a 2000-Hz sound in air, so uniformity of the pressure on the surfaces is a valid assumption.

After the initial meshes were generated according to the procedure explained in Section 4.2.1, convergence tests were done to assess the adequacy of the mesh resolution for both the ear-canal and middle-ear models. Every element of each mesh was bisected three times. The admittance magnitudes

at the resonance peaks for the meshes after the third bisection deviated by only 1.2% and 0.9% from the results for the meshes after the second bisection for the ear-canal and middle-ear models, respectively. Thus, we used the mesh resulting from the second mesh bisection for all simulations reported below. The ear-canal mesh consisted of 45 086 second-order tetrahedral elements (17 544 and 27 542 elements for the ear-canal volume and the surrounding soft tissues, respectively). The middle-ear mesh consisted of 28 748 second-order tetrahedral elements (23 012, 6 136 and 288 elements for the TM, ossicles and ligaments, respectively).

## **4.2.8 Computational methods**

### *4.2.8.1 Finite-element solver*

The finite-element solver was Code\_Aster (<http://www.code-aster.org>) version 11.5, which is free (libre) and open-source software. Simulations were performed on the supercomputer Guillimin of McGill University. Guillimin is a part of the Compute Canada national High Performance Computing (HPC) platform. It is a cluster of Intel Westmere EP Xeon X5650 and Intel Sandy Bridge EP E5-2670 processors running under the CentOS 6 Linux distribution. We ran a maximum of 12 simulation scenarios at a time on nodes of 12 or 16 processors, each scenario on a single processor. Typical run times for the ear-canal and middle-ear models were 144 and 277 minutes, respectively.

The complex dynamic responses of the models were obtained using the dynamic linear harmonic (DYNA\_LINE\_HARM) module in Code\_Aster. This module calculates the steady-state response of the models to the harmonic excitation.

### *4.2.8.2 Admittance calculation*

The volume displacements of the ear-canal and middle-ear models were calculated from the variation of the volume of a very-low-impedance mesh filling the canal, with a Young's modulus of 0.001 Pa, a density of 0.001 kg/m<sup>3</sup> and a Poisson's ratio of 0.01. We performed a series of sensitivity analyses to

confirm that the effects of this pseudomaterial on the model responses were negligible. Code\_Aster calculated the real and imaginary volume displacements of the enclosed volume and these values were multiplied by the angular frequency  $\omega$  to calculate volume velocities, which were then divided by the sound pressure to calculate the conductance  $G$  and susceptance  $B$ . The admittance magnitude and phase were calculated as  $\sqrt{G^2+B^2}$  and  $\text{Tan}^{-1}(B/G)$ , respectively.

#### 4.2.9 Sensitivity analysis

A sensitivity analysis can lead to an improved understanding of the system and help establish how much the uncertainty in the parameters will affect the output. In this study, we performed two sensitivity analyses, using (1) a traditional one-parameter-at-a-time method, and (2) the method of Morris (1991). Two different criteria were used to evaluate the effects of each parameter on both the ear-canal and middle-ear models: (1) the maximum admittance, and (2) the frequency at which that maximum admittance occurs. The range between the minimum and maximum values for each parameter (shown in Table 1) was divided into 4 intervals so each parameter has  $p = 5$  evenly spaced values.

In the one-parameter-at-a-time method, the effect of each parameter is studied individually by varying it while keeping all of the other parameters at their baseline values. This method provides a quantitative measure of the effect of each individual parameter on the output. Performing a linear regression analysis provides measures of the size of the effect, given by the slope, and of the linearity or nonlinearity of the effect, given by the coefficient of determination  $R^2$ :

$$R^2 = 1 - \frac{\sum_{i=1}^m (y_i - g_i)^2}{\sum_{i=1}^m (y_i - \bar{y})^2} \quad (4-7)$$

where  $y_i$  ( $i = 1, 2, \dots, p$ ) are the outputs at each of  $p$  simulations  $\bar{y}$ , is the mean of the outputs and the  $g_i$  are the values in the fitted line corresponding to the  $y_i$ .  $R^2$  is a number between 0 and 1, and the larger it is, the more linear the parameter effect is.

The method of Morris (1991), on the other hand, is said to be a ‘qualitative’ screening method. The underlying intent of this method is to determine which input parameters may be considered to have effects that are (a) negligible, (b) linear and additive, or (c) nonlinear and/or involved in interaction with other parameters. A number of combinations of different parameter values is randomly selected within the domain of all possible combinations. Unlike the one-parameter-at-a-time method, in which all other parameters are at their baseline values when a particular parameter is altered, in this method every other parameter can have any value in its own specified range when the effect of a particular parameter is investigated. Assume that, for the model being studied, an output  $y$  is given by

$$\begin{aligned} y &= f(\mathbf{x}) \\ \mathbf{x} &= \mathbf{x}(x_1, x_2, \dots, x_i, \dots, x_k), \end{aligned} \quad (4-8)$$

where  $x_1, x_2, x_3, \dots, x_i, \dots, x_k$  are the parameters of the model. For this model, simulations are designed for  $n$  sets  $\mathbf{x}^j$  ( $j = 1, 2, 3, \dots, n$ ). Each parameter  $x_i$  can take on  $p$  predefined values in the range  $[x_{i, \min}, x_{i, \max}]$ . At each  $\mathbf{x}^{j+1}$ , only the value of one parameter  $x_i$  is changed from  $\mathbf{x}^j$ . Thus, for two consecutive simulations we can define a simple partial difference of the output with respect to the change of  $x_i$  to  $x'_i$ :

$$d_i(\mathbf{x}^j) = \frac{f(\mathbf{x}^{j+1}) - f(\mathbf{x}^j)}{\Delta} = \frac{f(\mathbf{x}(x_1, x_2, x_3, \dots, x'_i, \dots, x_k)) - f(\mathbf{x}(x_1, x_2, x_3, \dots, x_i, \dots, x_k))}{\Delta}. \quad (4-9)$$

where  $\Delta$  is a value in  $\{1/(p-1), \dots, 1-1/(p-1)\}$ . (In our case, for  $p = 5$ ,  $\Delta$  could be 1/4, 1/2 or 3/4.) Since from one simulation to the next only one parameter changes,  $k+1$  simulations should be performed to obtain one  $d_i$  for each parameter, resulting in a total of  $n = r \times (k+1)$  simulations,  $r$  being

the number of  $d_i$ 's desired for each parameter.

Unlike the case of the one-parameter-at-a-time method, it is not necessary to keep all but one parameter at their baseline values; the only restriction is that only one  $x_i$  changes between  $\mathbf{x}^j$  and  $\mathbf{x}^{j+1}$ . Morris (1991) introduced a method, which is used here, to randomly design each set of  $k+1$  of simulations. We selected  $\Delta = 1/(p-1)$  to cover all  $p$  options for the parameter ranges.

Once  $n$  simulations are performed, then the effect of parameter  $x_i$  can be described using the following three measures:

$$\begin{aligned}\mu_i &= \frac{1}{r} \sum_{j=1}^r d_i(\mathbf{x}^j) \\ \mu_i^* &= \frac{1}{r} \sum_{j=1}^r |d_i(\mathbf{x}^j)| \\ \sigma_i &= \sqrt{\frac{1}{r-1} \sum_{j=1}^r (d_i(\mathbf{x}^j) - \mu_i)^2}\end{aligned} \quad (4-10)$$

For each parameter  $x_i$ , the corresponding  $\mu_i$  is the mean of the  $d_i$ 's across the  $r$  simulations and is thus a measure of the overall influence of that parameter on the output.  $\mu_i^*$  provides a more practical measure of overall influence of a parameter, in which oppositely signed values of the  $d_i$  do not cancel each other.  $\sigma_i$  is the standard deviation of the  $d_i$ 's for parameter  $x_i$  and is a measure of the interaction and nonlinear effects of  $x_i$ . If for parameter  $x_i$  we obtain a high value of  $\sigma_i$  (i.e., large deviations of  $d_i$  around its mean value), it means that the output is affected by the choice of the other parameters (i.e., there are parameter interactions), or that the parameter has a nonlinear effect in the range of  $[x_{i, \min}, x_{i, \max}]$ , or both. In contrast, a low  $\sigma_i$  indicates that  $x_i$  has linear effects that are independent (or nearly so) of the values taken by the other parameters.

We set  $r = 10$  as a trade-off between completeness and computation time. For the ear-canal model, 4 parameters were investigated (i.e.,  $k = 4$ ): Young's modulus, density, Poisson's ratio and damping ratio of the soft tissue. This resulted in 50 simulations for the ear-canal model. For the middle-ear model, 12

parameters were investigated (i.e.,  $k = 12$ ): Young's moduli of the pars tensa, pars flaccida ligaments and ossicles; densities of the soft tissue and ossicles; middle-ear cavity volume; Poisson's ratio of the soft tissues; stapes mass; stiffness of the stapedial annular ligament; cochlear load (dashpot coefficient); and damping ratio. (The Poisson's ratio of the ossicles was not varied.) This resulted in 130 simulations for the middle-ear model. Instead of just presenting the values for the  $\sigma_i$ 's, as done by Morris (1991), we present scatter plots and 10th-to-90th-percentile ranges of the  $d_i$ 's for each parameter.

#### **4.2.10 Clinical data**

Three studies of immittance response have been reported in the literature for ages similar to the 22-day age of our model. Holte et al. (1990) reported pressurized admittance responses for infants in 5 age groups: 1–7, 11–22, 26–47, 51–66 and 103–133 days old. Their measurements were done from 250 to 1000 Hz. Keefe et al. (1993) reported impedance measurements performed under ambient pressure for age groups of 1, 3, 6, 12 and 24 months in addition to adults, for frequencies from 125 to 10700 Hz with a 1/3-octave resolution. The maturation effects were studied further by Keefe and Levi (1996) with the data from the 1993 study expressed in terms of admittance. Sanford and Feeney (2008) measured pressurized admittance for infants at 1, 3 and 6 months and for adults, for frequencies from 250 to 8000 Hz with a 1/3-octave resolution. Since our model represents unpressurized conditions, we used only the data of Keefe et al. (1993) for comparison with our model, to avoid the complications inherent in interpreting zero-pressure or peak-pressure data from pressure sweeps like those of Holte et al. (1990) and Sanford and Feeney (2008).

In addition, we used admittance measurements that we performed as part of another project, on a group of 23 infants with ages between 14 and 28-days old, for frequencies from 250 to 8000 Hz at 1/12-octave resolution. That study was approved by the Institutional Review Board of the McGill University Health Centre. The measurements were made with a wideband tympanometry research

system (WBTymp 3.2, Interacoustics Inc.). All measurements except one were performed in the Otolaryngology out-patient clinic of the Montréal Children's Hospital. More details about the measurement procedure can be found in Pitaro (2013).

## **4.3 Results**

### **4.3.1 Displacement patterns**

Normalized displacement maps of the ear-canal and middle-ear models at a low frequency (100 Hz) are presented in Fig. 4–3 for the baseline parameter values. (In the figure, the ear-canal model is sectioned in a horizontal plane to provide a superior-to-inferior direction of view of the temporal bone and ear canal.) For the ear canal, the greatest displacements occur at the medial and inferior portion of the canal, just inferior to the TM. This can be explained by the fact that the ear canal has a larger diameter in that location. For the TM, the maximum displacement occurs in the posterior region (where the TM is thinner and the distance from the manubrium to the TM boundary is greater) and a smaller local maximum occurs in the anterior region.

Vibration patterns of the ear-canal wall are presented in Fig. 4–4 for frequencies of 250, 500, 1000, 1500 and 2000 Hz. Since the main displacements occur in the inferior portion of the canal at all frequencies, the canal model is again sectioned horizontally and the viewing direction is again superior to inferior. The initial vibration pattern (i.e., one maximal displacement region in the inferior medial portion of the canal) remains up to frequencies of  $\sim 700$  Hz, in the vicinity of the ear-canal resonance. The magnitude of the maximum displacement increases with frequency from 24 to 32 nm/Pa. In the frequency range of 700 to 1200 Hz, the region of maximal displacement moves toward the lateral portion of the canal and the magnitude of the maximum displacement decreases to 12 nm/Pa. At frequencies from  $\sim 1200$  Hz up to  $\sim 1500$  Hz, two regions of maximal displacement are visible in the lateral and medial portions of the ear canal and the magnitude of the maximum displacement decreases

from 12 to 9 nm/Pa. At frequencies higher than 1500 Hz, up to our upper limit of 2000 Hz, the region of maximal displacement in the medial portion splits into two regions and the magnitude of the maximum displacement decreases from 9 to 6 nm/Pa.

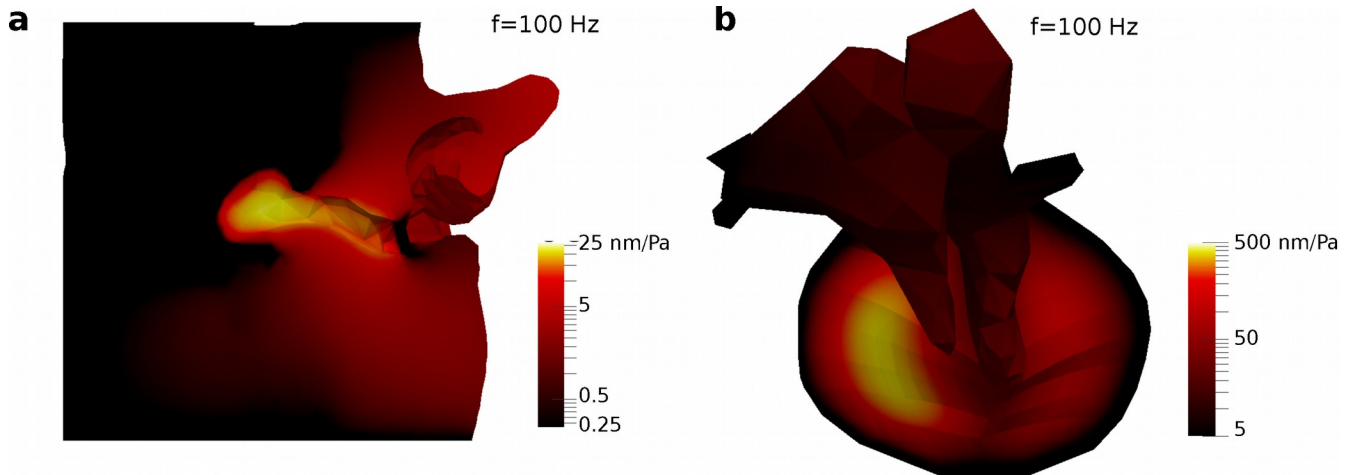


*Fig. 4–3. Normalized displacement maps of the models in response to sound pressures at a low frequency (100 Hz). Due to the small displacements of some components of the models (e.g., ossicles), the displacement maps are presented using logarithmic scales. (a) Ear-canal model, sectioned in a horizontal plane to provide a superior-to-inferior view of the temporal bone and ear canal; the largest displacements are in the medial region of the canal. (b) Medial view of the middle-ear model; the largest displacements are in the posterior portion of the tympanic membrane.*

Vibration patterns of the TM are presented in Fig. 4–5, again for frequencies of 250, 500, 1000, 1500 and 2000 Hz. The initial vibration pattern (i.e., two maxima, in the posterior and anterior regions of the TM) remains up to about 1800 Hz and the maximal displacement is in the posterior region. The maximum displacement of the anterior region increases gradually from 180 nm/Pa at 250 Hz to 350 nm/Pa at 1800 Hz then drops to 330 nm/Pa at 2000 Hz. The magnitude of the maximum displacement in the posterior region increases from 390 nm/Pa at 250 Hz to 830 nm/Pa at 1200 Hz. Between 1200 and 1800 Hz, the posterior maximal-displacement region moves toward the superior quadrant. Above 1800 Hz, the posterior maximum splits into superior and inferior regions and the magnitude of the maximum displacement decreases to 370 nm/Pa.

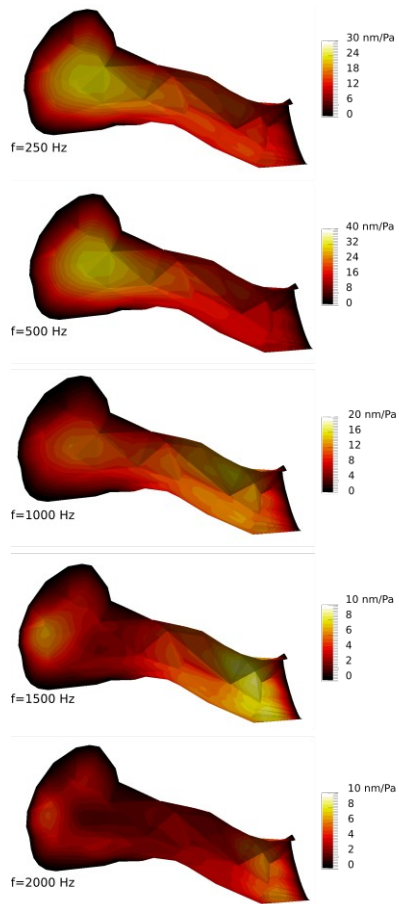


*Fig. 4–4. Normalized displacement maps of vibration patterns of the ear-canal wall at five different frequencies. Superior view of horizontally sectioned canal, as in Fig. 4–3a.*

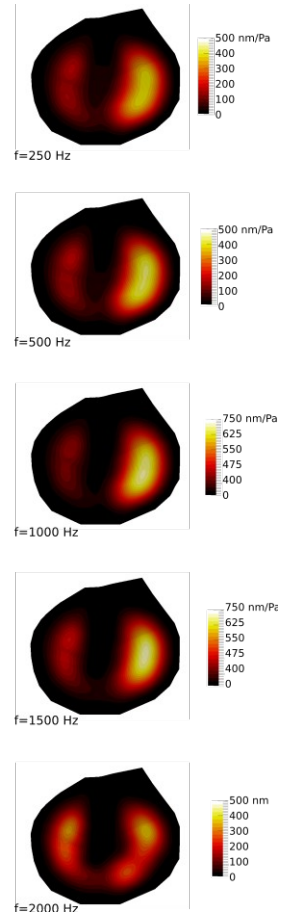


*Fig. 4–5. Normalized displacement maps of vibration patterns of the middle ear at different frequencies.*

### 4.3.2 Admittances of the individual models

The volume velocities and admittances of the ear-canal and middle-ear models were calculated as described in Section 4.2.8.2. The input-admittance magnitude and phase of the ear canal as functions of frequency for three scenarios (i.e., the low-impedance, baseline and high-impedance models) are presented in Fig. 4–6. Since the baseline model is more than 10 times as stiff as the low-impedance model, three intermediate cases, with Young’s moduli of 40, 80 and 160 kPa for the soft tissue and baseline values for the other material parameters, are also presented in this figure to illustrate the

gradual change of the responses. As the model becomes stiffer, the resonance peaks shift to higher frequencies, decrease in magnitude, and become broader: the admittance magnitude peaks of 24.2, 5.6 and 3.2 mm<sup>3</sup>/s/Pa occur at 225, 700 and 1050 Hz, and the widths of the peaks (as defined by the frequencies at which the magnitudes are 90% of the peak value) are 150, 500 and 850 Hz for the low-impedance, baseline and high-impedance models, respectively. The phases are constant at the lowest frequencies, as expected for a stiffness-dominated response. However, since the Rayleigh damping was set so as to provide a constant damping ratio, even at low frequencies, the phase does not converge to 90°. As the excitation frequency is increased, the mass contributes more to the response and the phases tend toward negative angles.

The admittance of the enclosed air in the canal was calculated by Equations 4–3 and 4–4 and is presented in Fig. 4–6a. It is a linear function of the excitation frequency and thus appears as an increasingly steep curve for the logarithmic frequency scale of the figure. Since the canal air is modelled as a pure stiffness component, its phase is constant at 90°.

The admittance magnitude and phase of the middle-ear model for three scenarios (i.e., the low-impedance, baseline and high-impedance models) are presented in Fig. 4–7. As the model becomes stiffer, the resonance peaks shift to higher frequencies, decrease in magnitude, and become broader, similar to what we see for the ear-canal model. The admittance magnitude peaks of 104.6, 39.1 and 21.8 mm<sup>3</sup>/s/Pa occur at 1400, 2000 and 2300 Hz, and the widths of the peaks (again defined by the frequencies at which the magnitudes are 90% of the peak value) are 200, 900 and 1200 Hz for the low-impedance, baseline and high-impedance models, respectively. We extended the frequency range to 3000 Hz to provide an estimate of the resonance frequency of the middle ear. The parts above 2000 Hz are represented by dashed lines to emphasize that they may be beyond the range of validity of the uniform-pressure assumption. In the same way as for the canal model, the phases are constant at the

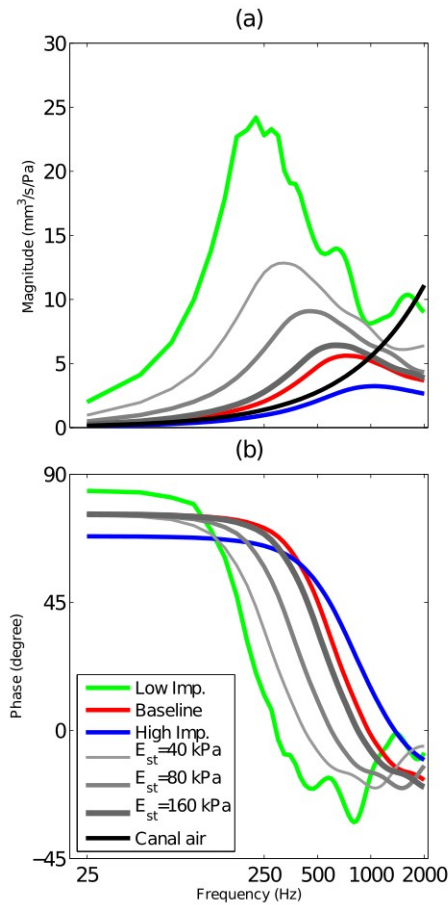


Fig. 4–6. Admittance responses of the ear-canal models. Admittance magnitudes (a) and phases (b) are presented for low-impedance (green), baseline (red), and high-impedance (blue) parameters, and for three intermediate cases (Young’s moduli of 40, 80 and 160 kPa for the canal soft tissue). The admittance magnitude for the air in the canal is presented in (a) as a solid black line; its phase is constant at  $90^\circ$  over the frequency range.

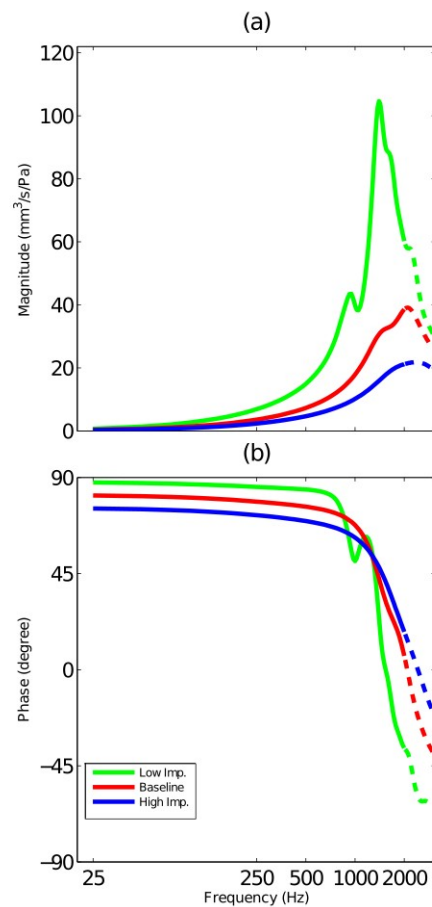


Fig. 4–7. Admittance responses of the middle-ear models. Admittance magnitudes (a) and phases (b) are presented for low-impedance (green), baseline (red) and high-impedance (blue) parameters.

lowest frequencies but do not quite reach  $90^\circ$ . In the middle-ear model the phase responses remain close to  $90^\circ$  over a larger range of frequencies than in the ear-canal model, illustrating that the stiffness characteristics are relatively more important in the case of the middle ear.

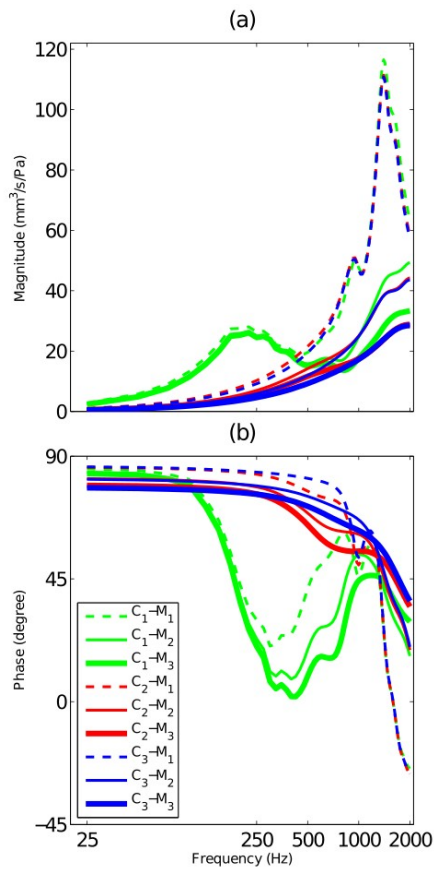


Fig. 4–8. Admittance responses of the combinations of three ear-canal and three middle-ear models. Admittance magnitudes (a) and phases (b) are presented for each pair  $C_i-M_j$  corresponding to the combination of the canal model  $i$  and the middle-ear model  $j$ ; the indices  $i = 1, 2$  and  $3$  represent the low-impedance, baseline and high-impedance models, respectively.

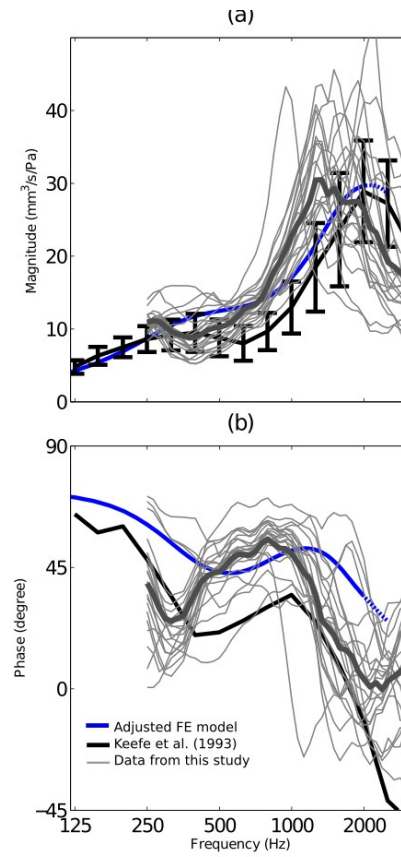


Fig. 4–9. Results for model with adjusted parameters and comparison with two sets of clinical data. Admittance magnitudes (a) and phases (b) are presented for the data of (Keefe 1993) and for data from this study, in comparison with the output of the model with adjusted parameters (see text).

### 4.3.3 Admittance of the combined model

Based on the admittance responses of its components as shown in Figs. 4–6 and 4–7, the combined input admittance response of the ear was calculated using Equation 4–6. All nine combinations of the three ear-canal scenarios and the three middle-ear scenarios are presented in Fig. 4–8. In this figure

each pair  $C_i-M_j$  corresponds to the combination of the canal model  $i$  and the middle-ear model  $j$ , and the indices  $i = 1, 2$  and  $3$  represent the low-impedance, baseline and high-impedance models, respectively.

In all results with the low-impedance canal model (green curves), a local peak in the frequency range of 150–500 Hz is observed, along with a drop and subsequent rise of the phase response at frequencies below 1000 Hz. The main resonance magnitudes and frequencies are slightly higher than in the corresponding middle-ear responses (Fig. 4–7a), indicating that the low-impedance canal influences the total response not only at low frequencies but also, to a small extent, at higher frequencies.

As canal becomes stiffer (red and blue curves), the local admittance peak at low frequencies disappears. Since the resonances of the baseline and high-impedance canal models are at frequencies higher than 500 Hz (Fig. 4–6a), their resonances merge into the resonance of the middle ear. Also, the phase responses remain close to  $90^\circ$  over a broader frequency range (Fig. 4–8b), representing the influence of the stiffness characteristics of the middle ear on the total ear response. In these models the resonance magnitudes and frequencies are close to the those of the middle-ear response (as shown in Fig. 4–7b), indicating that at higher frequencies the middle-ear response is dominant.

#### **4.3.4 Model validation and parameter adjustments**

The canal response has a pronounced effect on the total admittance of the ear at frequencies below 1000 Hz while the middle-ear response dominates at higher frequencies. Comparing the clinical data with the nine combinations of the canal and middle-ear models (not shown), it can be concluded that an intermediate-impedance canal model, combined with the high-impedance middle-ear model, can provide a reasonable match to the clinical data over the frequency range of interest: by assigning a high damping ratio of  $\zeta = 0.4$  and an intermediate stiffness of  $E = 80$  kPa to the soft tissue surrounding the ear canal, we can adjust the admittance magnitude of the canal resonance and shift it to frequencies

around 500 Hz, to be more consistent with Keefe and Levi (1996, Fig. 2). Fig. 4–9 shows the admittance for such an adjusted model of the ear, together with the two sets of clinical data, namely, the means of Keefe and Levi (1996) and the curves for our individual subjects. We extended the frequency range up to 2500 Hz (again with dashed lines) to provide insight into the admittance behaviour around the resonance peak at 2000 Hz.

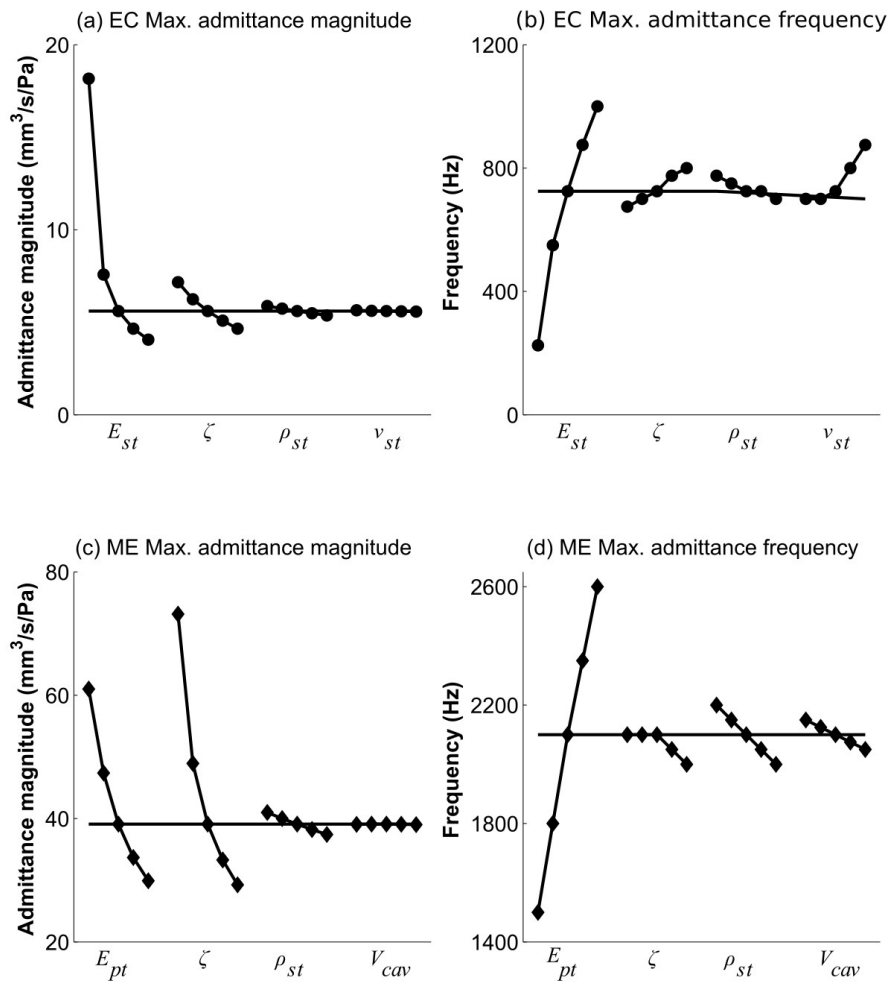


Fig. 4–10. One-variable-at-a-time sensitivity analysis, showing the influence of the material parameters on the maximum admittance magnitudes (panels a & c) and the corresponding frequencies (panels b & d) for the ear-canal model (panels a & b) and the middle-ear model (panels c & d).  $E_{st}$  = Young's modulus of the soft tissue;  $\zeta$  = damping ratio;  $\rho_{st}$  = density of soft tissue;  $\nu_{st}$  = Poisson's ratio;  $E_{pt}$  = Young's modulus of the pars tensa;  $V_{cav}$  = volume of the middle-ear cavity.

The admittance magnitude response of the adjusted model is mostly within the error bars of the clinical data of Keefe and Levi (1996), with values up to 30% higher at frequencies between 500 and 1000 Hz (Fig. 4–9a). The model results are entirely within the range of the individual responses of our clinical data, where the resonance peaks of the admittances are in the range of 1000 to 2200 Hz and the peak values vary between 24 and 50 mm<sup>3</sup>/s/Pa; the admittance peak of the adjusted model (30 mm<sup>3</sup>/s/Pa at 2100 Hz) falls within this range.

The mean phase data of Keefe and Levi (1996) show a minimum at 400 Hz, rise to a maximum at 1000 Hz and then drop at higher frequencies; in our clinical data the minima and maxima are mostly at lower frequencies and they are sharper because the frequency resolution is finer than that of Keefe et al. and because they have not been smeared by averaging. The shape of the model curve is similar to that of the mean curve of Keefe et al. but the minima and maxima are shifted to slightly higher frequencies and the phases are about 15 to 28° higher than those of Keefe et al., more like those of our clinical data.

#### 4.3.6 Sensitivity analysis

The results of the one-parameter-at-a-time sensitivity analysis are presented in Fig. 4–10, for the two separate models (ear canal in the upper panels, middle ear in the lower panels) and for two features of the admittance (maximum magnitude in the left-hand panels and frequency of the maximum in the right-hand panels). All four parameters are shown for the canal model, and for the middle-ear model only the four most influential parameters are shown.

The parameters with the most influence on the maximum admittance magnitude of the ear-canal model are the Young’s modulus  $E_{st}$ , damping ratio  $\zeta$ , density  $\rho_{st}$  and Poisson’s ratio  $\nu$  of the soft tissue, in decreasing order of importance (Fig. 4–10a). The coefficients of determination  $R^2$  for these parameters are 0.71, 0.95, 0.99 and 0.99, respectively, meaning that the  $E_{st}$  has a quite nonlinear effect but that the others are practically linear. The same order of influence holds for the frequency of the

maximum admittance, except that Poisson’s ratio plays an important role at its higher values (Fig. 4–10b). The  $R^2$ ’s for this criterion are 0.96, 0.99, 0.94 and 0.87 for  $E_{st}$ ,  $\zeta$ ,  $\rho_{st}$  and  $\nu$ , respectively, meaning that  $\nu$  has a more nonlinear effect than the others do.

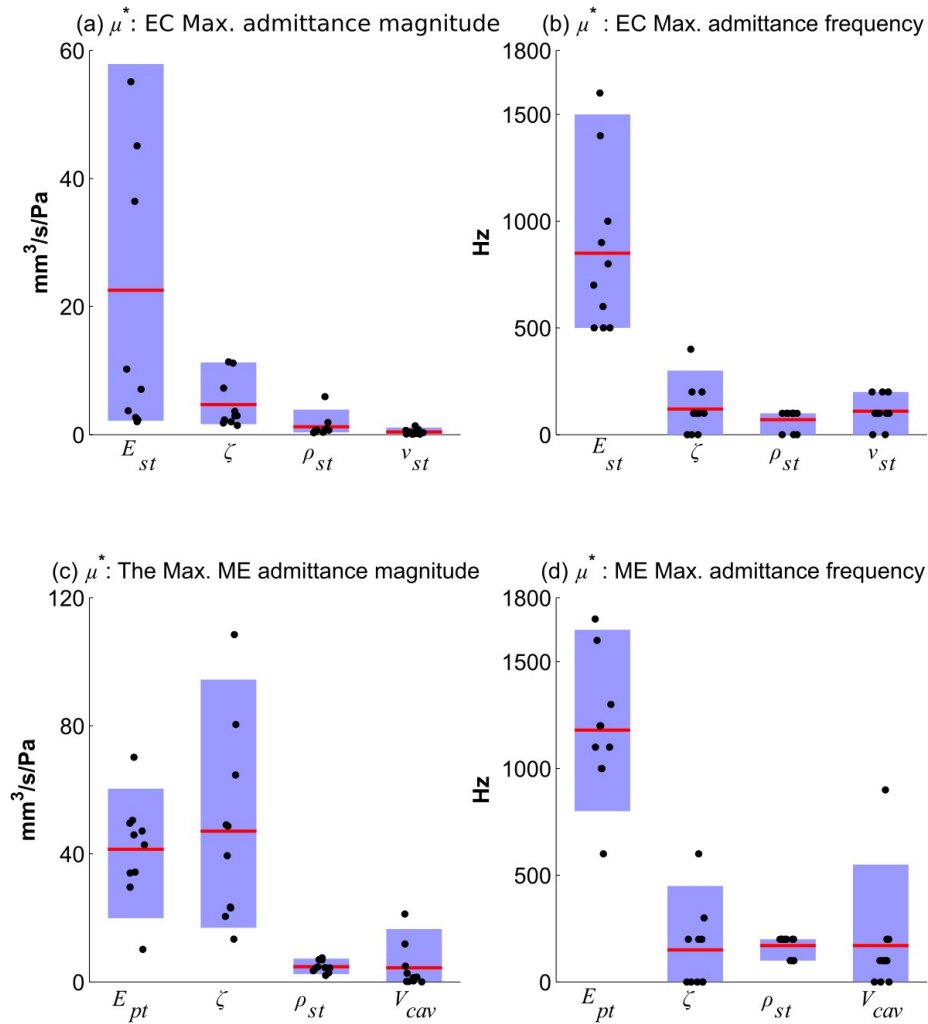


Fig. 4–11. Sensitivity analysis using Morris method, showing the influence of the material parameters on the maximum admittance magnitudes (panels a & c) and the corresponding frequencies (panels b & d) for the ear-canal model (panels a & b) and the middle-ear model (panels c & d). The blue boxes indicate the 10th-to-90th-percentile ranges; each point represents a  $|d_i|$  and the red lines represent  $\mu_i^*$ . Abbreviations are the same as in Fig. 4–10.

For the middle-ear model, the damping ratio  $\zeta$  affects the maximum admittance magnitudes more than does the pars-tensa Young’s modulus  $E_{pt}$ . The soft-tissue density  $\rho_{st}$  (i.e., the density of the components other than the ossicles) and the middle-ear cavity volume  $V_{cav}$  have much smaller effects

(Fig. 4–10c). The  $R^2$ 's for  $E_{pt}$ ,  $\zeta$ ,  $\rho_{st}$  and  $V_{cav}$  are 0.94, 0.92, 0.99 and 0.98, respectively, reflecting the fact that  $E_{pt}$  and  $\zeta$  have somewhat nonlinear effects. The frequency of the maximum admittance is strongly affected by  $E_{pt}$  and the order of the influence of the other parameters for this criterion is  $\rho_{st}$ ,  $V_{cav}$  and  $\zeta$  (Fig. 4–10d). The  $R^2$ 's for  $E_{pt}$ ,  $\zeta$ ,  $\rho_{st}$  and  $V_{cav}$  are 0.98, 0.75, 0.98 and 0.97, respectively, indicating that  $\zeta$  is the only one with a notably nonlinear effect. The effects of the other parameters of the middle-ear model are less than 1% and they are not presented in this figure.

The results of the sensitivity analysis with the Morris method are presented in Fig. 4–11, again for the maximum admittance and its corresponding frequency. Although, as mentioned in Section 4.2.9, the effects of 12 parameters of the middle-ear model were explored with the Morris method, only the four most important parameters are shown here. Each point represents a  $|d_i|$ , and the red lines represent  $\mu_i^*$ . The blue boxes indicate the 10th-to-90th-percentile ranges. The order of overall influence of the ear-canal parameters (i.e.,  $\mu_i^*$ ) on the maximum admittance and its corresponding frequency (Fig. 4–11a & b) is the same as what the one-parameter-at-a-time analysis shows (Fig. 4–10a & b). The large 10th-to-90th-percentile ranges for the Young's modulus  $E_{st}$  indicate possible nonlinear and/or interaction effects for both the admittance magnitude and the corresponding frequency.

The order of overall influence of the middle-ear parameters (i.e.,  $\mu_i^*$ ) on the maximum admittance magnitude (Fig. 4–11c) is again the same as what the one-parameter-at-a-time analysis shows (Fig. 4–10c). However, the order of importance is slightly different for the corresponding frequency: as shown in Fig. 4–10d, the mean sizes of the effects are similar for the damping ratio  $\zeta$ , soft-tissue density  $\rho_{st}$  and middle-ear cavity volume  $V_{cav}$ , but the distributions around the means are different. For the cavity-volume effect, which is linear in Fig. 4–10c, the wide (and asymmetrical) distribution of the deviations may be due to interactions with other parameters.

In both ear-canal and middle-ear models, the effects of the damping ratio are more complicated. Its broad distribution of  $d_i$ 's in Fig. 4–11d may be because of the strong nonlinearity seen in Fig. 4–10d,

and that nonlinearity may be because multiple peaks at low damping ratios (Figs. 4–6 & 7, blue curves) are merged when the damping is higher. In addition, based on the definition of the Rayleigh model of damping, by which the damping is a product of stiffness and mass, these three parameters can be expected to interact with one another.

## **4.4 Discussion**

### **4.4.1 Displacement patterns**

To the best of our knowledge, no experimental data have been reported for vibration and displacement patterns of the newborn TM. However, there have been a few studies of the vibration patterns of the TM in adult humans and animals. Tonndorf and Khanna (1972) and Rosowski et al. (2009) reported that complex vibration patterns of the adult human TM are observable at frequencies higher than 3000 and 4000 Hz, respectively. Our model shows that the first, simple vibration pattern (i.e., two maxima, one posteriorly and one anteriorly) remains only up to about 1800 Hz. Around this frequency, the patterns start to become more complex, as described in Section 4.3.1. The fact that the complex patterns begin at a lower frequency may be attributed to the lower stiffness of the TM in the newborn model.

Unlike the case for the TM, the vibration patterns of the ear canal cannot be readily observed in experimental measurements and no experimental data have been reported in the literature for either newborns or adults. As shown in Section 4.3.1, our model predicts three major displacement patterns of the canal: a single maximal-displacement region in the inferior medial region at low frequencies; a single maximal-displacement region in the lateral region at intermediate frequencies; and two maximal-displacement regions, in the lateral and medial regions, at high frequencies.

### **4.4.2 Admittance**

Holte et al. (1991) and Keefe et al. (1993) found that an admittance maximum of the ear canal in

infants less than 1 month old happens at frequencies around 450 Hz. With our adjusted parameters (Section 4.3.4) the resonance happens around 500 Hz in the model, similar to what was found by Holte et al. and Keefe et al. The canal resonances of the individual subjects in our clinical measurements occur in the range of 250 to 500 Hz, mostly close to 250 Hz.

Holte et al. (1991) didn't measure to high enough frequencies to observe the middle-ear resonance, but they suggested that it is beyond 900 Hz. Keefe et al. (1993) reported that the overall ear resonance was in the vicinity of 1800 Hz. This resonance presumably contains both canal and middle-ear responses, with the resonance of the middle ear itself happening at a frequency slightly higher than 1800 Hz. The ear resonances of the individual subjects in our clinical measurements are in the range of 1000 to 2500 Hz. In our models, the middle-ear resonances happen around 1400, 2000 and 2300 Hz for the low-impedance, baseline and high-impedance models (Fig. 4–7a), which is consistent with the measured data.

As the frequency increases from 25 to 1000 Hz, the ratio of the admittance magnitude of the canal to that of the middle-ear decreases from 0.6 to 0.3 for our baseline models. This ratio is larger (decreasing from 2.0 to 0.6 over the same frequency range) in the adjusted model. Thus, at frequencies below 1000 Hz admittance measurements are highly affected by the canal response and they cannot satisfy their main goal of reporting the middle-ear response. The response of the ear canal becomes negligible at frequencies in the vicinity of the middle-ear resonance (i.e., between 1000 and 2000 Hz). This suggests that admittance measurements can provide more information about the condition of the middle-ear when made at frequencies above 1000 Hz than when made at lower frequencies. However, since the resonance frequency may vary considerably due to intersubject variability (as seen in the individual responses in Fig. 4–9), it may be important to measure at many frequencies over the range where the resonance may occur.

When comparing the model output with clinical data, one should keep several factors in mind. (1) Our model is reconstructed from one particular ear, whereas the clinical data of Keefe et al (1993), for example, are averaged over groups of infants with substantial inter-subject variability. Averaging across a group may cancel out fine features of the response. For example, if different subjects have different resonance frequencies (as seen in the individual curves in Fig. 4–9), the average will display a flatter, smeared resonance, making it hard to compare the amplitude maximum and hard to draw conclusions about the resonance frequency. (2) There are substantial differences between our measurements and those of Keefe et al. (1993), which may be attributed to factors besides inter-subject variability, such as differences in the measurement devices, different screening of the subjects before inclusion in the study, etc. (3) During the first months after birth, the ear response is highly age dependent (e.g., Holt et al. 1991; Keefe et al. 1993), particularly for the first month of age. Hunter et al. (2010, Fig. 7) reported that within ~100 hours after birth the reflectance response of the ear alters by more than 50 % at 2000 Hz. Our model is for a 22-day-old baby, while the data of Keefe et al. are for somewhat older babies, around 1 month old. A more compliant canal and TM in younger infants may increase the admittance magnitudes and shift the resonance to lower frequencies. (4) Biological tissue can be expected to have frequency-dependent behaviour (e.g., Charlebois et al., 2013; Motallebzadeh et al., 2013a), but in these models all material properties are assumed to be constant across frequencies. Such potential frequency dependence should be taken into account when such models are refined.

#### **4.4.3 Sensitivity analysis**

As stated in Section 4.2.2.1.3, the material properties of the ear undergo significant alterations with age, particularly in the first months of life, and their values are even less well known than for adults. We performed two sets of analyses to investigate the sensitivity of the model outputs (in particular, the maximum admittance values and corresponding frequencies) to the parameters.

The Morris method enables us to investigate nonlinearity of the effects of parameters, and interactions among them, as well as the overall importance of their effects on the output. Morris (1991) stated that ‘where important nonlinearity or interaction exists, an experiment of any design that is small relative to the number of inputs will generally not produce enough information to resolve the nature of these effects’. However, combined with information about the nonlinearities that we obtain from the one-parameter-at-a-time sensitivity analysis, the Morris method can provide preliminary suggestions about the nature of these effects, at least for some parameters.

The results of the sensitivity analysis provide information about the relative importance of different material parameters, and which ones should be focused on to obtain more accurate values. In addition, the results provide insight into the sensitivity of the admittance data to possible pathologies or abnormal anatomical variations. For instance, a pathological condition that alters the stiffness and mass of the TM will result in significant changes in the admittance magnitude and resonance frequency. On the other hand, admittance data cannot provide accurate information about parameters or components that do not influence the admittance response significantly, such as the density of the ossicles.

## **4.5 Acknowledgements**

This work was supported in part by the Canadian Institutes of Health Research, the Fonds de recherche en santé du Québec, the Natural Sciences and Engineering Research Council (Canada), the Montréal Children’s Hospital Research Institute, and the McGill University Health Centre Research Institute. Computations were made on the supercomputer Guillimin of McGill University, managed by Calcul Québec and Compute Canada; the operation of this supercomputer is funded by the Canada Foundation for Innovation, NanoQuébec, the Réseau de Médecine Génétique Appliquée and the Fonds de recherche du Québec – Nature et technologies. The authors thank C. Northrop (Temporal Bone Foundation, Boston) for the histological images used to supplement our CT scan.

# **Chapter 5: Fluid-structure finite-element modelling of the wideband acoustic input admittance of the newborn ear canal and middle ear**

To be submitted to the *Journal of the Association for Research in Otolaryngology*.

## **Preface**

In the previous chapter, it was assumed that the wavelength of the sound at frequencies below 2 kHz is long enough (in comparison with model dimensions) that we could assume a uniform pressure distribution throughout the ear canal and middle-ear cavity and across the TM surface. We have taken fluid-structure interactions into account and developed a finite-element model to investigate the wideband immittance responses of the ear canal and middle ear in newborns and extended the frequency range up to 10 kHz. The modelling provides insight into the mechanical behaviour of the newborn ear and predicts features of the admittance responses that have not been observed in clinical data, presumably because of the low frequency resolution of the measurements.

## **Abstract**

The anatomical differences between the newborn ear and the adult one result in different input-admittance responses in newborns than in adults. Taking into account fluid-structure interactions, we have developed a finite-element model to investigate the wideband admittance responses of the ear canal and middle ear in newborns for frequencies up to 10 kHz. Sensitivity analyses were performed to investigate the contributions of the ear canal and middle ear to the overall admittance responses, as well as the effects of the material parameters, measurement location and geometrical variability. The model was validated by comparison with two sets of clinical data. The model provides a quantitative understanding of the canal and middle ear resonances around 500 and 1800 kHz, respectively, and also predicts the effects of the first resonance mode of the middle-ear cavity (around 6 kHz) as well as the first and second standing-wave modes in the ear canal (around 7.2 and 9.6 kHz, respectively).

## **5.1 Introduction**

Acoustic input immittance provides information about the status of the outer and middle ear by providing a measure of the mobility of the ear components in response to the acoustic excitation. The term immittance refers to either impedance  $Z$  or admittance  $Y$ . Impedance is calculated by dividing the sound pressure by the volume velocity, and admittance is the reciprocal of impedance. Both quantities are complex numbers, and they are usually reported as magnitudes and phases. The measurement can be done either under ambient pressure or with a pressurized ear canal. The latter type of measurement is referred to as tympanometry. Tympanometry is most often done with a 226-Hz probe tone. Multi-frequency immittance measurements have been shown to improve the test sensitivity in some cases of outer-ear and middle-ear pathology (e.g., Shahnaz and Polka, 1997). More information can be obtained quickly over a broad frequency range by using a wideband stimulus (e.g., Keefe et al., 1993).

Although tympanometry provides reasonably easy-to-interpret results for adult ears, and normative

data for adult responses are available, it has been shown to produce significantly different results in infants less than seven months old (e.g., Paradise et al., 1976; Paradise, 1982; Holte et al., 1990). Holte et al. (1991), Keefe et al. (1993) and Sanford and Feeney (2008) ascribed the differences to the maturation of the ear canal and middle ear during the first postnatal months. For example, the newborn ear-canal is surrounded by soft tissue along all of its length (McLellan and Webb 1957) and the middle-ear air cavity becomes larger due to growth of the antrum and mastoid air cells throughout childhood (Anson and Donaldson, 1992, p. 25).

At low frequencies, because of the long wavelengths of the sound in air (e.g., 170 mm at 2 kHz) in comparison with the canal length (~15 mm) and the dimensions of the middle-ear air cavity, the pressure is distributed almost uniformly inside the canal and the air cavity and across the TM. It is therefore reasonable to treat the ear canal and air cavity as discrete (lumped) immittance elements (e.g., Shanks and Lilly, 1981; Stinson et al., 1982). Based on this assumption, we developed linear finite-element models of the newborn ear canal and middle ear and analyzed their responses to sound frequencies up to 2 kHz (Motallebzadeh et al., 2013b, 2015). In those studies, sound pressure with an amplitude of 0.2 Pa root mean square (80 dB SPL) was applied uniformly on the surfaces of the ear canal and tympanic membrane; the volumes of air inside the canal and inside the middle-ear cavity were modelled as two compliance elements and the individual contributions of the ear canal and middle ear to the total immittance response of the ear were investigated.

At higher frequencies, however, the sound pressure is less uniform within the ear canal, across the surface of the TM, and within the middle-ear cavity. Gilman and Dirks (1986), for example, listed the sources of problems occurring in immittance measurements at higher frequencies: (1) standing waves are produced in the ear canal by reflection of sound from the TM; (2) variation of the TM impedance with frequency alters the positions of the standing waves; (3) the geometry of the canal (non-uniform cross-section) and the angle of the TM affect the pressure distribution in very complicated ways at high

frequencies; and (4) evanescent waves (waves that decay exponentially within a short distance) are present at both the TM and the probe-tip locations. For example, Stinson et al. (1982) measured the sound-pressure distribution in 13 adult ear canals between 5 and 10 kHz and reported differences between the SPL at the TM and the SPL at the canal entrance that were greater than 18 dB.

Energy reflectance has been proposed as an alternative to immittance that is insensitive to the probe position (e.g., Stinson et al., 1982; Keefe et al., 1993; Voss and Allen, 1994). Normative reflectance responses for adults (e.g., Liu et al., 2008) and newborns (e.g., Merchant et al., 2010) have been reported in the literature. However, energy-reflectance measurements are still sensitive to the insertion depth of the probe tip inside the canal in newborns, because the soft tissue surrounding the ear canal absorbs some portion of the energy.

The spatial distribution of sound pressure in the ear canal has been investigated with analytical approaches (e.g., Rabbitt, 1988; Stinson, 1985a; Stinson and Khanna, 1989) and also with 3-D finite-element models that take into account the fluid-structure interactions (FSI). Day and Funnell (1990) presented a finite-element model with a very simplified geometry for the human ear canal and TM. Gan et al. developed more realistic models of the human ear and investigated the pressure distribution in one chamber (ear canal, 2004), two chambers (canal and middle-ear cavity, 2006), and three chambers (canal, cavity, and the fluid inside the cochlea, 2007 and 2009). Lee et al. (2010) modelled the effects on the displacement of the umbo when the geometry of the middle-ear cavity was altered. Ihrle et al. (2013) used FSI modelling to study the nonlinear behaviour of the middle ear in response to large static pressures. Vollandri et al. (2014) studied the modal frequencies inside the canal with two different FSI approaches, based on finite-element shape functions that were either standard (polynomial) or ‘generalized’ (non-polynomial). None of the previous analytical or numerical studies have considered the effects of non-rigid ear-canal walls on the sound-pressure distribution and the interaction with the components of the ear.

In this study, we extended our previously developed linear finite-element models of the newborn ear canal and middle ear by taking into account the interactions between the ear structures and the non-uniform sound pressures in the two chambers bounded by (a) the ear-canal wall and the TM, and (b) the TM and the walls of the middle-ear cavity. This model enables us to study the wideband input immittance as well as the spatial distribution of the sound pressure in the canal and the middle-ear cavity. The results were validated in comparison with available clinical data. In addition, the influence of the material properties, the measurement position and geometrical variations were explored.

## **5.2 Methods**

### **2.1 3-D geometry**

The geometries used here for the ear-canal and middle-ear models were almost the same as in Motallebzadeh et al. (2015), the only differences being small changes in the geometry of the canal, and the fact that an explicit model of the middle-ear cavity was added to the model. The middle-ear cavity includes a set of air-filled and inter-connected spaces within the temporal bone consisting of the tympanic cavity, aditus, antrum, and mastoid air cells. As in our earlier paper, the models were reconstructed from a clinical X-ray CT scan (GE LightSpeed16, Montréal Children's Hospital) of a 22-day-old newborn's right ear. The scan had a pixel size of 0.187 mm and a slice thickness of 0.625 mm with a 0.125-mm overlap, resulting in a slice spacing of 0.5 mm. Fie, Tr3 and Fad (three locally developed programs, available at <http://www.audilab.bme.mcgill.ca/sw/>) were used to generate a surface model for each structure. Gmsh (<http://www.geuz.org/gmsh/>) was then used to generate a 3-D solid model with tetrahedral elements, and the solid models of the various structures were combined using Fad. The complete model (Fig. 5–1) consists of the soft tissue surrounding the lumen of the ear canal; the tympanic membrane (TM), malleus, incus, anterior malleolar ligament (AML), and two bundles of the posterior incudal ligament (PIL); and the middle-ear cavity. More information about the

thickness distribution assumed for the TM can be found in Motallebzadeh et al. (2015).

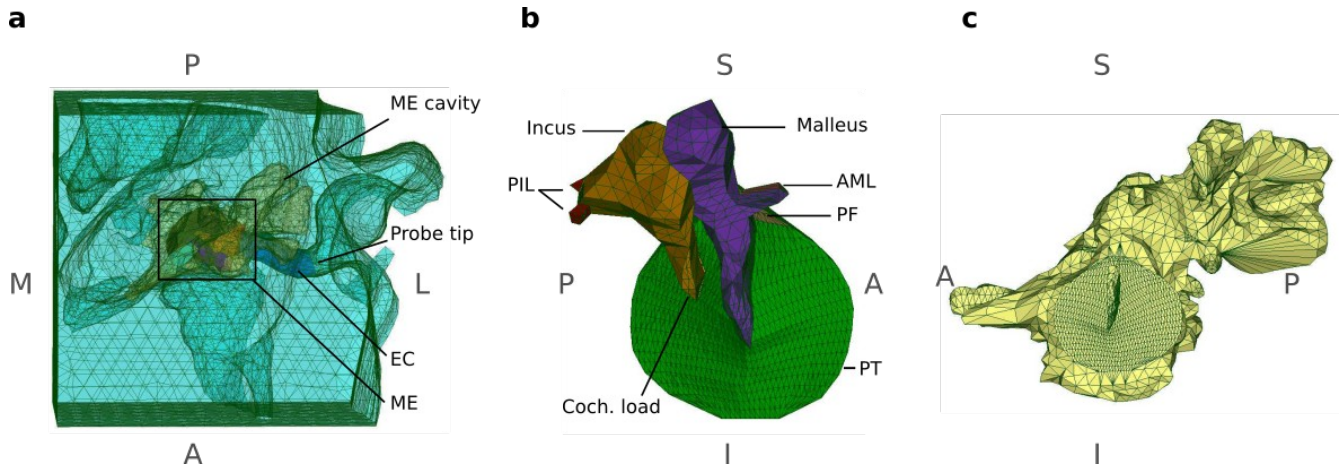


*Fig. 5–1. Meshed geometry of the finite-element model. (a) Superior view of the overall model including the ear canal, surrounding soft tissue, middle ear and middle-ear cavity. (The cavity is presented as partially transparent to provide better visualization of other parts.) (b) Expanded medial view of the middle-ear model, with the TM annulus almost parallel to the page. (ME = middle ear; PIL = posterior incudal ligament; AML = anterior malleolar ligament; PT = pars tensa; PF = pars flaccida; S = superior; I = inferior; M = medial; L = lateral; A = anterior; P = posterior). (c) Expanded lateral view of the middle-ear cavity, with the TM annulus almost parallel to the page.*

### 5.2.2 Material properties

The intensity of the probe tone in immittance measurements is low enough that linear elastic material properties can be used for the ear. As described in Motallebzadeh et al. (2015, Section 2.2), in the absence of experimental data, ranges of plausible values were adopted for the material properties. The material parameters of the ear components, listed in Table 4–1 are the same as in Motallebzadeh et al. (2015). The air enclosed in the ear canal and middle-ear cavity was modelled as a compressible, inviscid medium with a density of  $1.22 \text{ kg/m}^3$  and a speed of sound within it of  $340 \text{ m/s}$ .

### 5.2.3 Boundary and loading conditions

The ear-canal surface was clamped where it is in contact with the probe tip, because the probe tip is assumed to be securely held in the canal. The peripheral border of the TM and the ends of the AML and PIL were clamped at the places where they connect to the temporal bone, and the temporal-bone surfaces, which delimit both the soft tissues and the middle-ear cavity, were also clamped.

A harmonic velocity source with a constant amplitude of 0.00015 m/s was applied normal to the medial surface of the probe tip (which had a surface area of 13.2 mm<sup>2</sup>) to represent an acoustic driver delivering the sound energy into the ear canal. This particular velocity value was set in order to generate a pressure of 80dB SPL (typical of clinical measurements) at 250 Hz in the baseline model. The same input velocity was applied at frequencies from 25 to 10 000 Hz in 25-Hz steps and the input admittance of the model was calculated for each frequency.

### **5.2.4 Finite-element mesh**

The volume elements of the mesh consisted of second-order TETRA10 tetrahedra and the interface elements (between fluid and structural elements) consisted of second-order TRIA6 triangles. The ear-canal model consisted of 45 991 elements (17 972 and 28 039 elements for the air in the canal and the surrounding soft tissues, respectively). The middle-ear mesh consisted of 29 430 elements (23 102, 440, 5 888 and 11 393 elements for the TM, the ligaments, the ossicles, and the volume of the middle-ear cavity, respectively).

There were at least 25 nodes along the canal length; for a wavelength of 34 mm at 10 kHz, this more than satisfies the recommendation for at least 10 nodes per wavelength (e.g., Ihrle et al., 2013).

### **5.2.5 Computational methods**

#### *5.2.5.1 Finite-element solver*

Code\_Aster (<http://www.code-aster.org>) version 11.5 was the finite-element solver in this study. It is free (libre) and open-source software. The complex linear dynamic pressure responses of the models were obtained using the DYNA\_LINE\_HARM module, which calculates the steady-state response of a model for a harmonic excitation. Simulations were performed on the supercomputer Guillimin of McGill University. Guillimin is a part of the Compute Canada national High Performance Computing platform. It is a cluster of Intel Westmere EP Xeon X5650 and Intel Sandy Bridge EP E5-2670

processors running under the CentOS 6 Linux distribution. The frequency range of 25–10 000 Hz was divided into four jobs, each consisting of 100 frequencies in 25-Hz steps. We ran a maximum of 12 jobs at a time on nodes with 16 processors each, each job on a single processor. The run times were about 450 minutes per job for a total of 1800 minutes for the complete frequency range for one simulation scenario.

#### *5.2.5.2 Implementation of fluid-structure interaction*

Fluid-structure interactions are modelled by coupling the constitutive equations of the two domains, fluid (air) and structure (ear components), on their interface surfaces. At the interface there are two conditions that should be satisfied: (1) the continuity of the normal stresses, and (2) the continuity of the normal velocities. The simultaneous satisfaction of these two conditions couples the two domains. The detailed mathematical formulation can be found elsewhere (e.g., Greffet, 2013).

#### *5.2.5.3 Admittance calculation*

The impedance components (resistance  $R$  and susceptance  $X$ ) were calculated by dividing the real and imaginary components of the pressure (usually taken from a node on the medial surface of the probe tip) by the input volume velocity at each frequency. Admittance is the reciprocal of impedance and has two components, conductance  $G$  and susceptance  $B$ . The admittance magnitude and phase were calculated as  $\sqrt{G^2+B^2}$  and  $\text{Tan}^{-1}(B/G)$ , respectively.

### **5.2.6 Sensitivity analyses**

In this study we performed four sensitivity analyses. First, all nine combinations of the three ear-canal scenarios and three middle-ear scenarios (low-impedance, baseline and high-impedance for each) were simulated to provide estimates of the contributions of the canal and middle-ear responses to the total ear model.

Second, a traditional one-parameter-at-a-time analysis was performed to investigate the effects of these parameters. As stated in Section 5.2.2, plausible ranges were established for the material parameters of the ear components. The range between the minimum and maximum values for each parameter (shown in Table 1) was divided into 4 intervals so each parameter had  $p = 5$  evenly spaced values.

Third, we evaluated the effect of the location of the pressure measurement point by examining the pressures at 5 nodes in the canal, between 0.0 and 6.0 mm from the medial surface of the probe tip. This procedure was suggested by the fact that Keefe et al. (1993) extended the microphone probe approximately 3 mm beyond the surface of the foam eartip to minimize the effects of evanescent waves between the source and the receiver.

Fourth, to provide an estimate of the effects of anatomical variability, the geometry of the model was scaled by  $-10$ ,  $-5$ ,  $+5$  and  $+10\%$  in the  $x$ ,  $y$  and  $z$  directions separately and also in all three directions simultaneously. The  $x$ ,  $y$  and  $z$  directions represent the lateral-medial, posterior-anterior and superior-inferior directions, respectively.

### **5.2.7 Clinical data**

As in our previous study, two sets of clinical data were used for comparison with the model. The first set consisted of the impedance measurements obtained by Keefe et al. (1993) under ambient pressure in a group of 1-month-old infants, for frequencies from 125 to 10 700 Hz with a 1/3-octave resolution. The second set consisted of admittance measurements that we performed as part of another project, on a group of 23 infants with ages between 14 and 28 days, for frequencies from 250 to 8 000 Hz with 1/12-octave resolution. That study was approved by the Institutional Review Board of the McGill University Health Centre. The measurements were made with a wideband tympanometry research system (WBTymp 3.2, Interacoustics Inc.). All measurements except one were performed in the

Otolaryngology out-patient clinic of the Montréal Children's Hospital. More details about the measurement procedure can be found in Pitaro (2013).

## 5.3 Results

### 5.3.1 Sound-pressure and admittance responses

Fig. 5–2 shows the pressure distributions inside the canal and middle-ear cavity for frequencies of 6.1, 7.2 and 9.6 kHz, representing the first acoustic resonance of the middle-ear cavity and the first and second standing-wave modes inside the canal, respectively, for the baseline model. The descriptions of these features are provided later in this section. Fig. 5–3 shows the pressure (panel a), admittance magnitude (panel b) and admittance phase (panel c) frequency responses for a measurement point at the medial face of the probe tip. (Note that, since the admittance is proportional to the reciprocal of the pressure, minima and maxima of pressure correspond to maxima and minima of the admittance, respectively.) The solid black curves represent the responses of the overall model with baseline parameters. The other curves represent the responses obtained when one or more parts of the model are removed or made rigid. The dashed black curves represent the baseline model with open middle-ear cavity. The red curves represent the responses of the simplest case, namely, a rigid canal with a rigid TM. The green curves represent the behaviour of the non-rigid canal only – the TM is rigid and so the middle ear does not contribute to the responses. The blue curves represent the responses of models with a rigid canal and either an open middle-ear cavity (dashed curves) or a closed cavity (solid curves). In Fig.5– 3a & b the upper limits of the pressure and admittance magnitude axes are limited to 1 Pa and 225 mm<sup>3</sup>/s/Pa, respectively, clipping some of the curves at some frequencies in order to provide better visualization of other parts of the curves. An inset shows the admittance magnitudes with an expanded vertical scale for frequencies below 1 kHz. Comparisons among these models reveal the contributions of the different components to the overall response of the newborn ear. The important features are

pointed out by numbered arrows in the figure and can be summarized in order from low to high frequencies as follows, with the paragraph numbers corresponding to the arrow numbers. (The focus is on panel b unless otherwise stated.)

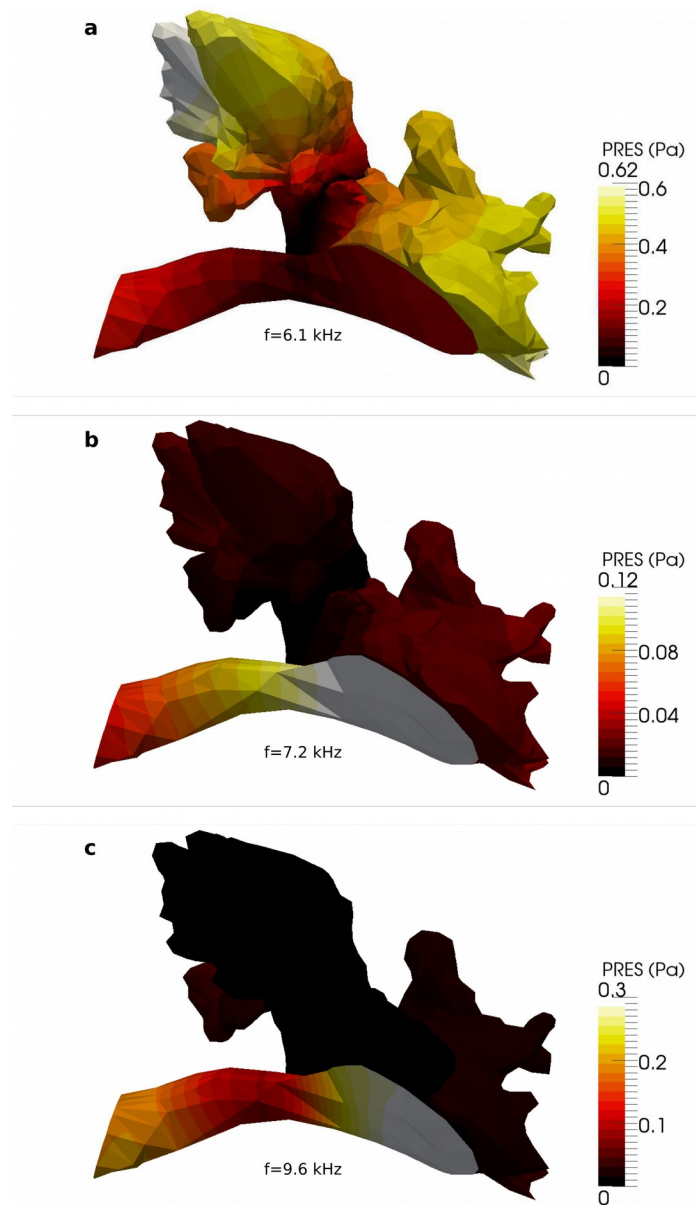


*Fig. 5–2. Posterior view of pressure distribution map inside the ear canal and middle-ear cavity in response to a harmonic velocity source with a constant amplitude of 0.00015 m/s, normal to the medial surface of the probe tip. (a) First resonance mode of the middle-ear cavity (6.1 kHz). (b) First standing-wave mode inside the ear canal (7.2 kHz). (c) Second standing-wave mode inside the ear canal (9.6 kHz).*

1. A broad resonance is seen at frequencies around 650 Hz (green curve, inset figure) for a model

with a rigid TM and compliant canal wall. The feature disappears when the canal wall is rigid (red curve).

2. A resonance peak is seen at 1.05 kHz for the open-cavity models (dashed blue and dashed black curves). Changing the canal wall from rigid (dashed blue curve) to compliant (dashed black curve) does not alter the curve significantly in this frequency region (less than a 4% increase in magnitude and 25-Hz shift of the peak). Having a closed middle-ear cavity decreases the resonance magnitude by 5% and shifts it upward to 1.2 Hz (solid blue and black curves).
3. A sharp resonance occurs at 5.1 kHz in the models with a rigid TM, whether the canal walls are rigid or compliant (solid red and green curves, respectively). At this frequency the first standing-wave mode of the model occurs inside the canal; the pressure has a node (minimum) at the entrance (as seen at 5.1 kHz in panel a) and an anti-node (maximum) at the rigid medial end of the canal.
4. Another resonance, which is very sharp, happens at 6.1 kHz in the models with closed cavity (solid blue and black curves), representing the first resonance of the middle-ear cavity. The pressure distribution of this mode is shown in Fig. 5–2a.
5. Admittance maxima are seen at 7.2 kHz for the models with compliant canal wall and TM, whether the cavity is open or closed (blue and black, dashed and solid curves). This represents the first standing-wave mode in the canal, which occurs at 5.1 kHz when the TM is rigid (see item 3 above). The pressure distribution at this frequency is presented in Fig. 5–2b for the baseline model; there is a pressure node at the entrance of the canal and an anti-node at the medial end. The models with open cavities have slightly higher magnitudes (around 10%) for this feature (dashed blue and black curves).
6. Admittance minima are observable at frequencies in the vicinity of 8.2 kHz in the models with a rigid TM, whether the canal walls are rigid or compliant (solid red and green curves,

respectively). At this frequency the second standing-wave modes occur inside the canal, resulting in pressure anti-nodes at both the entrance and the medial end of the canal. The pressures in these two models have sharp peaks at this frequency (panel a).

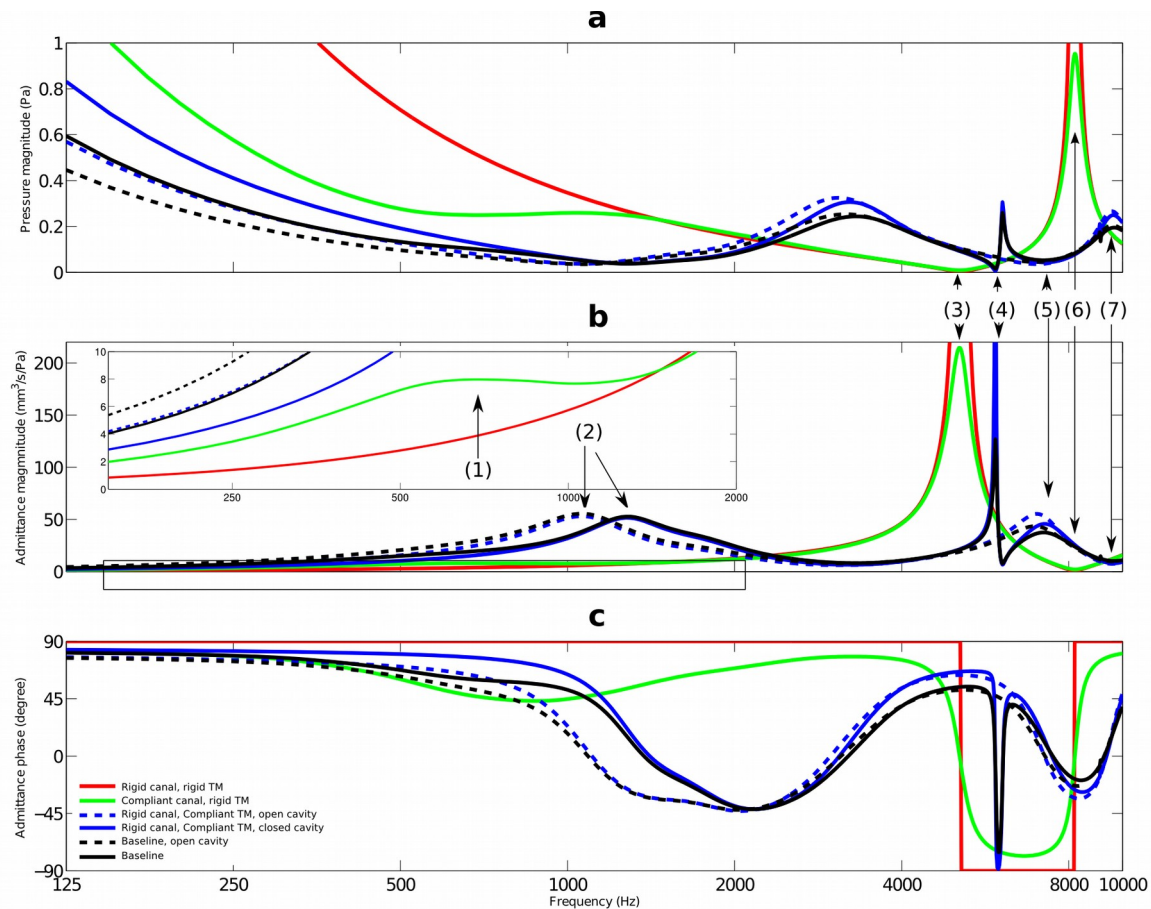


Fig. 5–3. Pressure and admittance responses of the ear models at the medial surface of the probe tip. (a) Pressure magnitudes. (b) Admittance magnitudes. (c) Phases. The inset shows a magnified view of the admittance magnitudes at frequencies between 150 and 2000 Hz. Features indicated by arrows and numbers are discussed in the text.

7. Admittance minima are observable at frequencies in the vicinities of 9.6 kHz for the models with compliant canal wall and TM, whether the cavity is open or closed (blue and black, dashed and solid curves). This represents the second standing-wave mode in the canal, which occurs at 8.2 kHz when the TM is rigid. The models with open cavities have slightly lower magnitudes (a difference of less than 10%) at this frequency (dashed blue and black curves). The pressure distribution at 9.6 kHz is presented in Fig. 5–2c for the baseline model; there are pressure anti-

nodes at both the entrance and the medial end of the canal.

### 5.3.2 Sensitivity analysis

#### 5.3.2.1 Combinations of low-, baseline-, and high-impedance models

Admittances for all nine combinations of the three ear-canal and three middle-ear scenarios (low-impedance, baseline and high-impedance for each) are presented in Fig. 5–4. In this figure each pair  $C_i$ - $M_j$  corresponds to the combination of the canal model  $i$  and the middle-ear model  $j$ , and the indices  $i = 1, 2$  and  $3$  represent the low-impedance, baseline and high-impedance models, respectively. In all models with the low-impedance canal model (green curves), a peak with a magnitude of  $\sim 27$  mm<sup>3</sup>/s/Pa is visible at  $\sim 250$  Hz. A drop and a subsequent rise of the phase response between 100 and 1000 Hz are also observable for these models. As the canal becomes stiffer (red and blue curves), the local admittance peak at low frequencies merges with that of the middle-ear resonance in the frequency range of 1–2 kHz. The resonances of the models at frequencies in the vicinity of 1.5 kHz are not affected significantly by the conditions of the ear canal, so they may be taken to mainly represent the middle-ear resonances. Around 7.2 kHz (the occurrence of the second standing-wave mode inside the canal) the stiffer canals have increased admittance magnitudes but the stiffer middle ears have decreased magnitudes.

The phases of the models with stiffer canals (red and blue curves) remain close to  $90^\circ$  over a broader frequency range below 1 kHz. Between 1 and 3 kHz, the canal condition does not effect the phase response significantly, but the stiffer middle ears have higher phases (e.g., blue curves). Between 3 and  $\sim 7.8$  kHz the stiffer canals show higher phase values, and above 7.8 kHz they have decreased phases. The stiffness of the middle ear works in the opposite direction above 3 kHz: the stiffer middle ears show lower phase values between 3 and  $\sim 7.8$  kHz and higher values above 7.8 kHz.

### 5.3.2.2 Effects of material parameters

Since the main goal of clinical admittance measurements is to characterize the middle-ear response, the features that we looked into were at frequencies in the vicinity of the middle-ear resonance (between 1 and 2 kHz). The results of the one-parameter-at-a-time sensitivity analysis are presented in Fig. 5–5, for two features of the admittance (maximum magnitude in the upper panel and frequency of the maximum in the lower panels).

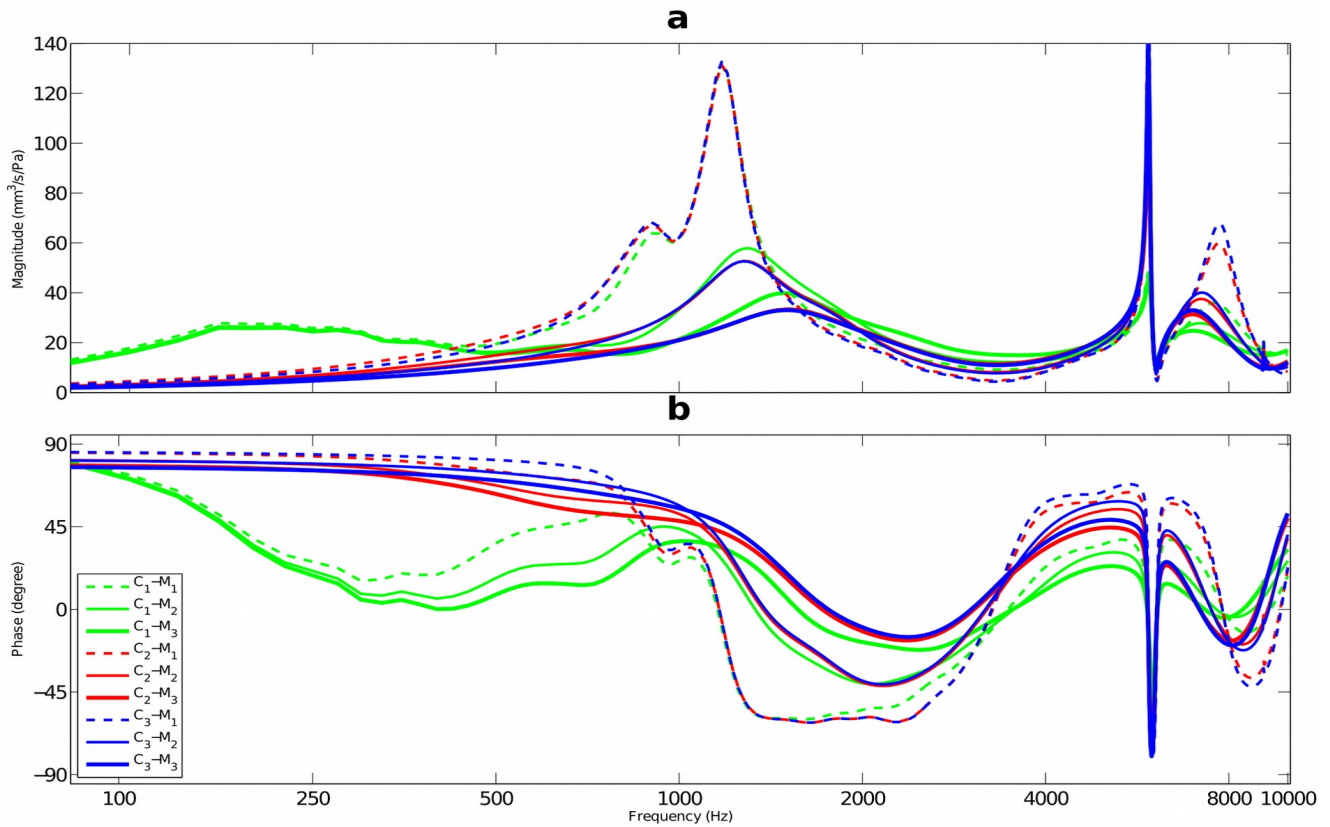


Fig. 5–4. Admittance responses of the combinations of three ear-canal and three middle-ear models. (a) Admittance magnitudes. (b) Phases. Each pair  $C_i$ - $M_j$  corresponding to the combination of the canal model  $i$  and the middle-ear model  $j$ ; the indices  $i, j = 1, 2$  and  $3$  represent the low-impedance, baseline and high-impedance models, respectively.

All material parameters of the ear-canal and middle-ear models (i.e., stiffness, damping ratio, density, Poisson’s ratio, stapes mass and cochlear load) were included in this analysis. Here only parameters with effects greater than 1% on either criterion are reported. The parameters shown in

Fig. 5–5 upper panel, in order of decreasing influence on the maximum admittance magnitude of the ear model, are the damping ratio  $\zeta_{pt}$  and Young’s modulus  $E_{pt}$  of the pars tensa; the density  $\rho_{st}$  of all soft tissues in the model; the Young’s modulus  $E_{st}$  of the soft tissue surrounding the canal; and the Poisson’s ratio  $\nu$  of the soft tissues. The parameters with the greatest effects on the maximum admittance magnitude are  $\zeta_{pt}$  and  $E_{pt}$  with maximum deviations of 80 and 46%, respectively. The effects of the other parameters are less than 7%. The coefficients of determination for these parameters are 0.88, 0.82, 0.99, 0.51 and 0.97, respectively, meaning that only  $E_{st}$  has a notably nonlinear effect; it has an effect mainly at its lowest value, which is only about one tenth as large as its baseline value.

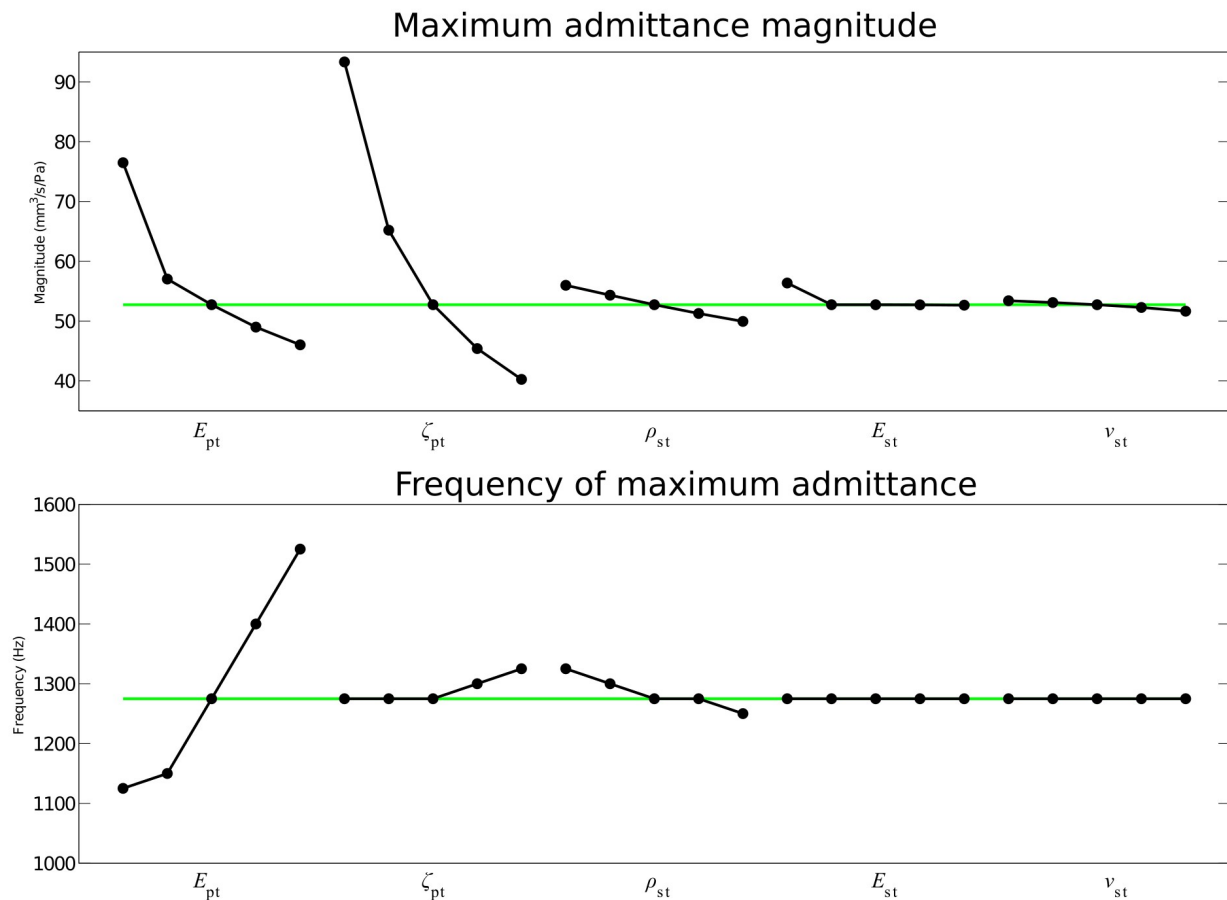


Fig. 5–5. One-variable-at-a-time sensitivity analysis, showing the influence of the material parameters on the maximum admittance magnitudes (upper panel) and the corresponding frequencies (lower panel) for the ear models.  $E_{pt}$  = Young’s modulus of the pars tensa;  $\zeta_{pt}$  = damping ratio of the pars tensa;  $\rho_{st}$  = density of all soft tissues in the model;  $E_{st}$  = Young’s modulus of soft tissue surrounding the canal;  $\nu_{st}$  = Poisson’s ratio of all soft tissues.

Most of the material parameters have very small effects on the frequency of the maximum admittance in the frequency range of interest, as shown in Fig. 5–5 lower panel. The most important parameter is the pars-tensa Young’s modulus  $E_{pt}$ , shifting the maximum frequency by 250 Hz. The pars-tensa damping ratio  $\zeta_{pt}$  and the soft-tissue density  $\rho_{st}$  shift the maximum frequency by 50 Hz. The coefficients of determination are 0.96, 0.78 and 0.94 for the pars-tensa Young’s modulus  $E_{pt}$ , damping ratio  $\zeta_{pt}$  and soft-tissue density  $\rho_{st}$ , indicating that  $\zeta_{pt}$  is the only parameter with a notably nonlinear effect.  $E_{pt}$  has an almost linear effect at values higher than 4 Mpa.

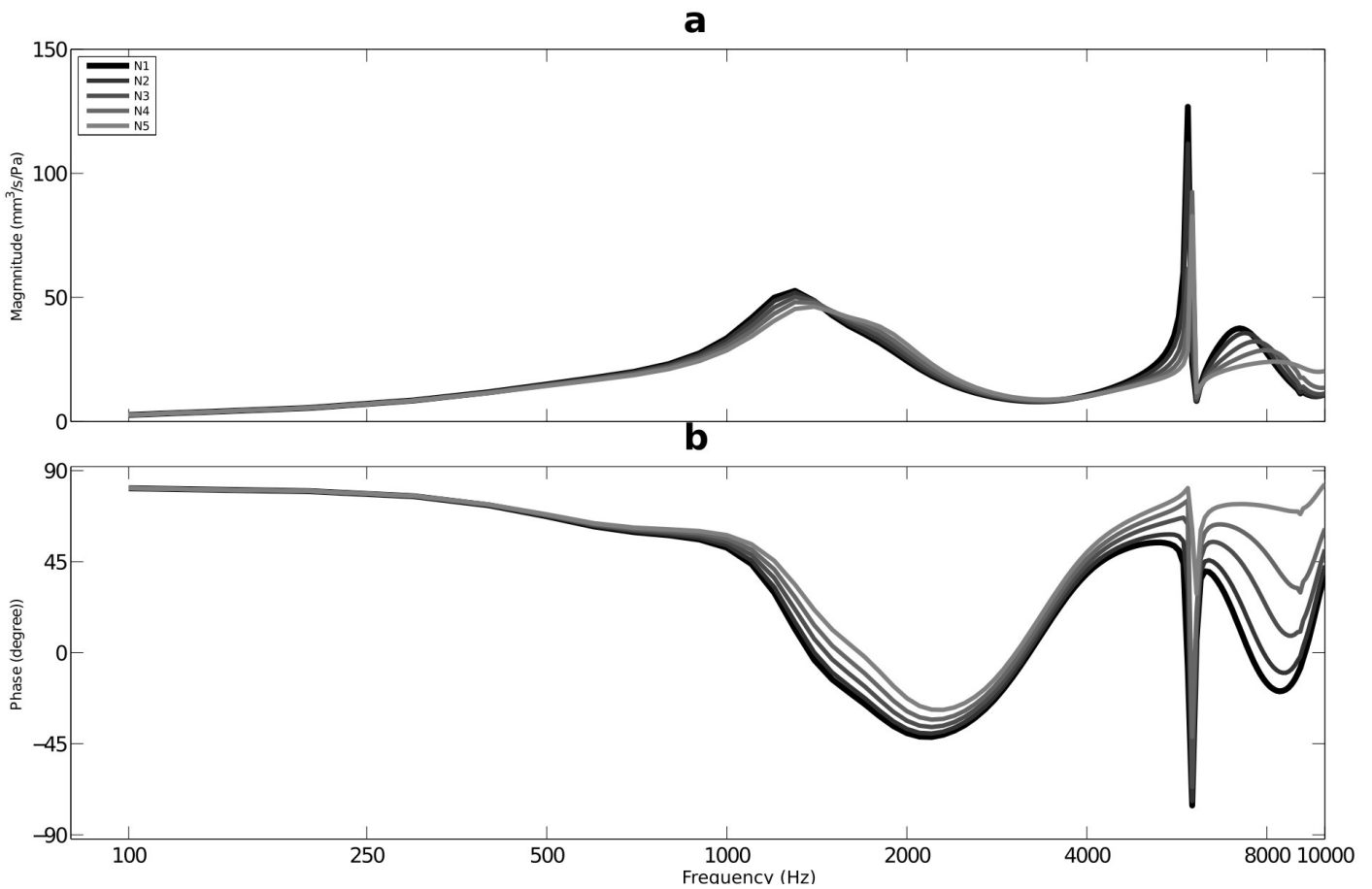


Fig. 5–6. Admittance responses of the measurements at 5 nodes along the ear canal: Nodes N1 to N5 are at 0.0, 1.5, 3.0, 4.5, 6.0 mm, respectively, from the medial surface of the probe tip. (a) Admittance magnitude. (b) Phase.

### 5.3.2.3 Effect of measurement location

To investigate the effects of the distance between the source and the measurement point which was

taken to be 3 mm by Keefe et al. (1993), we recorded the admittance data at 5 nodes inside the canal at distances of 0.0, 1.5, 3.0, 4.5 and 6.0 mm from the medial surface of the probe tip (Fig. 5–6).

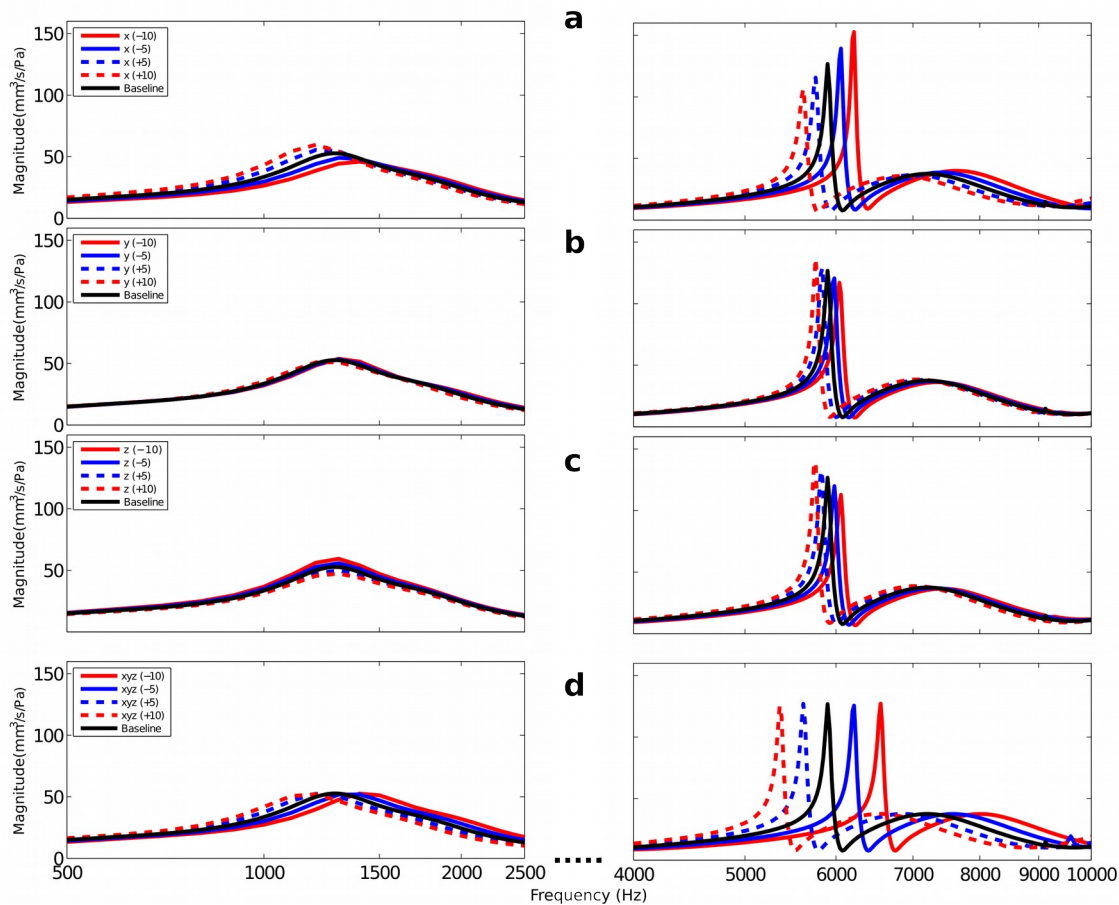


Fig. 5–7. Sensitivity analysis of geometry-variation effects in  $x$ ,  $y$  and  $z$  (panels a, b and c, respectively) and simultaneous variation in all directions (panel d) for  $-10$ ,  $-5$ ,  $+5$  and  $+10\%$  scaling of the baseline geometry. Frequencies from 2.5 to 4 kHz are excluded because no significant deviations occur in that range.

At frequencies below 1 kHz, the maximum difference between the admittance magnitudes calculated at 0.0 and 6.0 mm is less than 15%. The first resonance peak not only decreases in magnitude (from  $52.6 \text{ mm}^3/\text{s}/\text{Pa}$  at 0.0 mm to  $46.2$  at 6.0 mm (a change of about 12%) but also becomes broader and shifts from 1300 to 1400 Hz. The admittance peak due to the second standing-wave mode inside the canal is also significantly affected by the choice of the measurement point: as the distance from the driving point increases from 0 to 6 mm, the admittance peak in the vicinity of

7.2 kHz decreases in magnitude (by up to 35%) and shifts to 8.2 kHz.

#### *5.3.2.4 Effect of geometry variations*

In Fig. 5–7, panels a, b and c compare the geometry-variation effects in  $x$ ,  $y$ ,  $z$ , respectively, and panel d presents the effects of simultaneous variation in all directions, for  $-10$ ,  $-5$ ,  $+5$  and  $+10\%$  scaling of the baseline geometry. Since no significant deviations are observable between 2.5 and 4 kHz, this frequency range was excluded in order to provide better visualization of the other parts of the curves. As described in Section 5.2.9, the  $x$ ,  $y$  and  $z$  directions mainly represent the lateral-medial, posterior-anterior and superior-inferior directions, respectively. The most influential dimension is  $x$ , because it changes the canal length more than the others do. As the canal becomes longer, the middle-ear resonance shifts to lower frequencies (e.g., from 1.4 to 1.1 kHz for elongations from  $-10$  to  $+10\%$ ). The resonance magnitude is also increased by 30%, from 46.0 to 59.7 mm<sup>3</sup>/s/Pa. The resonance of the middle-ear cavity (which also extends mainly in the lateral-medial direction) also shifts to lower frequencies (from 6.2 kHz to 5.6 kHz, at  $-10$  and  $+10\%$  elongation, respectively). The elongations in the other two directions do not affect the admittance response significantly, with a maximum magnitude change of 15% and a maximum frequency shift of 25 Hz for elongations in the range of  $\pm 10\%$ . The combined scaling in all directions simultaneously (panel d) cancels out the effects of elongations in each individual direction to some extent at the middle-ear resonance, where the resonance magnitude changes by less than 1% (from 52.6 mm<sup>3</sup>/s/Pa to 52.1) and the corresponding frequency shifts by only  $\sim 200$  Hz (from 1.4 to 1.2 kHz) for elongations from  $-10$  to  $+10\%$ . However, the effect on the middle-ear-cavity resonance is significantly enhanced for simultaneous elongation from  $-10$  to  $+10\%$  in all directions simultaneously, as the corresponding frequency shifts from 6.5 kHz to 5.3 kHz.

### **5.3.3 Comparison with clinical data**

The sensitivity analyses in Sections 5.3.3.1 and 5.3.3.2 showed that the canal response has a

pronounced effect on the total admittance of the ear at frequencies below 1000 Hz. Comparing the behaviour of the ear model for the nine combinations of canal and middle-ear parameters with two sets of clinical data (described in Section 5.2.7), it was concluded that the main feature of the clinically measured low-frequency response (a peak at frequencies below 1 kHz due to the canal resonance) could be matched by assigning an intermediate impedance to the canal parameters (an intermediate stiffness of  $E = 80$  kPa together with a high damping ratio of  $\zeta = 0.4$ ). These are the same adjusted parameters that we adopted in our previous model (Motallebzadeh et al. 2015). A comparison of such an adjusted model with the clinical data is presented in Fig. 5–8. As shown in the inset figure, the resonance of the ear canal for the adjusted model happens at  $\sim 500$  Hz (arrow 1). The corresponding peak in the mean data of Keefe et al. (1996) is around 400 Hz and the first peaks of our individual subjects are spread over the frequency range of 250–750 Hz, with most being around 250 Hz.

The resonance of the middle ear of the adjusted model results in a magnitude peak of  $34.7$  mm<sup>3</sup>/s/Pa at 1550 Hz (arrow 2), and the width of the peak (as defined by the frequencies at which the magnitudes are 90% of the peak value) is 450 Hz. The mean curve of Keefe et al. shows a resonance peak of  $30.0$  mm<sup>3</sup>/s/Pa at around 2 kHz. The resonances of our individual subjects are spread from about 1 to 2.5 kHz. Averaging the individual curves smears their peaks, resulting in a broad resonance peak (with about 3 small local peaks) between 1 and 2 kHz. This frequency range covers the corresponding frequency of the adjusted model, with a good match in magnitude values.

The adjusted model predicts low admittance magnitudes between the frequencies of 3 and 5 kHz. This local minimum is visible in both sets of clinical data but with higher magnitudes than those of the model.

The resonance of the middle-ear cavity of the model causes a sharp peak of admittance magnitude at 6.1 kHz (arrow 3), followed by a minimum, and then there is another local peak at around 7.2 kHz

(arrow 4) due to the second standing-wave mode inside the ear canal (described in Section 5.3.1). The individual-subject responses show two local peaks, one between 4.5 and 5.5 kHz and another one between 5.6 and 7.2 kHz. The mean curve has two peaks in this frequency range, one at 5.0 kHz (arrow 3') and one at 6.4 kHz (arrow 4'). The data of Keefe et al., however, simply show a constantly increasing admittance at frequencies higher than 4 kHz, presumably because the frequency resolution of their measurements was not fine enough to exhibit such sharp features.

The frequencies of the minima and maxima in the phase of the model closely match those of the mean phase data of Keefe et al. (1993), but differences in the actual phase values are seen. The differences are within about  $20^\circ$  up to about 2.5 kHz but they increase to  $75^\circ$  at 5 kHz (the second maximum). The model phase shows a sharp notch  $\sim 6.1$  kHz and rises at frequencies above 8.2 kHz. This notch is not observable in the data of Keefe et al., where the phase continues to decrease after the maximum at 5 kHz. The phase of the model is within the range of phases of the individual subjects of our clinical data at all frequencies, except for the sharp notch at 6.1 kHz. The first rather sharp minimum of our mean phase occurs at 300 Hz; the corresponding minimum of the model is much more shallow and happens at 550 Hz. The first maximum of the mean phase of our clinical data has a broad peak at 800 Hz. The corresponding frequency in the model is 900 Hz, at a phase that is  $10^\circ$  lower. The second minimum of the mean phase of the clinical data occurs at 2.1 kHz. The corresponding frequency in the model is 2.4 kHz at a phase that is  $18^\circ$  lower. Two peaks of the mean measured phase response are seen at 4.3 and 5.7 kHz with a shallow notch between them. The corresponding features in the model are two maxima at 5.2 and 6.4 kHz, with a sharp notch between them. The phases of these maxima for the model are  $8^\circ$  lower and  $3^\circ$  higher than those of the mean phase of our clinical data, respectively; in both model and clinical data the second maximum is lower than the first.

### 5.3.4 Comparison with non-FSI model

In Fig. 5–9 we compare the non-FSI model from our previous study (Motallebzadeh et al., 2015) and the FSI model in this study. Three non-FSI scenarios (dashed lines), with the low-impedance, baseline and high-impedance models, are compared with the corresponding FSI models (solid lines) at frequencies up to 2.5 kHz, somewhat beyond the nominal 2-kHz frequency range of the non-FSI model.

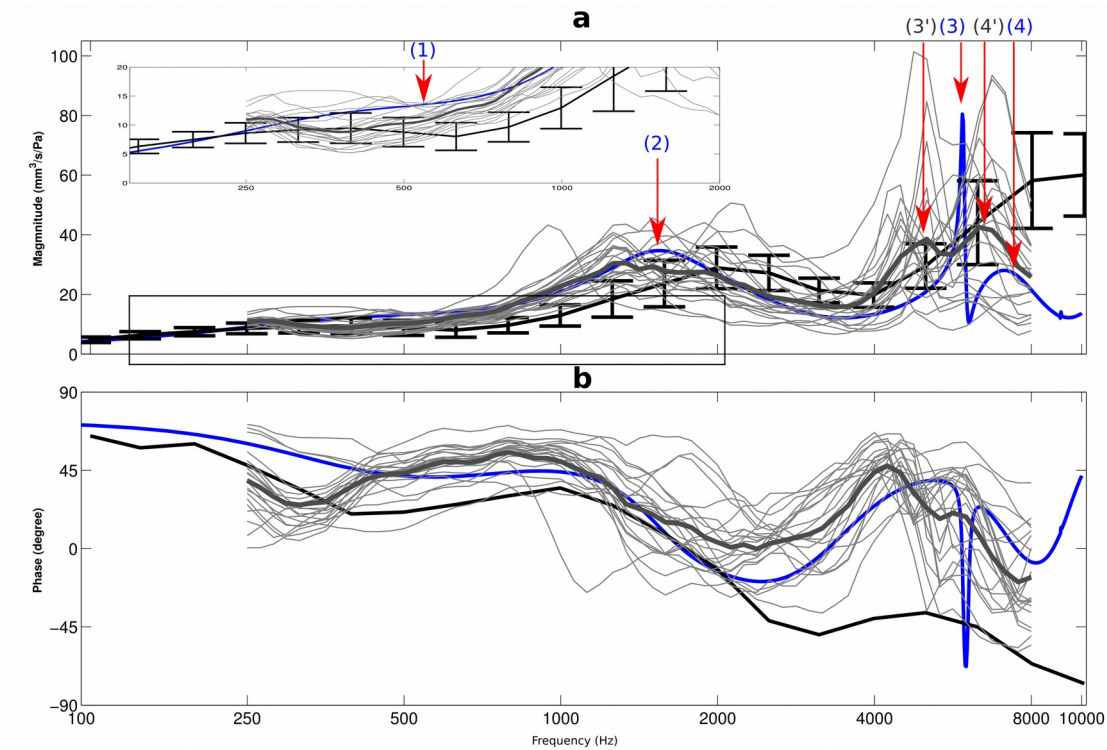


*Fig. 5–8. Results for model with adjusted parameters and comparison with two sets of clinical data. Admittance magnitudes (a) and phases (b) are presented for the 1-month-old data of Keefe et al. (1993) and for data from this study, and for the output of the model with adjusted parameters. The inset shows a magnified view of the admittance magnitudes at frequencies between 150 and 2000 Hz. Features indicated by arrows and numbers are discussed in the text.*

At frequencies up to 800 Hz, the non-FSI models show a good match with the corresponding FSI models. However, at higher frequencies the FSI models start to deviate from the non-FSI models. In the low-impedance FSI model (solid green curve), a small peak and a main peak are seen with magnitudes of 63 and 130  $\text{mm}^3/\text{s}/\text{Pa}$  at  $\sim 925$  and 1200 Hz, respectively. In the corresponding non-FSI model

(dashed green curve), these features are shifted to 950 and 1400 Hz with magnitudes of 51 and 114 mm<sup>3</sup>/s/Pa, respectively, about 19% and 12% lower, respectively. In addition, in the FSI model the resonance peak decreases smoothly up to 2.5 Hz but in the non-FSI model two shoulders appear on the downslope of the main peak, at 1650 and 2200 Hz. The baseline FSI model (solid red curve) shows a simple peak of 52 mm<sup>3</sup>/s/Pa at 1300 Hz, whereas in the non-FSI model (dashed red curve) a broad peak is seen with a maximum of 44 mm<sup>3</sup>/s/Pa at 2000 Hz and a shoulder around 1600 Hz. The peak of the high-impedance FSI model occurs at 1500 Hz with a magnitude of 32 mm<sup>3</sup>/s/Pa, while that of the non-FSI model reaches its maximum of 29 mm<sup>3</sup>/s/Pa at 2100 Hz.

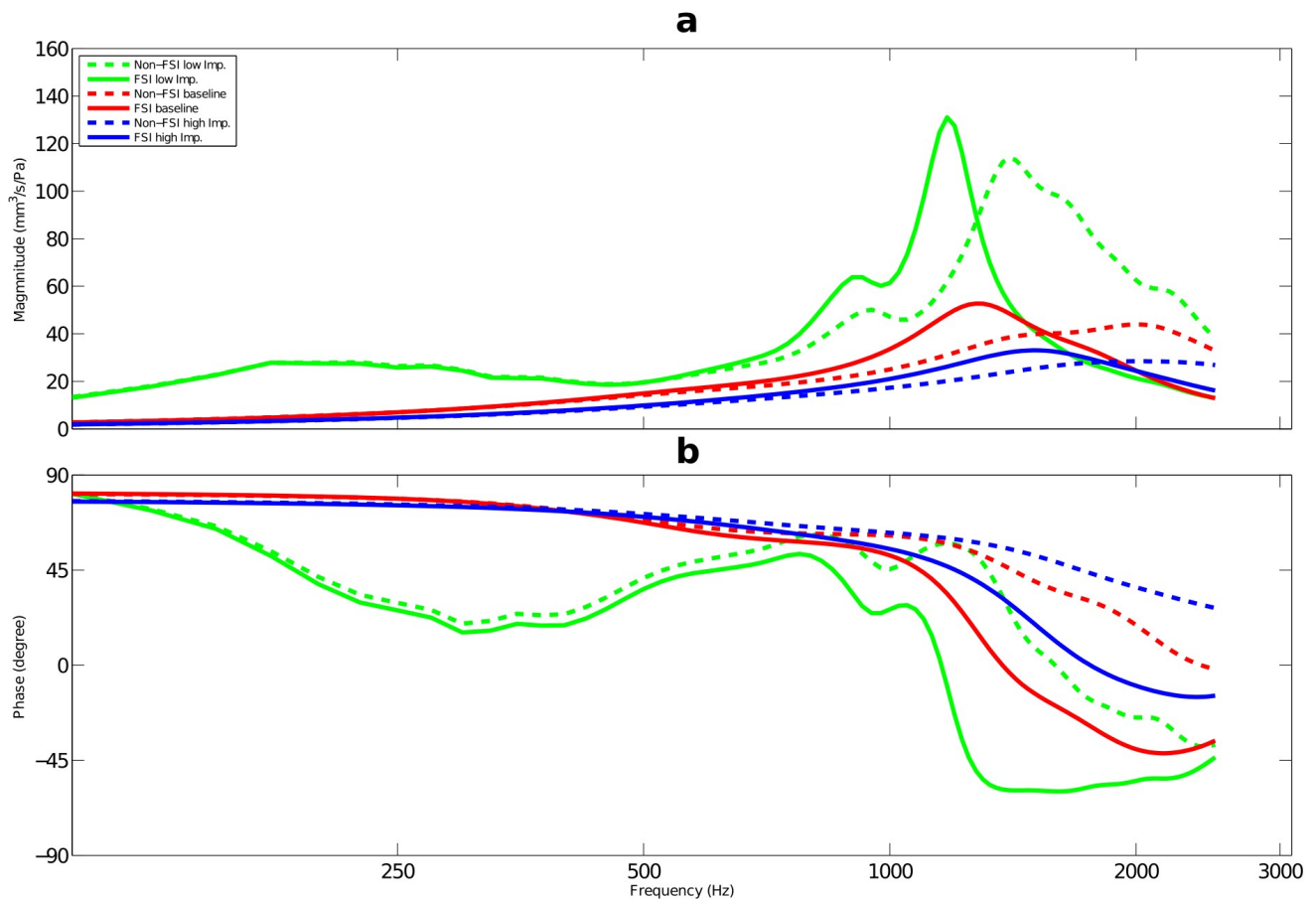


Fig. 5–9. Comparison between FSI and non-FSI models. Admittance magnitudes (a) and phases (b) are presented for low-impedance (green), baseline (red) and high-impedance (blue) parameters.

A good match between the phase responses of the FSI and non-FSI models remains up to 800 Hz (maximum of 8° difference between the low-impedance models at 800 Hz). At higher frequencies,

however, although the sequences of rises and drops are similar in the corresponding models, the phase values differ considerably. In the low-impedance models, the minimum at 950 Hz and maximum at 1050 Hz in the FSI model are shifted by 50 and 120 Hz, respectively, in the non-FSI model, and the phases are very different at higher frequencies. In the stiffer models, the corresponding models deviate by up to  $60^\circ$  (baseline models at 1800 Hz) and  $45^\circ$  (high-impedance models at 2000 Hz). The inconsistency is presumably due to the treatment of the air spaces as lumped admittance elements in the non-FSI models. In those models it was assumed that the wavelength of the sound at frequencies below 2 kHz is long enough (in comparison with the model dimensions) that we could assume a uniform pressure distribution throughout the ear canal and middle-ear cavity and across the TM surface. However, the pressure is not uniform in spite of the long wave length, because of the interaction of the incident and reflected sound waves: at 2 kHz the pressure at the entrance of the canal and the pressure at the tympanic membrane already differ by more than 30%.

## **5.4 Discussion**

### **5.4.1 Pressure distribution inside the canal and middle-ear cavity**

To the best of our knowledge, no experimental measurements have been reported for the spatial sound pressure distribution within the newborn ear canal, but there have been several such studies of adult humans and animals (e.g., Stinson et al., 1982; Stinson, 1985a, 1985b; Gilman and Dirks, 1986; Stinson and Khanna, 1989; Bergevin and Olson, 2014). Since the ear canal is longer in adults (~25 mm (Anson and Donaldson, 1992, p. 146)) than in newborns (~16 mm from the entrance to the umbo, in our model), the onset of standing waves happens at lower frequencies in adult canals. For example, Gilman and Dirks (1986) found a frequency of ~3.6 kHz for a standard ear simulator. In our model with rigid canal wall and rigid TM, the first standing-wave mode, with one node (minimum pressure) at the entrance and one anti-node (maximum pressure) at the medial end of the canal, occurred at 5.1 kHz.

The second standing-wave mode is observed at 8.2 kHz, with anti-nodes at both the entrance and the medial end of the canal.

The first standing-wave mode of a cylindrical pipe, driven at the entrance and closed at the end, happens at 5.1 kHz if its length is 16.6 mm (1/4 of the wavelength). The second standing-wave mode for such a pipe occurs at 10.2 kHz, twice the first mode, much larger than the 8.2-kHz frequency of the corresponding mode in our model with a realistically shaped but rigid ear canal and a rigid TM. To explore the discrepancy further, we also modelled waveguides shaped like truncated cones with entrance diameters of 4.4 mm (approximately the diameter of the canal in newborns) and closed terminations of diameter 9 mm (approximately the diameter of the TM), and different lengths; we observed a standing-wave pattern at 5.1 kHz for a length of 12.4 mm; however, the second standing-wave mode for such a cone with that length happens at 14.4 kHz, again much higher than 8.2 kHz. These simulations show that a realistically shaped but rigid newborn ear canal cannot be well approximated by rigid cylindrical or conical waveguides. The differences can be attributed to the variations of the cross-sectional area, the curvature along the length of the canal, and the angle of the TM at the termination. These features presumably also affect the behaviour of the newborn canal when its walls are not rigid.

The cavity in our model can be enveloped in a box of dimensions 23×18×15 mm. Treating such a box-shaped cavity as being driven at one end of the longest dimension and closed at the other end, its first standing-wave mode happens at 3.7 kHz. Since the middle-ear cavity is terminated by the TM impedance, it can be expected to have its first resonance at a higher frequency (i.e., around 6.1 kHz in our model). Due to the limited resolution of the CT images that we used for reconstructing the geometry of our model, the fine structures of the cavities (especially the mastoid air cells) and their narrow connections were modelled only very approximately. Moreover, since the air was modelled as

an inviscid fluid, the viscous losses associated with sound-pressure propagation inside the connecting passages was not modelled. Any energy absorption at the walls of the cavities was also not modelled. Although damping would not be expected to shift the resonance frequency significantly, the absence of damping does result in a resonance that is probably unrealistically sharp. The complex structure of the middle-ear cavity, including the tympanic cavity, aditus, antrum, and mastoid air-cell system (e.g., Keefe, 2015), makes the exploration of the sound-pressure distribution very challenging.

### **5.4.2 Model validation**

Holte et al. (1991) and Keefe et al. (1993) found that the resonance of the ear canal in infants less than 1 month old occurs at frequencies around 450 Hz. The corresponding frequencies in our clinical data for individual subjects are spread over the frequency range of 250 to 750 Hz. By adjusting the parameters of the model within the proposed plausible ranges, we reproduced the resonance of the canal at 500 Hz, consistent with the clinical data.

Due to their limited frequency range, Holte et al. (1991) did not observe the middle-ear resonance, but they suggested that it is beyond 900 Hz. Keefe et al. (1993) found that the overall ear resonance occurred in the vicinity of 1800 Hz. In our clinical measurements of individual subjects, the middle-ear resonance occurs in the range of 1000 to 2500 Hz. Our model with the adjusted parameters presents a clear resonance peak at 1.8 kHz, well placed among those of our individual subject responses and the finding of Keefe et al. (1993).

Keefe et al. (1993) found an increase in the admittance magnitudes at frequencies higher than 4 kHz. They suggested that this might be because of the resonance of the middle-ear cavity. However, their frequency resolution was not high enough to distinguish this effect from the effect of the first standing-wave mode in the canal, which also results in a peak of admittance magnitude. In our clinical data with 1/12-octave resolution, both the individual responses and the mean curve show two peaks, at 5.1 and

6.3 kHz. These features, which may be attributable to the resonance of the middle-ear cavity and the occurrence of the first standing-wave mode inside the ear canal, occurred in our model at 6.1 and 7.2 kHz, respectively.

Previous clinical reports (e.g., Holte et al., 1990; Keefe et al., 1993; Keefe and Levi, 1996; Sanford and Feeney, 2008) concluded that the canal contribution to the total admittance response of the ear is substantial at frequencies below 1 kHz and that traditional low-frequency tympanometry at single probe tones of 250, 650 and 1000 Hz does not reflect the middle-ear response. Our model provides a description of the canal contribution to the overall admittance response of the newborn ear and shows quantitatively that at frequencies around the middle-ear resonance (around 1.8 kHz) the admittance of the newborn ear is mainly dominated by that of the middle ear. This model also predicts the features of the first resonance mode of the middle-ear cavity (around 6 kHz) as well as the first and second standing-wave modes in the ear canal (around 7.2 and 9.6 kHz, respectively). Wideband immittance measurements with higher frequency resolution will be required to further investigate these features.

## **5.5 Acknowledgements**

This work was supported in part by the Canadian Institutes of Health Research, the Fonds de recherche en santé du Québec, the Natural Sciences and Engineering Research Council (Canada), the Montréal Children's Hospital Research Institute, the McGill University Health Centre Research Institute. Computations were made on the supercomputer Guillimin of McGill University, managed by Calcul Québec and Compute Canada; the operation of this supercomputer is funded by the Canada Foundation for Innovation, NanoQuébec, the Réseau de Médecine Génétique Appliquée and the Fonds de recherche du Québec – Nature et technologies. The authors thank C. Northrop (Temporal Bone Foundation, Boston) for the histological images used to supplement and help interpret our CT scan.

# Chapter 6: Conclusions and future work

## 6.1 Summary

In this thesis, the focus was on finite-element modelling relevant to the tympanometric response of the newborn ear. In the first study, a model of non-linear viscoelastic tympanic-membrane tissue was developed. This model is suitable for modelling large deformations of the tympanic membrane in conditions corresponding to the pressurization involved in tympanometry (pressurized immittance measurements). In the second study, newborn ear-canal and middle-ear models were developed and their responses to acoustic stimulation were explored for frequencies up to 2 kHz. In this frequency range, corresponding to conventional multi-frequency tympanometry, the wavelength of sound is long enough that the air spaces of the outer and middle ear are often modelled as lumped elements, which allowed the individual responses of the components to be quantitatively differentiated. In the third study, taking into account the fluid-structure interaction between the sound pressure in the ear canal and middle-ear cavity and the vibrations of the ear structures, we could extend the excitation frequency range up to 10 kHz, corresponding to wideband tympanometry. The results of these studies provide insight into the features present in clinical immittance measurements in newborns and infants.

## 6.2 Original contributions

1. The non-linear viscoelastic behaviour of the tympanic membrane was modelled. The major outcomes are:
  - a) A numerical approach to represent the non-linear and time-dependent behaviour of the TM was proposed.
  - b) An iterative method was developed to identify material parameters by simultaneously fitting stress-strain and relaxation tests.
  - c) This model could reproduce both the loading and unloading curves, with the associated

hysteresis, with a single set of parameters.

- d) Taking into account the time-dependent behaviour, this model provides a quantitative measure of the energy dissipation as a function of frequency and the effect of the loading rate on the mechanical response of the TM.
  - e) Being able to represent the TM response to large, sweeping quasi-static pressures, this model will facilitate numerical modelling of tympanometry.
2. The individual and combined input-immittance responses of newborn ear-canal and middle-ear models to acoustic excitation were studied for frequencies up to 2 kHz. The major outcomes are:
- a) In the absence of experimental data for material properties of the newborn ear components, ranges of plausible values were established for the material properties.
  - b) The resonances of the ear canal and middle ear were quantitatively explored, and the contribution of each component to the overall immittance response of the ear was identified.
  - c) The model was adjusted within the proposed plausible ranges of the material parameters and found to agree quite well with two sets of clinical data: one set from the literature and one set from our own clinical measurements.
  - d) Three sets of systematic sensitivity analyses were performed to investigate the material-parameter effects on the output of the models.
  - e) The model provides quantitative support for the suggestion that clinical immittance measurements in newborns should be performed at frequencies around the middle-ear resonance in order to obtain useful information about the status of the middle ear.
3. Fluid-structure coupling between the air and the structures of the ear canal and middle ear was included in a newborn ear model. The major outcomes are:
- a) By taking into account the fluid-structure coupling, the excitation frequency range was

extended to 10 kHz, suitable to model clinical wideband immittance measurements.

- b) The geometrical and compliance characteristics of the canal and middle ear and their effects on the spatial pressure distributions and the measured admittance responses were explored.
- c) The model was adjusted within the proposed plausible ranges of the material parameters and found to agree quite well with two sets of clinical data.
- d) The main features of standing waves inside the ear canal and the middle-ear cavity and their contributions to the measured immittance data were explored.
- e) Four sets of sensitivity analyses were performed to investigate the effects of the material parameters, geometrical variations, and measurement locations on the immittance response.
- f) The model provides further quantitative support for suggestions that middle-ear status in newborns should be evaluated at frequencies around the middle-ear resonance.
- g) The model provides interpretations for features that exist in the clinical data but whose significance was previously not clear.

### **6.3 Clinical application of this work**

The problems with immittance measurements in newborns and infants at low frequencies have been reported frequently in the literature, and they were attributed to the anatomical differences between adults and newborns. The maturation effects have been studied in clinical measurements and it has been suggested that, due to the contribution of the outer ear to the total input-admittance response at low frequencies (because of its compliant characteristics in newborns and infants), admittance measurement at the traditional probe-tone frequency of 226 Hz is not recommended for assessing the middle-ear status of infants less than 7 months old. However, a quantitative understanding of the underlying mechanisms has been lacking.

Our numerical models of the immittance responses of the newborn ear were able to provide a

quantitative description of the contribution of the ear canal and middle ear to the overall immittance response. The models show that, in newborns, the admittance of the ear is dominated by that of the middle ear at frequencies around the middle-ear resonance (in the neighbourhood of 1.8 kHz), and is rather insensitive to the mechanical properties of the canal. Due to inter-subject variability and to changes with maturation, the resonance frequency will be different in different babies, and the modelling suggests that measurements at multiple frequencies in that neighbourhood can provide more information about the condition of the middle ear. The model also predicts the effects of the first resonance mode of the middle-ear cavity (around 6 kHz) as well as the first and second standing-wave modes in the ear canal (around 7.2 and 9.6 kHz, respectively) and their contributions to the admittance response of the ear. Those features had not been identified explicitly in clinical measurements, but with this new understanding they could be exploited to provide additional information about the ear. With respect to the effects of static pressurization, the non-linear viscoelastic model presented here for the tympanic membrane provides a quantitative approach to understanding the behaviour of the TM when undergoing large deformations at low frequencies and establishes the groundwork for modelling clinical tympanometric measurements.

## **6.4 Future Work**

Brief suggestions for major aspects of future work are provided here.

### **6.4.1 Experimental Work**

No explicit data are available for the mechanical properties of the components of the newborn ear. We established *a priori* estimates of parameters based on measurements reported for the adult ear or other parts of the body. To obtain more realistic and accurate numerical models of the newborn ear, mechanical measurements should be performed on the structural components of newborn ears. Our sensitivity analyses provided information about the relative importance of different material parameters

and which ones should be focused on in order to obtain more realistic models. Although access to newborn cadavers is very limited, there are alternative methods that might be used to obtain the mechanical properties of those structures, such as ultrasound methods.

There have been experimental studies on the pressure distribution inside the ear canals of adults. However, such measurements have not been performed on newborn ear canals. Those kind of experimental measurements would provide more information about the ear's transfer functions in newborns, but they would need to be performed on newborn temporal bones.

Available clinical immittance data in newborns and infants are limited to a few studies, mainly with low frequency resolutions. More measurements are required to understand the inter-subject variability and the maturation effects on the acoustical behaviour of the newborn ear, and better frequency resolution is required.

There are measurements of the vibrational characteristics of the adult ear components (particularly on the TM) in the literature. However, no studies have been conducted to quantify similar characteristics in newborns and infants. Such measurements could be performed on newborn temporal bones, although access to samples is very limited. Improved technology might make it possible to make such measurements *in vivo*.

### **6.4.2 Finite-Element Modelling**

In this thesis we report finite-element modelling studies. However, more remains to be explored. A few suggestions for future finite-element modelling are listed here.

We proposed a numerical model to represent the non-linear and time-dependent behaviour of the TM. Similar data to what we used for our model are available in the literature, for example, for the middle-ear ligaments (e.g., Cheng and Gan, 2008; Gan et al., 2011). Non-linear and time-dependent numerical models for other components of the ear are required to simulate pressurized wideband

immittance measurements, particularly for the soft tissue surrounding the canal, which also undergoes large deformations. The time-dependent behaviour of this tissue and its contribution to the absorbed energy has not been studied yet.

In pressurized immittance measurements, acoustical pressures with low amplitudes but high frequencies are introduced to the canal in the presence of high quasi-static pressures. We proposed a numerical approach to model the TM behaviour at large quasi-static deformations. The linear and dynamic behaviour of the canal and middle-ear models were studied in Chapters 4 and 5 in response to low-amplitude acoustical loads. A more realistic model of ear components should be able to model the combination of these two loading conditions.

Due to the low resolution of the CT images, we could not include very fine components of the ear structure, such as the stapes, stapedial annular ligament, etc. Sets of micro CT and histological images, with higher resolutions, are required for a more realistic geometry of the newborn ear.

Our newborn outer- and middle-ear models were constructed from a CT scan for a single subject. To investigate the effects of inter-subject variability, as well as maturation effects, more three-dimensional models of newborns of different ages should be used for numerical simulations. The effects of inter-subject variability might also be investigated by performing systematic sensitivity analyses on the effects of geometrical variability.

The acoustic pressure distribution inside the canal, across the TM surface, and in the middle-ear cavity is highly frequency-dependent. Some of the main features of the pressure maps were studied in this thesis. More work remains to provide better insight into the sound-pressure distributions within the ear. The pressure distribution over the ear components directly affects the input immittance response of the ear.

## References

- Aernouts, J., Aerts, J. R. M., and Dirckx, J. J. J. (2012). “Mechanical properties of human tympanic membrane in the quasi-static regime from in situ point indentation measurements,” *Hear. Res.* **290**, 45–54.
- Aernouts, J., and Dirckx, J. J. J. (2012). “Static versus dynamic gerbil tympanic membrane elasticity: derivation of the complex modulus,” *Biomech. Model. Mechanobiol.* **11**, 829–840.
- Agache, P. G., Monneur, C., Leveque, J. L., and De Rigal, J. (1980). “Mechanical properties and Young’s modulus of human skin in vivo,” *Arch. Dermatol. Res.* **269**, 221–232.
- Akinpelu, O. V., Peleva, E., Funnell, W. R. J., and Daniel, S. J. (2014). “Otoacoustic emissions in newborn hearing screening: A systematic review of the effects of different protocols on test outcomes,” *Int. J. Pediatr. Otorhinolaryngol.* **78**, 711–717.
- Alberti, P. W., and Jerger, J. F. (1974). “Probe-tone frequency and the diagnostic value of tympanometry,” *Arch. Otolaryngol.* **99**, 206–210.
- American Academy of Pediatrics (2007). “Year 2007 position statement: principles and guidelines for early hearing detection and intervention programs,” *Pediatrics* **120**, 898.
- Anson, B. J., and Donaldson, J. A. (1992). *Surgical anatomy of the temporal bone and ear* (Saunders Philadelphia, New York), 4th ed.
- Békésy, G. v. (1949). “The structure of the middle ear and the hearing of one’s own voice by bone conduction,” *J. Acoust. Soc. Am.* **21**, 217–232.
- Bergevin, C., and Olson, E. S. (2014). “External and middle ear sound pressure distribution and acoustic coupling to the tympanic membrane,” *J. Acoust. Soc. Am.* **135**, 1294–1312.
- Cancura, W. (1979). “On the Elasticity of the Ligamentum Anulare,” **225**, 27–32.
- Charlebois, M., Motallebzadeh, H., and Funnell, W. R. J. (2013). “Visco-hyperelastic law for finite deformations: a frequency analysis,” *Biomech. Model. Mechanobiol.* **12**, 705–715.
- Cheng, T., Dai, C., and Gan, R. Z. (2007). “Viscoelastic properties of human tympanic membrane,” *Ann. Biomed. Eng.* **35**, 305–314.
- Cheng, T., and Gan, R. Z. (2008). “Mechanical properties of anterior malleolar ligament from

- experimental measurement and material modeling analysis,” *Biomech. Model. Mechanobiol.* **7**, 387–394.
- Clemens, C. J., and Davis, S. A. (2001). “Minimizing false-positives in universal newborn hearing screening: a simple solution,” *Pediatrics* **107**, E29.
- Colletti, V. (1975). “Methodologic observations on tympanometry with regard to the probe tone frequency,” *Acta Otolaryngol. (Stockh.)* **80**, 54–60.
- Cowin, S. C. (2001). “Bone mechanics handbook,” (CRC Press, New York), 2nd ed.
- Daniel, S. J., Funnell, W. R., Zeitouni, A. G., Schloss, M. D., and Rappaport, J. (2001). “Clinical applications of a finite-element model of the human middle ear,” *J. Otolaryngol.* **30**, 340–346.
- Daphalapurkar, N. P., Dai, C., Gan, R. Z., and Lu, H. (2009). “Characterization of the linearly viscoelastic behavior of human tympanic membrane by nanoindentation,” *J. Mech. Behav. Biomed. Mater.* **2**, 82–92.
- Day, J. ., and Funnell, R. W. J. (1990). “An approach to finite-element modelling of the structural-acoustic interaction between the ear canal and eardrum,” *Proc 16th Can Med Biol Eng Conf Winn.*
- Decraemer, W. F., Dirckx, J. J. J., and Funnell, W. R. J. (2003). “Three-dimensional modelling of the middle-ear ossicular chain using a commercial high-resolution X-ray CT scanner,” *J. Assoc. Res. Otolaryngol.* **4**, 250–263.
- Decraemer, W. F., and Funnell, W. R. J. (2008). “Anatomical and mechanical properties of the tympanic membrane,” *Chronic Otitis Media Pathog.-Oriented Ther. Manag.*
- Decraemer, W. F., Maes, M. A., Vanhuyse, V. J., and Vanpeperstraete, P. (1980). “A non-linear viscoelastic constitutive equation for soft biological tissues, based upon a structural model,” *J. Biomech.* **13**, 559–564.
- Decraemer, W. F., de La Rochefoucauld, O., Dong, W., Khanna, S. M., Dirckx, J. J. J., and Olson, E. S. (2007). “Scala vestibuli pressure and three-dimensional stapes velocity measured in direct succession in gerbils,” *J. Acoust. Soc. Am.* **121**, 2774–2791.
- Decraemer, W., Maes, M., and Vanhuyse, V. (1980). “An elastic stress-strain relation for soft biological

- tissues based on a structural model,” *J. Biomech.* **13**, 463–468.
- Eby, T. L., and Nadol, J. B., Jr (1986). “Postnatal growth of the human temporal bone Implications for cochlear implants in children,” *Ann. Otol. Rhinol. Laryngol.* **95**, 356–364.
- Eiber, A. (1999). “Mechanical modeling and dynamical behavior of the human middle ear,” *Audiol. Neurootol.* **4**, 170–177.
- Elkhoury, N., Liu, H., and Funnell, W. R. J. (2006). “Low-frequency finite-element modeling of the gerbil middle ear,” *J. Assoc. Res. Otolaryngol.* **7**, 399–411.
- Fay, J., Puria, S., Decraemer, W. F., and Steele, C. (2005). “Three approaches for estimating the elastic modulus of the tympanic membrane,” *J. Biomech.* **38**, 1807–1815.
- Feldman, A. S. (1974). “Eardrum abnormality and the measurement of middle ear function,” *Arch. Otolaryngol. Neck Surg.* **99**, 211–217.
- Funasaka, S., Funai, H., and Kumakawa, K. (1984). “Sweep-Frequency Tympanometry: Its Development and Diagnostic Value,” *Int. J. Audiol.* **23**, 366–379.
- Fung, Y. (1993). *Biomechanics: mechanical properties of living tissues* (Springer, New York), 2nd ed.
- Funnell, W. R. J. (1983). “On the undamped natural frequencies and mode shapes of a finite-element model of the cat eardrum,” *J. Acoust. Soc. Am.* **73**, 1657–1661.
- Funnell, W. R. J., and Decraemer, W. F. (1996). “On the incorporation of moiré shape measurements in finite-element models of the cat eardrum,” *J. Acoust. Soc. Am.* **100**, 925–932.
- Funnell, W. R. J., Decraemer, W. F., and Khanna, S. M. (1987). “On the damped frequency response of a finite-element model of the cat eardrum,” *J. Acoust. Soc. Am.* **81**, 1851–1859.
- Funnell, W. R. J., Khanna, S. M., and Decraemer, W. F. (1992). “On the degree of rigidity of the manubrium in a finite-element model of the cat eardrum,” *J. Acoust. Soc. Am.* **91**, 2082–2090.
- Funnell, W. R. J., and Laszlo, C. A. (1978). “Modeling of the cat eardrum as a thin shell using the finite-element method,” *J Acoust Soc Am* **63**, 1461–1467.
- Funnell, W. R. J., and Laszlo, C. A. (1982). “A critical review of experimental observations on eardrum structure and function,” *ORL J. Oto-Rhino-Laryngol. Its Relat. Spec.* **44**, 181–205.
- Funnell, W. R. J., Maftoon, N., and Decraemer, W. F. (2013). “Modeling of middle ear mechanics,”

Middle Ear (Springer), pp. 171–210.

- Gan, R. Z., Cheng, T., Dai, C., Yang, F., and Wood, M. W. (2009). “Finite element modeling of sound transmission with perforations of tympanic membrane,” *J. Acoust. Soc. Am.* **126**, 243–253.
- Gan, R. Z., Feng, B., and Sun, Q. (2004). “Three-dimensional finite element modeling of human ear for sound transmission,” *Ann. Biomed. Eng.* **32**, 847–859.
- Gan, R. Z., Reeves, B. P., and Wang, X. (2007). “Modeling of sound transmission from ear canal to cochlea,” *Ann. Biomed. Eng.* **35**, 2180–2195.
- Gan, R. Z., and Sun, Q. (2002). “Finite element modeling of human ear with external ear canal and middle ear cavity,” *Eng. Med. Biol. 2002 24th Annu. Conf. Annu. Fall Meet. Biomed. Eng. Soc. EMBSBMES Conf. 2002 Proc. Second Jt. (IEEE), Vol. 1*, pp. 264–265.
- Gan, R. Z., Sun, Q., Feng, B., and Wood, M. W. (2006). “Acoustic–structural coupled finite element analysis for sound transmission in human ear—Pressure distributions,” *Med. Eng. Phys.* **28**, 395–404.
- Gan, R. Z., Yang, F., Zhang, X., and Nakmali, D. (2011). “Mechanical properties of stapedial annular ligament,” *Med. Eng. Phys.* **33**, 330–339.
- Gariepy, B. (2010). *Finite-element modelling of the newborn ear canal and middle ear*. M.Eng. thesis, McGill University, Montréal, Canada.
- Gariepy, B. (2011). *Finite-element modelling of the newborn ear canal and middle ear (Master dissertation)*. McGill University, Montreal, Qc. (M.Eng).
- Gea, S. L. R., Decraemer, W. F., Funnell, R. W. J., Dirckx, J. J. J., and Maier, H. (2010). “Tympanic membrane boundary deformations derived from static displacements observed with computerized tomography in human and gerbil,” *JARO-J. Assoc. Res. Otolaryngol.* **11**, 1–17.
- Geerligs, M., Van Breemen, L., Peters, G., Ackermans, P., Baaijens, F., and Oomens, C. (2011). “In vitro indentation to determine the mechanical properties of epidermis,” *J. Biomech.* **44**, 1176–1181.
- Gilman, S., and Dirks, D. D. (1986). “Acoustics of ear canal measurement of eardrum SPL in simulators,” *J. Acoust. Soc. Am.* **80**, 783–793.

- Greffet, N. (2013). “Éléments vibro-acoustiques,” Retrieved from [http://www.code-aster.org/V2/doc/default/fr/man\\_r/r4/r4.02.02.pdf](http://www.code-aster.org/V2/doc/default/fr/man_r/r4/r4.02.02.pdf).
- Gulya, A. (1995). “Anatomy of the temporal bone with surgical implications,” *Otolaryngol.-Head Neck Surg.* **112**, P165.
- Hayes, W. C., and Mockros, L. F. (1971). “Viscoelastic properties of human articular cartilage,” *J. Appl. Physiol.* **31**, 562–568.
- Holte, L., Cavanaugh, R. M., and Margolis, R. H. (1990). “Ear canal wall mobility and tympanometric shape in young infants,” *J. Pediatr.* **117**, 77–80.
- Holte, L., Margolis, R. H., and Cavanaugh, R. M., Jr (1991). “Developmental changes in multifrequency tympanograms,” *Audiol. Off. Organ Int. Soc. Audiol.* **30**, 1–24.
- Holzappel, G. A. (2000). *Nonlinear solid mechanics: a continuum approach for engineering* (John Wiley & Sons Ltd).
- Huang, G., Daphalapurkar, N. P., Gan, R. Z., and Lu, H. (2008). “A method for measuring linearly viscoelastic properties of human tympanic membrane using nanoindentation,” *J. Biomech. Eng.* **130**, 014501.
- Humphrey, J. (2003). “Review paper: Continuum biomechanics of soft biological tissues,” *Proc. R. Soc. Lond. Ser. Math. Phys. Eng. Sci.* **459**, 3–46.
- Hunter, L. L., Feeney, M. P., Lapsley Miller, J. A., Jeng, P. S., and Bohning, S. (2010). “Wideband reflectance in newborns: normative regions and relationship to hearing-screening results,” *Ear Hear.* **31**, 599–610.
- Ihrle, S., Lauxmann, M., Eiber, A., and Eberhard, P. (2013). “Nonlinear modelling of the middle ear as an elastic multibody system—Applying model order reduction to acousto-structural coupled systems,” *J. Comput. Appl. Math.* **246**, 18–26.
- Joint Committee on Infant Hearing 1994 Position Statement (n.d.). “Joint Committee on Infant Hearing 1994 Position Statement,” *Otolaryngol.-Head Neck Surg.* **113**, 191–196.
- Keefe, D. H., Bulen, J. C., Arehart, K. H., and Burns, E. M. (1993). “Ear-canal impedance and reflection coefficient in human infants and adults,” *J. Acoust. Soc. Am.* **94**, 2617–2638.

- Keefe, D. H., and Levi, E. (1996). “Maturation of the middle and external ears: acoustic power-based responses and reflectance tympanometry,” *Ear Hear.* **17**, 361–373.
- Keefe, D. H., and Simmons, J. L. (2003). “Energy transmittance predicts conductive hearing loss in older children and adults,” *J. Acoust. Soc. Am.* **114**, 3217–3238.
- Kelly, D. J., Prendergast, P. J., and Blayney, A. W. (2003). “The effect of prosthesis design on vibration of the reconstructed ossicular chain: a comparative finite element analysis of four prostheses,” *Otol. Neurotol.* **24**, 11–19.
- Khanna, S. M., and Tonndorf, J. (1972). “Tympanic Membrane Vibrations in Cats Studied by Time-Averaged Holography,” *J. Acoust. Soc. Am.* **51**, 1904.
- Kirikae, I. (1960). *The structure and function of the middle ear* (Tokyo: University of Tokyo Press), 46-48 pages.
- Knauss, W. G., and Zhao, J. (2007). “Improved relaxation time coverage in ramp-strain histories,” *Mech. Time-Depend. Mater.* **11**, 199–216.
- Koike, T., Wada, H., and Kobayashi, T. (2002). “Modeling of the human middle ear using the finite-element method,” *J. Acoust. Soc. Am.* **111**, 1306–1317.
- Kuypers, L. C., Decraemer, W. F., and Dirckx, J. J. (2006). “Thickness distribution of fresh and preserved human eardrums measured with confocal microscopy,” *Otol. Neurotol.* **27**, 256–264.
- Ladak, H. M., and Funnell, W. R. J. (1996). “Finite-element modeling of the normal and surgically repaired cat middle ear,” *J. Acoust. Soc. Am.* **100**, 933–944.
- Ladak, H. M., Funnell, W. R. J., Decraemer, W. F., and Dirckx, J. J. (2006). “A geometrically nonlinear finite-element model of the cat eardrum,” *J. Acoust. Soc. Am.* **119**, 2859.
- Lang-Roth, R. (2014). “Hearing impairment and language delay in infants: Diagnostics and genetics,” *GMS Curr. Top. Otorhinolaryngol. Head Neck Surg.* **13**.
- Lauxmann, M., Eiber, A., Haag, F., and Ihrle, S. (2014). “Nonlinear stiffness characteristics of the annular ligament,” *J. Acoust. Soc. Am.* **136**, 1756–1767.
- Lee, C.-F., Chen, P.-R., Lee, W.-J., Chou, Y.-F., Chen, J.-H., and Liu, T.-C. (2010). “Computer aided modeling of human mastoid cavity biomechanics using finite element analysis,” *EURASIP J.*

- Adv. Signal Process. **2010**, 6.
- Lesser, T. H. J., and Williams, K. R. (1988). "The tympanic membrane in cross section: a finite element analysis," J. Laryngol. Otol. **102**, 209–214.
- Lim, D. J. (1970). "Human tympanic membrane: an ultrastructural observation," Acta Otolaryngol. (Stockh.) **70**, 176–186.
- Lim, D. J. (1995). "Structure and function of the tympanic membrane: a review," Acta Otorhinolaryngol. Belg. **49**, 101–115.
- Liu, Y.-W., Sanford, C. A., Ellison, J. C., Fitzpatrick, D. F., Gorga, M. P., and Keefe, D. H. (2008). "Wideband absorbance tympanometry using pressure sweeps: System development and results on adults with normal hearing," J. Acoust. Soc. Am. **124**, 3708–3719.
- Luo, H., Dai, C., Gan, R. Z., and Lu, H. (2009). "Measurement of young's modulus of human tympanic membrane at high strain rates," J. Biomech. Eng. **131**, 064501.
- Luo, H., Lu, H., Dai, C., and Gan, R. Z. (2009). "A comparison of Young's modulus for normal and diseased human eardrums at high strain rates," Int. J. Exp. Comput. Biomech. **1**, 1–22.
- Maas, S. A., Ellis, B. J., Ateshian, G. A., and Weiss, J. A. (2012). "FEBio: finite elements for biomechanics," J. Biomech. Eng. **134**, 011005.
- Maftoon, N. Funnell, W. R. J., Daniel, S. J., and Decraemer, W. F. (2015). "Finite-Element Modelling of the Response of the Gerbil Middle Ear to Sound," J. Assoc. Res. Otolaryngol. **16**, 547–567.
- Margolis, R. H., Bass-Ringdahl, S., Hanks, W. D., Holte, L., and Zapala, D. A. (2003). "Tympanometry in newborn infants--1 kHz norms," J. Am. Acad. Audiol. **14**, 383–392.
- Martins, P., Natal Jorge, R., and Ferreira, A. (2006). "A Comparative Study of Several Material Models for Prediction of Hyperelastic Properties: Application to Silicone-Rubber and Soft Tissues," Strain **42**, 135–147.
- Mase, G. T., and Mase, G. E. (1999). *Continuum mechanics for engineers* (CRC, New York), 2nd ed., 344-346 pages.
- McLellan, M. S., and Webb, C. H. (1950). "Ear studies in the newborn infant," J. Pediatr **51**, 672–677.
- Merchant, G. R., Horton, N. J., and Voss, S. E. (2010). "Normative reflectance and transmittance

- measurements on healthy newborn and 1-month-old infants,” *Ear Hear.* **31**, 746–754.
- Molvaer, O. I., Vallersnes, F. M., and Kringlebotn, M. (1978). “The size of the middle ear and the mastoid air cell: System measured by an acoustic method,” *Acta Otolaryngol. (Stockh.)* **85**, 24–32.
- Morris, M. D. (1991). “Factorial sampling plans for preliminary computational experiments,” *Technometrics* **33**, 161–174.
- Motallebzadeh, H., Charlebois, M., and Funnell, W. R. J. (2013). “A non-linear viscoelastic model for the tympanic membrane,” *J. Acoust. Soc. Am.* **134**, 4427–4434.
- Motallebzadeh, H., Garipey, B., Maftoon, N., Funnell, W. R. J., and Daniel, S. J. (2013). “Finite-element modelling of the newborn ear canal and middle ear,” *Proc. Meet. Acoust. (Acoustical Society of America)*, Vol. 19, p. 030101.
- Motallebzadeh, H., Pitaro, J., Funnell, W. R. J., and Daniel, S. J. (2015). “Finite-element modelling of the acoustic input admittance of the newborn ear canal and middle ear,” Submitted to *J. Assoc. Res. Otolaryngol.*
- Ogden, R. W. (1972). “Large deformation isotropic elasticity-on the correlation of theory and experiment for incompressible rubberlike solids,” *Proc. R. Soc. Lond. Math. Phys. Sci.* **326**, 565–584.
- Overstreet III, E. H., and Ruggero, M. A. (2002). “Development of wide-band middle ear transmission in the Mongolian gerbil,” *J. Acoust. Soc. Am.* **111**, 261–270.
- Paradise, J. L. (1982). “Editorial retrospective: tympanometry,” *N. Engl. J. Med.* **307**, 1074–1076.
- Paradise, J. L., Smith, C. G., and Bluestone, C. D. (1976). “Tympanometric detection of middle ear effusion in infants and young children,” *Pediatrics* **58**, 198–210.
- Park, S. W., and Schapery, R. A. (1999). “Methods of interconversion between linear viscoelastic material functions Part I—A numerical method based on Prony series,” *Int. J. Solids Struct.* **36**, 1653–1675.
- Pitaro, J. (2013). *Wideband Measurements in Newborns: Relationship to Otolaryngologic Findings*. M.Sc. thesis, McGill University, Montréal, Canada.

[http://audilab.bme.mcgill.ca/~funnell/AudiLab/theses/pitaro\\_2013\\_thesis.pdf](http://audilab.bme.mcgill.ca/~funnell/AudiLab/theses/pitaro_2013_thesis.pdf)

- Puso, M. A., and Weiss, J. A. (1998). "Finite element implementation of anisotropic quasi-linear viscoelasticity using a discrete spectrum approximation," *J. Biomech. Eng.* **120**, 62–70.
- Qi, L. (2008). *Non-linear Finite-element Modelling of Newborn Ear Canal and Middle Ear*.
- Qi, L., Funnell, W. R. J., and Daniel, S. J. (2008). "A nonlinear finite-element model of the newborn middle ear," *J. Acoust. Soc. Am.* **124**, 337.
- Qi, L., Liu, H., Lutfy, J., Funnell, W. R. J., and Daniel, S. J. (2006). "A nonlinear finite-element model of the newborn ear canal," *J. Acoust. Soc. Am.* **120**, 3789.
- Rabbitt, R. D. (1988). "High-frequency plane waves in the ear canal: Application of a simple asymptotic theory," *J. Acoust. Soc. Am.* **84**, 2070–2080.
- Rollhäuser, H. (1950). "Die zugfestigkeit der menschlichen haut," *Gegenbaurs Morph Jb* **90**, 249.
- Rosowski, J. J., Cheng, J. T., Ravicz, M. E., Hulli, N., Hernandez-Montes, M., Harrington, E., and Furlong, C. (2009). "Computer-assisted time-averaged holograms of the motion of the surface of the mammalian tympanic membrane with sound stimuli of 04-25 kHz," *Hear. Res.* **253**, 83–96.
- Ruah, C. B., Schachern, P. A., Zelterman, D., Paparella, M. M., and Yoon, T. H. (1991). "Age-related morphologic changes in the human tympanic membrane A light and electron microscopic study," *Arch. Otolaryngol. Head Neck Surg.* **117**, 627–634.
- Sanford, C. A., and Feeney, M. P. (2008). "Effects of maturation on tympanometric wideband acoustic transfer functions in human infants," *J. Acoust. Soc. Am.* **124**, 2106–2122.
- Saunders, J. C., Kaltenbach, J. A., and Relkin, E. M. (1983). "The structural and functional development of the outer and middle ear," *Dev. Audit. Vestib. Syst.*
- Schatzmann, L., Brunner, P., and Stäubli, H. (1998). "Effect of cyclic preconditioning on the tensile properties of human quadriceps tendons and patellar ligaments," *Knee Surg. Sports Traumatol. Arthrosc.* **6**, 56–61.
- Schomburg, W. K. (2011). *Introduction to Microsystem Design* (Springer, Berlin ; Heidelberg), 29-30 pages.

- Shahnaz, N., Miranda, T., and Polka, L. (2008). “Multifrequency tympanometry in neonatal intensive care unit and well babies,” *J. Am. Acad. Audiol.* **19**, 392–418.
- Shahnaz, N., and Polka, L. (1997). “Standard and multifrequency tympanometry in normal and otosclerotic ears,” *Ear Hear.* **18**, 326–341.
- Shanks, J. E., and Lilly, D. J. (1981). “An evaluation of tympanometric estimates of ear canal volume,” *J. Speech Hear. Res.* **24**, 557.
- Soons, J. A., Aernouts, J., and Dirckx, J. J. (2010). “Elasticity modulus of rabbit middle ear ossicles determined by a novel micro-indentation technique,” *Hear. Res.* **263**, 33–37.
- Stach, B. A. (2008). *Clinical audiology: an introduction* (Cengage Learning).
- Standring, S. (2008). *Gray’s Anatomy: The anatomical basis of clinical practice, expert consult* (Elsevier, Spaine), fortieth.
- Stepp, C. E., and Voss, S. E. (2005). “Acoustics of the human middle-ear air space,” *J. Acoust. Soc. Am.* **118**, 861–871.
- Stinson, M. R. (1985). “Spatial variation of phase in ducts and the measurement of acoustic energy reflection coefficients,” *J. Acoust. Soc. Am.* **77**, 386–393.
- Stinson, M. R. (1985). “The spatial distribution of sound pressure within scaled replicas of the human ear canal,” *J. Acoust. Soc. Am.* **78**, 1596–1602.
- Stinson, M. R., and Khanna, S. M. (1989). “Sound propagation in the ear canal and coupling to the eardrum, with measurements on model systems,” *J. Acoust. Soc. Am.* **85**, 2481–2491.
- Stinson, M. R., Shaw, E. A. G., and Lawton, B. W. (1982). “Estimation of acoustical energy reflectance at the eardrum from measurements of pressure distribution in the human ear canal,” *J. Acoust. Soc. Am.* **72**, 766–773.
- Sun, Q., Gan, R. Z., Chang, K.-H., and Dormer, K. J. (2002). “Computer-integrated finite element modeling of human middle ear,” *Biomech. Model. Mechanobiol.* **1**, 109–122.
- Taylor, R. L., Pister, K. S., and Goudreau, G. L. (1970). “Thermomechanical analysis of viscoelastic solids,” *Int. J. Numer. Methods Eng.* **2**, 45–59.
- Tonndorf, J., and Khanna, S. M. (1972). “Tympanic-membrane vibrations in human cadaver ears

- studied by time-averaged holography,” *J. Acoust. Soc. Am.* **52**, 1221–1233.
- Tuck-Lee, J. P., Pinsky, P. M., Steele, C. R., and Puria, S. (2008). “Finite element modeling of acousto-mechanical coupling in the cat middle ear,” *J. Acoust. Soc. Am.* **124**, 348–362.
- Volandri, G., Carmignani, C., Di Puccio, F., and Forte, P. (2014). “Finite Element Formulations Applied to Outer Ear Modeling,” *Stroj. Vestn.-J. Mech. Eng.* **60**, 363–372.
- Volandri, G., Di Puccio, F., Forte, P., and Carmignani, C. (2011). “Biomechanics of the tympanic membrane,” *J. Biomech.* **44**, 1219–1236.
- Voss, S. E., and Allen, J. B. (1994). “Measurement of acoustic impedance and reflectance in the human ear canal,” *J. Acoust. Soc. Am.* **95**, 372–384.
- Wada, H., Metoki, T., and Kobayashi, T. (1992). “Analysis of dynamic behavior of human middle ear using a finite-element method,” *J. Acoust. Soc. Am.* **92**, 3157–3168.
- Waller, T.-S., and AMBERG, A. (2002). *AUS DER KLINIK UND POLIKLINIK FÜR HALS-, NASEN- UND OHRENKRANKE DER UNIVERSITÄT WÜRZBURG.*
- Wellman, P., Howe, R. D., Dalton, E., and Kern, K. A. (1999). “Breast tissue stiffness in compression is correlated to histological diagnosis,” *Harv. BioRobotics Lab. Tech. Rep.*
- Wever, E. G., and Lawrence, M. (1954). *Physiological acoustics.* (Princeton university press, Princeton).
- Williams, K. R., and Lesser, T. H. J. (1990). “A finite element analysis of the natural frequencies of vibration of the human tympanic membrane Part I,” *Br. J. Audiol.* **24**, 319–327.
- Williamson, A. K., Chen, A. C., and Sah, R. L. (2001). “Compressive properties and function-composition relationships of developing bovine articular cartilage,” *J. Orthop. Res. Off. Publ. Orthop. Res. Soc.* **19**, 1113–1121.
- Wu, J. Z., Dong, R. G., Smutz, W. P., and Schopper, A. W. (2003). “Nonlinear and viscoelastic characteristics of skin under compression: experiment and analysis,” *Biomed. Mater. Eng.* **13**, 373–385.
- Yamada, H., and Evans, F. G. (1970). “Strength of biological materials,” (Williams & Wilkins, Baltimore)
- Zhang, X., and Gan, R. Z. (2010). “Dynamic properties of human tympanic membrane—experimental

measurement and modelling analysis,” *Int. J. Exp. Comput. Biomech.* **1**, 252–270.

Zhang, X., and Gan, R. Z. (2013). “Dynamic Properties of Human Tympanic Membrane Based on Frequency-Temperature Superposition,” *Ann. Biomed. Eng.* **41**, 205–214.

Zienkiewicz, O. C., Taylor, R. L., Zienkiewicz, O. C., and Taylor, R. L. (1977). *The finite element method* (McGraw-hill London), Vol. 3.